# FACULTY OF MATHEMATICS AND PHYSICS
## Charles University

# DOCTORAL THESIS

## Dmytro Shapko

## EXPERIMENTAL STUDY OF THE DISSOCIATIVE RECOMBINATION OF MOLECULAR IONS AT TEMPERATURES RELEVANT TO COLD INTERSTELLAR PLASMA
## (30 – 300 K)

Department of Surface and Plasma Science

Supervisor:   prof. RNDr. Juraj Glosík, DrSc.

Scientific advisor:   doc. RNDr. Radek Plašil, Ph.D.

Study program:   Physics

Study branch:   Physics of Plasmas and Ionized Media

Prague 2023

# ACKNOWLEDGMENT

## *2*

I would like to express my sincere gratitude to all those who have helped and supported me throughout my Ph.D. journey under the guidance of prof. Juraj Glosík.

First and foremost, I would like to thank my advisor Petr Dohnal, who has provided me with invaluable guidance, support, and encouragement throughout the years. His unwavering faith in me and my research has been a constant source of inspiration and motivation.

I would like to extend my heartfelt thanks to my colleagues, especially Ábel Kálosi, Artem Kovalenko, Dung Tran, Štěpán Roučka, doc. Radek Plašil who have made my time here both enjoyable and productive.

I would like to acknowledge the funding support from GAUK, Erasmus+, Czech Academy of Science, without which my research would not have been possible.

Finally, I would like to express my love and gratitude to my family and cats, for their unwavering love and support. Their encouragement and understanding have been a constant source of strength throughout the years.

This thesis is a testament to the support and encouragement that I have received from all of you. Thank you.

I declare that I carried out this doctoral thesis independently, and only with the cited sources, literature and other professional sources.

I understand that my work relates to the rights and obligations under the Act No. 121/2000 Coll., the Copyright Act, as amended, in particular the fact that the Charles University has the right to conclude a license agreement on the use of this work as a school work pursuant to Section 60 paragraph 1 of the Copyright Act.

*Prague, 16th June 2023*                                              *Dmytro Shapko*

ABSTRACT: The dissociative recombination process of $N_2H^+$ ions with electrons was investigated using a stationary afterglow combined with a Cavity Ring-Down Spectrometer. We conducted real-time observations of the changes over time in the population densities of various rotational and vibrational states of recombining $N_2H^+$ ions. Based on these observations, we determined the rate coefficients for thermal recombination of $N_2H^+$ within a temperature range of 80 – 350 K. By employing newly calculated vibrational transition moments of $N_2H^+$, we provided an explanation for the discrepancies observed in previous studies regarding the recombination rate coefficients. Furthermore, our findings indicate that the measured recombination rate coefficient does not exhibit a statistically significant correlation with the number density of the buffer gas. We also conducted a study on the dissociative recombination of $H_3^+$ ions with electrons in neon gas at a temperature of 110 K. To perform this investigation, we utilized a new Cryogenic Stationary Afterglow apparatus equipped with a Cavity Ring-Down Spectrometer and an electron number density measurement system. Our results revealed that the ternary recombination rate coefficient, denoted as $K_{Ne}$(110 K), closely resembles the value obtained in a helium buffered plasma.

KEYWORDS: dissociative recombination, afterglow plasma, CRDS, low temperature plasma, astrochemistry, molecular ions, electrons, recombination rate coefficient

ABSTRAKT: Byl zkoumán proces disociativní rekombinace iontů $N_2H^+$ s elektrony pomocí stacionárního dohasínajícího plazmatu ve spojení s Cavity Ring-Down Spektrometrem. Prováděli jsme reálné sledování změn v hustotách populace různých rotačních a vibračních stavů rekombinujících iontů $N_2H^+$ v průběhu času. Na základě těchto pozorování jsme určili koeficienty rychlosti pro termální rekombinaci $N_2H^+$ v teplotním rozsahu 80 – 350 K. S využitím nově vypočtených vibračních momentů přechodu $N_2H^+$ jsme vysvětlili rozpory pozorované v předchozích studiích týkajících se koeficientů rychlosti rekombinace. Navíc naše zjištění naznačují, že naměřený koeficient rychlosti rekombinace nesvědčí o statisticky významné korelaci s hustotou částic pozaďového plynu. Provedli jsme také studii disociativní rekombinace iontů $H_3^+$ s elektrony v neonovém plynu při teplotě 110 K. Pro provedení této investigace jsme využili nový Kryogenní Stacionární Afterglow aparát vybavený Cavity Ring-Down Spektrometrem a systémem pro měření hustoty elektronů. Naše výsledky ukázaly, že koeficient rekombinace ternárního procesu, označovaný jako $K_{Ne}$(110 K), se blíží hodnotě získané v plazmatu s heliovým pozaďovým plynem.

KLÍČOVÁ SLOVA: disociativní rekombinace, dohasínající plazma, CRDS, nízkoteplotní plazma, astrochemie, molekulární ionty, elektrony, koeficient rychlosti rekombinace.

# CONTENTS

# GOALS OF THE THESIS

The primary scientific objectives of this thesis involved quantifying the recombination rate coefficients of dissociative recombination for multiple molecular ions with electrons, focusing on temperatures below 300 K and potentially as low as 30 K. Notably, particular emphasis was placed on investigating the ternary neutral-assisted recombination process between molecular ions and electrons. To summarize, the goals of this research can be outlined as follows:

- Conduct a comprehensive study on the dissociative recombination of $N_2H^+$ ions with electrons using the SA-CRDS experimental setup.

- Develop a novel Cryo-SA-CRDS apparatus that allows for expanding the measurement region of SA-CRDS to temperatures as low as 30 K.

- Incorporate direct time-resolved electron number density measurement through microwave diagnostics into the Cryo-SA-CRDS setup.

- Determine the recombination rate coefficient for the neon-assisted dissociative recombination of $H_3^+$ ions with electrons utilizing the new Cryo-SA-CRDS apparatus.

# PUBLICATIONS

The present thesis is an extension of a collection of articles that were published throughout the duration of the research. Certain concepts and illustrations have been previously featured in the subsequent publications (are attached in chapter 5):

Glosík, J.; Dohnal, P.; Kálosi, Á.; Augustovičová, L. D.; Shapko, D.; Roučka, Š.; Plašil, R. Electron-Ion Recombination in Low Temperature Hydrogen/Deuterium Plasma. *Eur. Phys. J. Appl. Phys.* **2017**, *80* (3), 30801. https://doi.org/10.1051/epjap/2017170228.

Kálosi, Á.; Dohnal, P.; Shapko, D.; Roučka, Š.; Plašil, R.; Johnsen, R.; Glosík, J. Overtone Spectroscopy of $N_2H^+$ Molecular Ions—Application of Cavity Ring-down Spectroscopy. *J. Instrum.* **2017**, *12* (10), C10010. https://doi.org/10.1088/1748-0221/12/10/C10010.

Plašil, R.; Dohnal, P.; Kálosi, Á.; Roučka, Š.; Shapko, D.; Rednyk, S.; Johnsen, R.; Glosík, J. Stationary Afterglow Apparatus with CRDS for Study of Processes in Plasmas from 300 K down to 30 K. *Rev. Sci. Instrum.* **2018**, *89* (6), 063116. https://doi.org/10.1063/1.5036834.

Dohnal, P.; Shapko, D.; Kálosi, Á.; Kassayová, M.; Roučka, Š.; Rednyk, S.; Plašil, R.; Hejduk, M.; Glosík, J. Towards State Selective Recombination of $H_3^+$ under Astrophysically Relevant Conditions. *Faraday Discuss.* **2019**, *217* (0), 220 – 234. https://doi.org/10.1039/C8FD00214B.

Shapko, D.; Dohnal, P.; Kassayová, M.; Kálosi, Á.; Rednyk, S.; Roučka, Š.; Plašil, R.; Augustovičová, L. D.; Johnsen, R.; Špirko, V.; Glosík, J. Dissociative Recombination of $N_2H^+$ Ions with Electrons in the Temperature Range of 80 – 350 K. *J. Chem. Phys.* **2020**, *152* (2), 024301. https://doi.org/10.1063/1.5128330.

Shapko, D.; Dohnal, P.; Roučka, Š.; Uvarova, L.; Kassayová, M.; Plašil, R.; Glosík, J. Cavity Ring-down Spectroscopy Study of Neon Assisted Recombination of $H_3^+$ Ions with Electrons. *J. Mol. Spectrosc.* **2021**, *378*, 111450. https://doi.org/10.1016/j.jms.2021.111450.

Plašil, R.; Roučka, Š.; Kovalenko, A.; Tran, T.D.; Rednyk, S.; Dohnal, P.; Shapko, D.; Gerlich, D.; Glosík, J. Reaction of $N^+$ Ion with $H_2$, HD, and $D_2$ at Low Temperatures: Experimental Study of the Pathway to Deuterated Nitrogen-containing Molecules in the Interstellar Medium. *Astrophys. J.* **2022**, *941* (2): 144 (1 – 16). https://doi.org/10.3847/1538-4357/aca088.

# ACRONYMS

| | |
|---|---|
| **AD** | Analog-Digital |
| **AOM** | Acousto-Optic Modulator |
| **BNC** | Bayonet Neill-Concelman |
| **CRDS** | Cavity Ring-Down Spectrometer |
| **Cryo-SA-CRDS** | Cryogenic Stationary Afterglow Cavity Ring-Down Spectrometer |
| **CW** | Continuous Wave |
| **DAQ** | Data Acquisition |
| **DC** | Direct Current |
| **DFB** | Distributed FeedBack |
| **DPDT** | Double Pole Double Throw |
| **DR** | Dissociative Recombination |
| **ECD** | External Cavity Diode |
| **FALP** | Flowing Afterglow Langmuir Probe |
| **FWHM** | Full Width at Half Maximum |
| **GPIB** | General Purpose Interface Bus |
| **IEEE** | Institute of Electrical and Electronics Engineers |
| **IR** | InfraRed |
| **MW** | MicroWave (not Mega Watt) |
| **PC** | Personal Computer |
| **PEC** | Potential Energy Curve |
| **PES** | Potential Energy Surface |
| **RF** | Radio Frequency |
| **RPM** | Revolutions Per Minute |
| **RTD** | Resistance Temperature Detector |
| **SA** | Stationary Afterglow |
| **SMA** | SubMiniature version A |
| **TTL** | Transistor-Transistor-Logic |
| **USB** | Universal Serial Bus |

# LIST OF FIGURES

# LIST OF TABLES

# 1  THEORY

## 1.1 Dissociative recombination

The process of dissociative recombination (DR) of molecular ions with electrons is not fully understood, and is considered a complex phenomenon. However, it is now well-established that DR plays a critical role as a neutralizing agent in the Earth's upper atmosphere, interstellar gas clouds, and it has been the subject of extensive research due to its occurrence in natural and laboratory-produced plasmas [1].

When a free electron possesses kinetic energy, it can recombine with a positive atomic or molecular ion. However, to enter a bound state, the electron's energy must be removed. If there is no third body to absorb the excess energy, it can be released as a photon, although this is an inefficient option for atomic ions. On the other hand, molecular ions can utilize their internal structure to transfer the electron to a bound state, which involves breaking one or several chemical bonds. This efficient process is called **dissociative recombination**, as the capture of the electron is stabilized by the dissociation of the molecular ion. The term "dissociative recombination" was coined alongside a theoretical calculation of the recombination rate coefficient by Bates in 1950 [1, 2].

A complex phenomenon of dissociative recombination is a molecular collision process where at least two nuclei and their bound electrons combine to form a molecular ion and a free electron. These types of collisional processes are typically characterized by cross sections, which represent the probability of a scattering event based on the relative velocity or energy of

the colliding particles. To calculate collisional cross sections, it is necessary to represent the potential energy of the molecule as a function of its geometrical coordinates, known as a Potential Energy Surface (PES). The adiabatic representation of the PES is typically used in the Born-Oppenheimer approximation. The fundamental concept behind the Born-Oppenheimer approximation is to separate the motion of the nuclei and electrons in a molecule because of their significant difference in time scales. When graphically representing the PES, projections are often used to simplify the representation, resulting in a Potential Energy Curve (PEC). In the case of diatomic molecules, the problem is naturally reduced to a PEC. Throughout the following explanations, we will focus on the simplified case of diatomic molecules [3].

Dissociative recombination can be classified into two types: direct (as shown in **Figure 1**) and indirect (as shown in **Figure 2**), which depend on the crossing of the PEC. First, we will start with a brief overview of simplest case of direct dissociative recombination.

## 1.1.1 Direct dissociative recombination

The process of dissociative recombination begins with the union of a molecular ion $AB^+$ and an electron to form a quasi-molecule, which exists in a highly excited autoionization state. In cases where there is no bond between the atoms, as with inert gases, the corresponding molecule AB may not exist. The capture of an electron by the ion is stabilized by the decay of the quasi-molecule into two atoms, one of which may be excited. This is possible when the potential curve of one of the states of the atom system $A^* + B$ intersects with the potential curve of the $AB^+$ ion (**direct dissociative recombination**). Such a situation is depicted in **Figure 1**, which shows the potential energy of both systems as a function of the distance between their nuclei. The figure

illustrates the case of unchanged repulsion between atoms $A^*$ and B, i.e., the absence of an accessible excited bound state [4].

Assuming that the vibrations are not excited in the initial molecular ion, the most probable inter-nuclear distances are those close to the location of the minimum potential energy, $r_m$. Let us suppose that an electron, possessing a certain energy $E$, is somewhere in the vicinity of the ion, as shown in **Figure 1**. At inter-nuclear distances near $r_m$, the $AB^+ + e^-$ and $A^* + B$ systems have the same energies. Therefore, a spontaneous transition from the first configuration to the second is possible. To achieve this, an appropriate restructuring of the electronic shells must occur. The restructuring occurs quickly, at the rate of electron movement in the atoms, and the heavy nuclei do not have time to shift from their positions. Thus, the transition from $AB^+$ to $A^* + B$ is carried out vertically. This is where the so-called Franck-Condon principle comes into play, which states that electronic transitions in molecules occur only along verticals on the potential curve diagram of different states [5].

Thus, the quasi-molecule can either revert to an ion and an electron, realizing its autoionization state, or transition into a state of two atoms. The stabilization of the latter occurs as a result of mutual atom repulsion, which causes the potential energy of the interatomic interaction to be transformed into the kinetic energy of relative motion [4]. The general scheme for direct dissociative recombination can be represented by a formula:

$$AB^+ + e^- \rightleftharpoons AB^{**} \rightarrow A^* + B. \qquad (1)$$
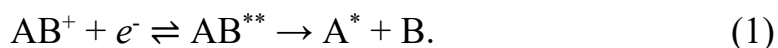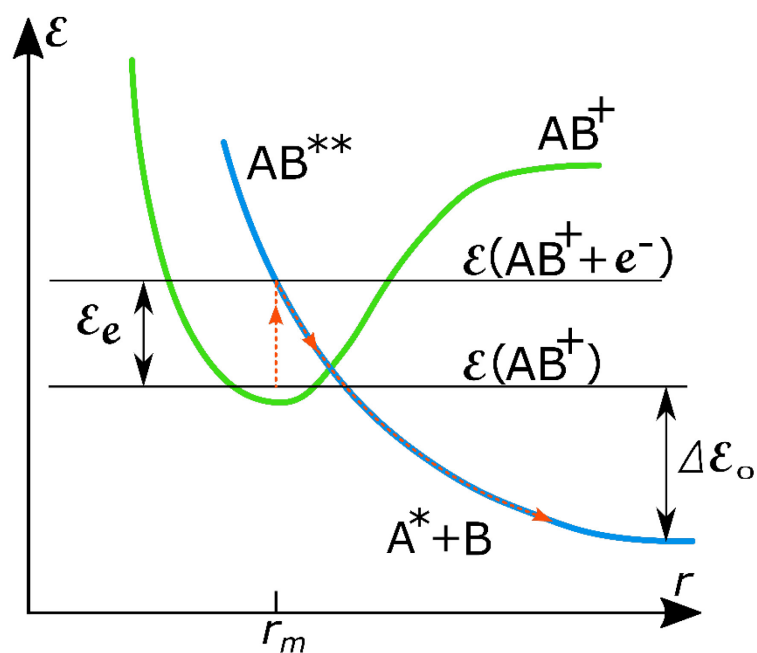
**Figure 1.** The diagram shows the potential energy curves for the direct dissociative recombination process, which involves the combination of an ion and an electron resulting in the formation of a neutral molecule. The orange dotted line indicates the path of the direct DR process. The diatomic molecular ion is denoted as $AB^+$ while the doubly excited neutral molecule is marked as $AB^{**}$. The pair of neutral atoms, where one is in an excited state, is labeled as $A^* + B$. The energy levels of the vibration energy of the ion and the energy of the neutral doubly excited molecule, which forms after attaching an electron to the ion, are represented by two black solid lines, labeled as $\varepsilon(AB^+)$ and $\varepsilon(AB^+ + e^-)$, respectively. The internuclear distance in a diatomic ion where the PEC of the ion has minimum value is marked as $r_m$. The minimum energy that an electron should possess to start the DR process is marked as $\varepsilon_e$, while the energy that will be released during DR is denoted as $\Delta\varepsilon_0$. The light green and blue solid lines represent the potential energy curves of the ion and neutrals, respectively. As we can see, these curves

intersect, allowing for the direct dissociative recombination process to occur. The figure was adapted from reference [4].

## 1.1.2 Indirect dissociative recombination

The **indirect mechanism of dissociative recombination** (**Figure 2**) involves the capture of an electron into a Rydberg state that is excited vibrationally. These Rydberg states are weakly bound, similar to the ion, and cannot dissociate directly. However, it is possible for the Rydberg state to couple with a dissociative resonant state $AB^{**}$, leading to dissociation into neutral products $A^* + B$. It should be noted that these states can also undergo autoionization, which results in the formation of an ion in an excited vibrational state [1]. The general scheme for indirect dissociative recombination can be represented by a formula:

$$AB^+ + e^- \rightleftharpoons \text{Rydberg state} \rightleftharpoons AB^{**} \rightarrow A^* + B. \tag{2}$$
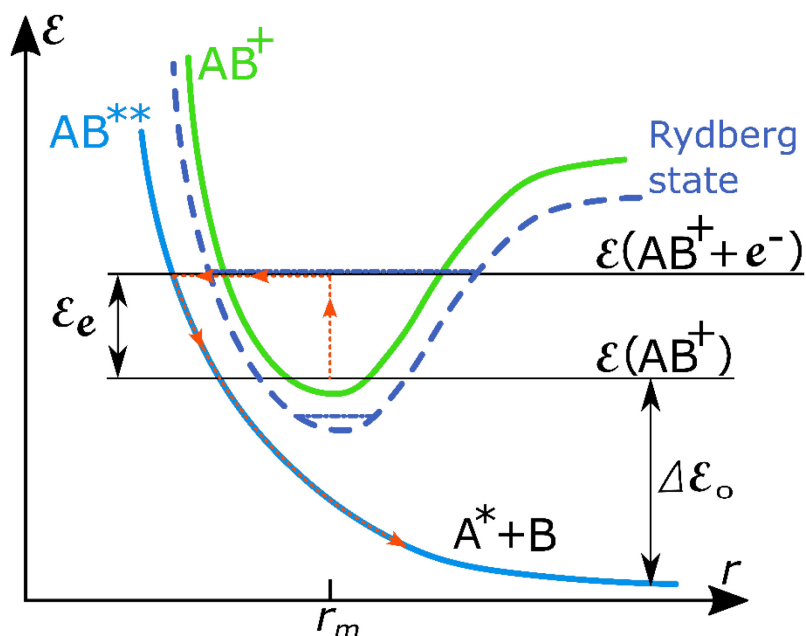


**Figure 2.** The potential energy curves in the diagram depict the process of indirect dissociative recombination, which involves the recombination of

an ion and an electron to form a neutral molecule. The dotted orange line represents the indirect DR process. The diatomic molecular ion is labeled as $AB^+$, and the doubly excited neutral molecule is denoted as $AB^{**}$. A pair of neutral atoms, with one in an excited state, is marked as $A^*+B$. Two black solid lines represent the energy levels of the ion's vibration energy and the neutral doubly excited molecule's energy after attaching an electron to the ion. They are labeled as $\varepsilon(AB^+)$ and $\varepsilon(AB^+ + e^-)$, respectively. The internuclear distance in a diatomic ion where the PEC of the ion has minimum value is marked as $r_m$. The minimum energy required for an electron to start the DR process is marked as $\varepsilon_e$, and the energy released during DR is denoted as $\Delta\varepsilon_0$. The light green and blue solid lines represent the potential energy curves of the ion and neutrals, respectively. As we can observe, these curves do not intersect, indicating that direct dissociative recombination is not possible. The vibrationally excited Rydberg state, marked as a dark blue dashed line, provides the pathway for indirect dissociative recombination. The figure was adapted from reference [1].

# 1.2 $N_2H^+$ investigation background

The atmospheric chemistry of Titan is quite a complicated system where one of the main roles plays $N_2H^+$ (diazenylium) [6]. As a crucial molecular ion, it has been also observed in various interstellar clouds such as translucent and dark ones [7, 8]. The protoplanetary disks [9] and protostellar cores [10] are other sites where $N_2H^+$ ion is abundant. This ion is also famous as an essential tracer for $N_2$, especially in dense clouds. Hence, comprehensive information about fundamental processes such as the production and destruction of $N_2H^+$ is important. The pieces of knowledge about those mechanisms are helpful for the prediction of the abundance of $N_2$ in different interstellar environments. The main production channel for $N_2H^+$ in space is proton transfer from $H_3^+$ to $N_2$ molecules. The primary destruction processes for diazenylium are proton transfer to carbon monoxide (CO) and electron-ion dissociative recombination [11].

Due to its fundamental nature, the recombination of $N_2H^+$ molecular ions with electrons has been an important issue in astrochemistry for over 40 years [1]. There are a lot of experimental data and theoretical calculations on the topic, but the difference between them, in some cases, is around an order of magnitude. In order to get the value of the recombination rate coefficient for diazenylium with electrons a lot of experimental techniques were utilized. In one of the first merged beam experiments with $N_2H^+$ in 1979 Mul and McGowan [12] obtained a value of the coefficient $\alpha = 7.5 \times 10^{-7}$ cm$^3$s$^{-1}$ at 300 K, but as reported in references [1] and [13], taking into account calibration error, the value must be twice smaller. The Flowing Afterglow Langmuir Probe (FALP) experimental studies show a significantly lower recombination rate coefficient for diazenylium at the same temperature. For instant, in 1984 Smith and Adams using FALP received $1.7 \times 10^{-7}$ cm$^3$s$^{-1}$ [14,

15]. The early storage ring measurements on CRYRING demonstrate quite a similar result — $1.7 \times 10^{-7}$ $cm^3s^{-1}$ [16]. Other experiments on later FALP show a slightly higher recombination rate coefficient at room temperature: Smith and Španel [17] had $2.4 \times 10^{-7}$ $cm^3s^{-1}$, and Poterya et al. [18] had $2.8 \times 10^{-7}$ $cm^3s^{-1}$. Rosati et al. studied flowing afterglow plasmas at 300 K. With the aim to explain the emission spectra from diazenylium recombination they used a value of $1.7 \times 10^{-7}$ $cm^3s^{-1}$ [19]. Contemporary results by Vigren et al. [11] measured by using an ion storage ring are in good agreement with Rosati's outcome. Nevertheless, the experiments at a lower temperature are more valuable for interstellar chemistry, but, for an instance, at 100 K the results from FALP measurements vary from ion storage ring values by a factor of two. The internal excitation of recombining ions is the key point. All these publications lack information about it. The rotational populations in the ion storage ring corresponded probably to the temperature of 300 K or even higher [20]. The only one who experimentally probed the internal excitation of recombining diazenylium ions with electrons was Amano [21]. He obtained at 273 K the value of recombination rate coefficient $7 \times 10^{-7}$ $cm^3s^{-1}$, which is significantly higher than the values from the ion storage ring and FALP results at the same temperature.

The theoretical investigations of the dissociative recombination of $N_2H^+$ with electrons are not so numerous. Hickman et al. [22] and Talbi [23] reported that the direct dissociative recombination process of diazenylium ions with electrons is extremely ineffective at low collision energies. The indirect type of dissociative recombination of $N_2H^+$ was investigated theoretically by Fonseca dos Santos et al. [24, 25]. They examine several kinds of vibronic couplings through all vibrational modes of the molecular ion. However, their outcome is almost twice lower than the values from modern ion storage rings and FALP experiments and almost five times lower

than value reported by Amano [21]. The goal of our investigation was to find a way how to explain and solve disagreement between various theoretical studies and experimental results.

### 1.2.1 Two and three-body recombination

There are several types of electron-ion recombination processes and here we will consider only binary and ternary cases. The binary nature of the recombination process usually can be observed in low-density environments such as interstellar medium or experimental setups like ion storage rings.

$$N_2H^+ + e^- \xrightarrow{\alpha_{bin}} \text{neutral products,} \tag{3}$$

where $\alpha_{bin}$ is the binary dissociative recombination rate coefficient. Ternary recombination is a process that can be enhanced by a three-body reaction [26] which occurs in the presence of an ambient gas, for instance He as a buffer gas in our experiment.

$$N_2H^+ + e^- + He \xrightarrow{K_{He}} \text{neutral products,} \tag{4}$$

where $K_{He}$ is the ternary recombination rate coefficient. A tree-body recombination phenomenon (4) has been considered in detail for atomic ions [27, 28] and not so well for molecules [27, 29, 30, 31, 32]. The experimental data at room temperature or above mostly coincide with theoretical calculations [26, 33] with $K_{He} \approx 10^{-27}$ cm$^6$s$^{-1}$ at 300 K. On the other hand, $H_3^+$ ions or their deuterated isotopologues in helium buffer gas according to recent studies [34, 35, 36, 37, 38] have a much higher value of the ternary recombination rate coefficients on the order of $10^{-25}$ cm$^6$s$^{-1}$ at 300 K. Moreover, $H_3^+$ ions recombine even faster in $H_2$ buffer gas [39, 40]. These outcomes became a basis for the assumption that the three-body

recombination of $H_3^+$ passes through dissociation of long-lived excited intermediate states. $H_3^+$ isotopologues probably deionize in the same way [34, 35]. The recombination of diazenylium is indirect also and proceeds via excited Rydberg states [24]. That is why it is possible that the ternary process (4) also influences overall recombination of $N_2H^+$ ions in a buffer gas.

In the prof. Glosík laboratory we carried out an experimental investigation on recombination of diazenylium with electrons in the $N_2H^+$ dominated afterglow plasmas. The measurements cover rather a wide temperature range from 80 up to 350 K. The number densities of several rotational and vibrational quantum states of studied ions were determined by means of absorption spectroscopy. A possible impact of buffer gas number density on the measured rate coefficient of the recombination process was also studied.

# 1.3 $H_3^+$ investigation background

From the very beginning of XX century, $H_3^+$ ion became one of the most discussed ions in theoretical and experimental works. For the discovery of such an important and controversial ion, we should be grateful to Thomson [41], who in 1911 shows to the world $H_3^+$ by means of the early form of mass spectrometry. The formation of this molecular ion was described by Hogness and Lunn [42] in 1925 as a product of the reaction between $H_2^+$ ions and molecular hydrogen. Later in the same decade [43], it was revealed that the equilibrium structure of $H_3^+$ ions is the equilateral triangle. Only more than five decades after that, in 1980, the scientific community saw for the first time the absorption spectrum of $H_3^+$ thanks to the experimental studies which were made by Oka [44]. Even before the first experimental paper on the topic, $H_3^+$ was considered as crucial for the understanding of interstellar chemistry [45] due to this molecular ion being the most produced [46] and as a result most abundant ion species in the interstellar media. The presence of $H_3^+$ ions was later confirmed in different astrophysical environments including interstellar gas clouds, ionospheres of gas giants, and all the way to the galactic center [47, 48, 49]. The importance of this molecular ion to cosmic chemistry is substantiated by its ability to deliver a proton in the chemical ion-molecule reactions. Therefore, $H_3^+$ can act as a universal proton donor in space [46, 50].

Taking into account the abundance of $H_3^+$ ions and the variety of conditions that could be found in the Universe, $H_3^+$ can be regarded as an initiator of long chemical reaction chains which produce more complex molecular species [17]. Hence, the detailed study of the dissociative recombination of $H_3^+$ ions with electrons became one of the most important

building blocks in astrophysics [51]. The research on this topic has been continued for more than 70 years already [1].

The precise value of the rate coefficient of the dissociative recombination of $H_3^+$ ignited intense discussion and controversial opinions in the scientific community. The nonlinear history of experimental studies of the issue proposed the value of about $10^{-7}$ cm$^3$ s$^{-1}$ at 300 K according to the ion storage ring measurements [52, 53], whereas afterglow experiments (flowing and stationary afterglow) show the broad range of results from $1.8 \times 10^{-7}$ to $10^{-11}$ cm$^3$ s$^{-1}$ [15, 21, 54, 55]. The theoretical research made the situation even more entangled due to the prediction that the corresponding potentials do not have favorable curve crossings [56], which leads to a relatively low value of the rate coefficient for dissociative recombination. It was necessary to go beyond the Born-Oppenheimer approximation by invoking the Jahn-Teller mechanism with the latest theoretical calculations supporting the high value of the recombination rate coefficient [57, 58].

### 1.3.1 Three-body recombination of $H_3^+$

Finally, the phenomena of the fast three-body recombination of $H_3^+$ ions was found by the group under the guidance of Glosik [34] in the first decade of the XXI century. The discovery of the surprisingly fast He-assisted recombination process of $H_3^+$ gives the explanation to a lot of previously published results of afterglow experiments. The value of the ternary recombination rate coefficient of $H_3^+$, obtained by the Glosík research group, turned out about two orders of magnitude higher than the values predicted by theoretical calculation for atomic ions [26, 33]. Future experiments showed a similarly high value of helium-assisted three-body recombination for all deuterated isotopologues of $H_3^+$ [37, 38, 59]. Moreover, for the process of recombination of $H_3^+$ with electrons in the dihydrogen carrier gas was

observed even higher ternary recombination rate coefficient [39, 40]. It is important to notice here, that there are no data about the studies of the three-body recombination process of $H_3^+$ with electrons and other third-body species than $H_2$ or He. Only in the paper by MacDonald *et al.* [60] was studied recombination of $H_3^+$ ions in Ne-buffered plasma. However, the MacDonald group gives data for a very narrow pressure range, hence it is hard to evaluate the role of neon as a third-body assistant in the three-body recombination process.

According to the studies by the prof. Glosík group [34, 35], there is a possibility of the formation of excited neutral molecules with relatively long lifetimes as a result of collisions between $H_3^+$ with electrons. The lifetime of those neutral species can reach up to tens of picoseconds at the conditions in the common experiments with afterglow plasmas. This lifetime is long enough for additional collisions of the investigated neutral molecules with particles from the carrier gas. The fully quantum mechanical investigation on the issue of $H_3^+$ ions behavior during the third-body assisted recombination is still needed to be done for a deeper understanding of the process.

The purpose of the present study is to investigate in more detail the recombination process of $H_3^+$ ions with electrons in the Ne buffered afterglow plasmas. The new Cryogenic Stationary Afterglow experimental setup, equipped with a near-infrared Cavity Ring-Down Spectrometer (Cryo-SA-CRDS), was selected for the measurement implementation. CRDS provides absolute measurement of absorbance, hence no calibration is needed. In the first part of the present study, the approach for simultaneous measurement of electron and ion number densities will be described. The new method of calculation for the recombination rate coefficient of $H_3^+$ ions first will be shown based on the experimental data for the test case of He

buffered plasma. The upcoming phase of the research will demonstrate the application of the aforementioned approach to acquire a ternary rate coefficient of electron-ion recombination for the $H_3^+$ species in neon buffered plasmas. In this context, Ne serves as both the carrier gas and the third body partner in the three-body recombination reaction.

# 2  EXPERIMENTS

## 2.1 CRDS as a key for study $N_2H^+$ recombination

In order to measure the recombination rate coefficient [1, 36] of $N_2H^+$ ions a stationary afterglow (SA) apparatus was used. It was equipped with a continuous wave modification (CW) cavity ring-down absorption spectrometer (CRDS) for the purpose of time-resolved tracking of ion number densities decays of specific vibrational and rotational states of diazenylium. A scheme of CW-CRD spectrometer, based on the design described by Romanini *et al.* [61, 62], is shown in **Figure 3**. For a more detailed description of present CW-SA-CRDS and its application for electron-ion recombination studies see references [36, 63, 64, 65, 66].
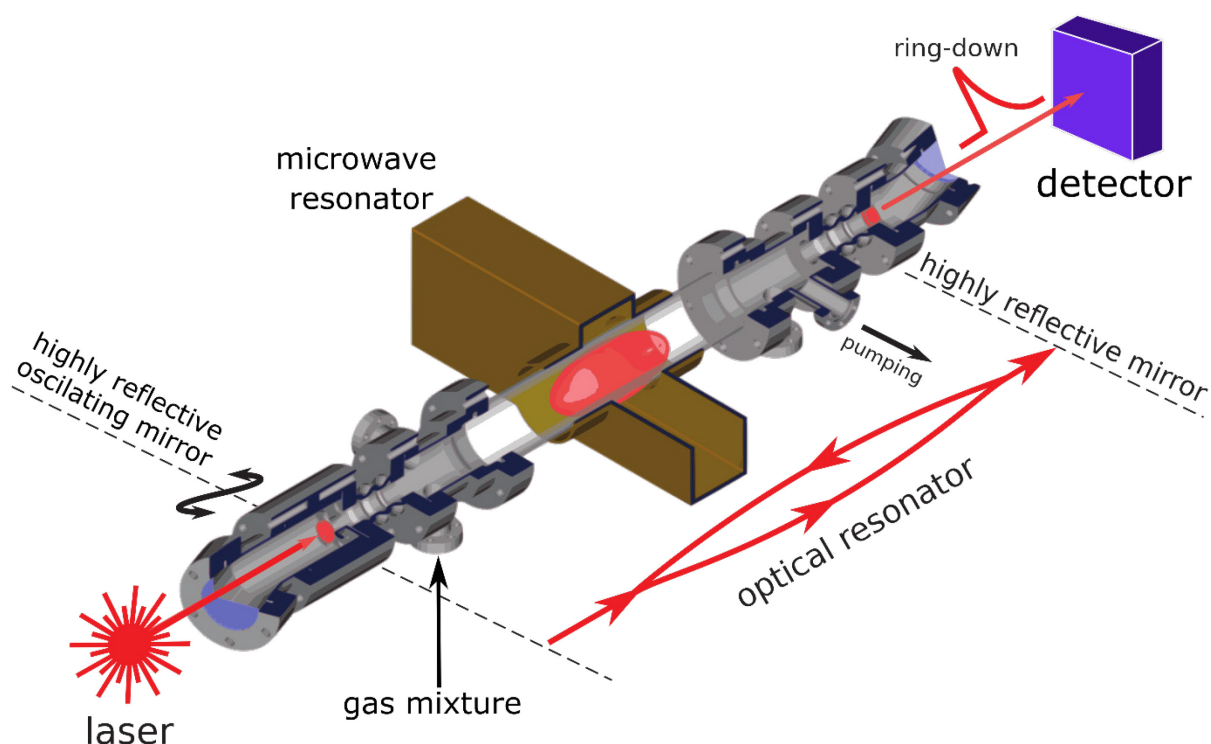


**Figure 3.** The schematic diagram of SA-CRDS experimental setup. To measure the concentration of ions, the SA-CRDS apparatus uses a

microwave discharge in a gas mixture to initiate plasma in optical resonator. This resonator contains two highly reflective mirrors, with an oscillating mirror used to establish resonance by injecting the laser light at random intervals. After injection, the laser light is turned off, and it travels effectively several kilometers in the cavity, being absorbed by the plasma. The gradual decrease of the recorded optical signal on the detector is known as ring-down, with a shorter ring-down event indicating a higher concentration of monitored ions due to increased absorption by the medium. The figure was adapted from reference [67].

A pulsed microwave (MW) discharge generates plasma in a fused silica tube with an inner diameter of about 12 mm. External switch, connected to the MW generator, is able to cut off high-voltage power towards magnetron with a fall time lower than 30 μs. With the aim of preventing exorbitant heating of the gas mixture during the discharge, a duty cycle was limited to $\approx 40\%$ at a microwave input power of $10 - 25$ W. The temperature ($T_{\text{tec}}$) of the silica discharge tube can be set and maintained in the range from 80 up to 350 K and is measured by means of a thermocouple attached to the outer surface of the tube near to discharge region. Within the measurement error, the tube temperature is equal to the rotational temperature of the investigated ions $T_{\text{rot}}$ and kinetic temperature $T_{\text{kin}}$. That will be demonstrated in the next chapter. The temperature of the fused silica tube will be utilized as nominal temperature $T$ in the experiment description. With the goal to cool down the discharge tube, liquid nitrogen or precooled $N_2$ gas are used. The plasma is ignited in the gas mixture based on helium ($10^{17}$ cm$^{-3}$) buffer gas. The admixtures are Ar, $H_2$, and $N_2$ with number densities of $10^{14}/10^{14}/10^{13}$ cm$^{-3}$, respectively. In the case of $H_2$ ambient gas ($(0.3 - 1) \times 10^{17}$ cm$^{-3}$), the density of the $N_2$ admixture is $\approx 10^{13}$ cm$^{-3}$. In the experiment, hydrogen was with an

"normal" ortho/para nuclear spin manifold ratio. That means, at room temperature, the *ortho*-$H_2$ to *para*-$H_2$ is 3:1. Later in the text there will be shown a table with the time constants in the model of chemical kinetics for the process of formation and recombination of diazenylium afterglow plasma.

## 2.1.1 Investigated transitions of $N_2H^+$ ions

Like in the CRDS papers of our group on the topic of electron-ion recombination [63, 64, 65, 66], for the $N_2H^+$ vibrational states description we will use the same symbols ($v_1v_2^lv_3$). The numbers of vibrational quanta in their normal mode are denoted here by $v_1$, $v_2$, and $v_3$. The letter "*l*" indicates the quantum number associated with the vibrational angular momentum corresponding to the doubly degenerate bending mode. With the view to probe the changes in rotational and vibrational state populations of diazenylium, the overtone transitions were used. For $N_2H^+$ ions transitions from the ground vibrational state (000) were chosen. The transitions originating in the first excited vibrational state of diazenylium ($01^10$) were also utilized.

The **Table 1** summarizes all transitions that were used in the present work. In order to estimate the production of $NH_3$ in the discharge plasma, two ammonium transitions were scanned. The positions of the lines (6314.1334 cm$^{-1}$ and 6314.4382 cm$^{-1}$) were taken from the HITRAN database [68].

The reaction of $NH_3$ with $N_2H^+$ ions proceed quickly ($k_{NH3}$ = 2.3 × 10$^{-9}$ cm$^3$s$^{-1}$) and produces $NH_4^+$ ions [69]. According to measurements, the number density of $NH_3$ in the gas mixture and buffer gas was lower than 5 × 10$^{11}$ cm$^{-3}$. At least 900 μs was the characteristic time for the reaction between $N_2H^+$ and $NH_3$ resulting in the formation of $NH_4^+$ ions. In order to estimate

the production of $NH_4^+$ in our experiment, the computer model of chemical kinetics was developed. The model shows that at a number density of $NH_3$ equal to $5 \times 10^{11}$ cm$^{-3}$ the number density of $NH_4^+$ in the early afterglow plasma will not be higher than 3% of all ionized species.

**Table 1.** List of the transitions in the $(200) - (000)$ and $(21^10) - (01^10)$ vibrational bands of $N_2H^+$ ($v_{exp}$) that were utilized in the present investigation. The line positions were taken from reference [70]. The errors of the measurement are given as a number in the parentheses in units of the last quoted digit. All transitions are marked by the appropriate branch (R or P) and by the rotational quantum number of the lower state. The letters $e$ and $f$ in the upper indices show parity.

| Transition | Band | $v_{exp}$ (cm$^{-1}$) |
|:---:|:---:|:---:|
| **P(8)** | $(200) - (000)$ | 6310.3902(2) |
| **P(7)** | $(200) - (000)$ | 6313.8544(2) |
| **P(6)** | $(200) - (000)$ | 6317.2682(2) |
| **P(5)** | $(200) - (000)$ | 6320.6311(2) |
| **R(9)$^f$** | $(21^10) - (01^10)$ | 6317.2450(11) |
| **R(9)$^e$** | $(21^10) - (01^10)$ | 6317.4329(20) |
| **R(10)$^e$** | $(21^10) - (01^10)$ | 6319.7976(6) |

## 2.2 New Cryo-SA-CRDS apparatus for study dissociative recombination of $H_3^+$ ions in He or Ne ambient gases

The present measurements were carried out by utilizing the new Cryogenic Stationary Afterglow experimental setup in conjunction with a near-infrared Cavity Ring Down Spectrometer (Cryo-SA-CRDS). A detailed description of this apparatus is given in the Reference [71] and only a simplified scheme is shown in the **Figure 4**. The working principle of our experimental setup is based on a continuous wave Cavity Ring-Down Spectroscopy (CW-CRDS) which was developed and described for the first time by Romanini *et al.* in the paper [62]. This technique allows us to make time-resolved probing of the ion number density of investigated species in order to evaluate the time evolution of the number density of these ions in the discharge time and in the afterglow plasmas.

### 2.2.1 CRDS for ion number densities measurements

The microwave discharge in a gas mixture is ignited in the monocrystalline sapphire tube. The length and inner diameter of the discharge tube are 20 cm and 2.5 cm respectively. Monocrystalline sapphire as a material for the tube was chosen due to its high thermal conductivity at the measurement conditions. The main part of the CRD spectrometer is a pair of highly reflective plano-concave mirrors (reflectivity typically exceeds 99.99%) which are situated on the inlet and outlet of the discharge tube and consequently form a cavity where Ring-Down will occur. The distance between the mirrors in our case is 82 cm, which makes harder the alignment of the cavity on one side, but ensures protection of the mirror surfaces from contamination and plasma erosion on the other side.
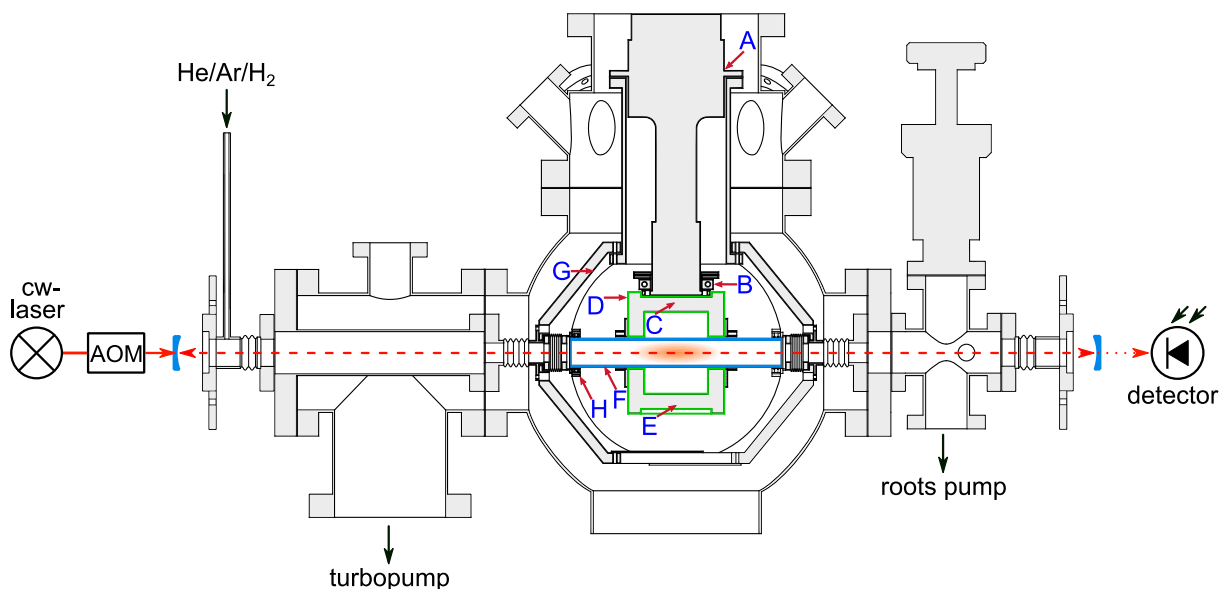
**Figure 4.** The Cryogenic Stationary Afterglow experimental apparatus equipped with a continuous wave Cavity Ring-Down Spectrometer (Cryo-SA-CRDS). The capital letters represent the position of temperature sensors such as platinum resistors and silicon diodes. The discharge region is marked by an orange cloud in the middle of the blue rectangle which represents the sapphire gas discharge tube. The cylindrical microwave resonator is drawn as a green frame around the discharge tube. The upper part of the aluminium microwave resonator is connected to the cold head Sumitomo RDK 408S. For the fast switching on/off laser beam, the acousto-optic modulator (AOM) is used. After the AOM the laser beam enters the optical cavity through the first plano-concave mirror, then passes the entire lengths of the discharge tube including the plasma region (orange), and then through the second mirror beam reaches the photodiode (marked as a detector). The figure was adapted from reference [72].

In order to form a laser beam with the needed wavelength of 1381 nm the distributed feedback (DFB) laser diode was utilized. The chosen light

source, with the necessary wavelength in the middle of the irradiation spectra, must cover the second overtone transitions originating from the lowest energy para and from the two lowest energy ortho rotational states of $H_3^+$. EXFO WA-1650 wavemeter ensures the precise measurement of the laser beam wavelength. The optical cavity leak of light from the second plano-concave mirror is collected by the InGaAs avalanche photodiode.

The plasma for the formation of $H_3^+$ ions is created by the microwave discharge which is ignited in the gas mixtures such as $He/H_2/Ar$ or $Ne/H_2/Ar$ with the typical particle number densities $10^{17}/10^{14}/10^{14}$ $cm^{-3}$, respectively. The velocity of the flow of He or Ne buffer gases was $\approx 1$ m $s^{-1}$. Those carrier gases were purified before the discharge tube inlet by applying a series of cold traps which were cooled by liquid nitrogen. The chemical kinetics of He buffered plasmas with the Ar and $H_2$ admixtures were detailly described in the paper [40]. The Ne buffered plasma as a medium for $H_3^+$ ions formation will be described later in the present work.

The cylindrical solid-state microwave resonator does not have movable parts. It consists of two aluminium blocks around the sapphire discharge tube. The glow microwave discharge is ignited by tuning the frequency of the microwave radiation to the resonance frequency of the cylindrical cavity of the microwave resonator with utilizing the $TM_{010}$ mode. To tune the microwave radiation frequency in the range from 2.4 to 2.6 GHz the solid-state MW source was installed. The output power of the MW radiation source was up to 20 W and the switching time does not exceed 1 μs (a more detailed description is in Reference [71]).

## 2.2.2 Cryogenic system

The intelligent cooling system of the apparatus is started from the upper block of the microwave resonator which is connected to the second stage of

cold head Sumitomo RDK 408S. The utilization of a cold head enables measurements to be conducted within the temperature range of 30 – 300 K [71, 73]. The aluminium body of the upper part of the resonator, in turn, is connected to the monocrystalline sapphire discharge tube by means of a system of copper braids. The mirrors which form a cavity for the Ring-Down spectrometer, and the discharge tube with the microwave resonator, and both stages of the cold head are situated inside the external vacuum chamber to ensure thermal insulation. The vacuum system, consisting of a Pfeiffer Vacuum turbopump and a membrane fore vacuum pump, ensures that the pressure inside the external vacuum chamber remains below $10^{-4}$ Pa. The external vacuum chamber also does not have any glass windows in order to prevent the heating transfer from the laboratory to the discharge regions. Moreover, the discharge tube and the microwave resonator aluminium cube are hidden inside the "pocket" of the heat shield which consists of several aluminium plates. The heat shield is attached to the first stage of the cold head, aiming to minimize the influence of radiative heating on the region of the gas discharge tube.

### 2.2.3 Microwave diagnostics for electron number densities measurements

With the purpose to get direct information about the evolution of electron number densities, the time-resolved microwave diagnostics was implemented in the Cryo-SA-CRDS apparatus (see **Figure 5**). The MW diagnostic is based on the method where the shift in the resonance frequency of the resonator can be transformed by calculation into electron number density value [74]. The electron number densities $n_e$ on the axis of the Cryo-SA-CRDS discharge tube can be calculated utilizing the measured shift of

the resonance frequency of the cylindrical resonator by means of the formula:

$$n_e(r = 0) = \Delta f_r f_r \frac{2\pi m_e}{e_0^2} \frac{\int_V E^2 dV}{\int_{V'} J_0\left(\frac{2.405}{r_1} r\right) E^2 dV}.$$
(5)

Here, $\Delta f_r$ represents the shift of the resonance frequency caused by a difference in the dielectric permittivity of the microwave resonator as a result of electrons present in plasma. $f_r$ denoted the resonance frequency of the MW resonator. The intensity of the high-frequency field in the MW resonator is marked by $E$. The volume of the MW resonator and the volume of the investigated plasma are marked as $V$ and $V'$ respectively. $J_0$ plays the role of the Bessel function of zeroth order. The electron mass and charge are marked as $m_e$ and $e_0$ respectively. The inner radius of the discharge tube is marked by $r_1$ whereas $r$ represents a distance from the axis [75]. The calculation of the resonant frequencies of the cylindrical cavity of the MW resonator was done by Dr. Roučka by utilizing an equivalent circuit finite difference time domain method [76, 77] as implemented in the openEMS software [78]. Other characteristics for Equation (5) were determined by means of the same software based on the actual geometrical parameters of the resonator cavity taking into account inserted sapphire tube and applying 3-dimensional cylindrical mesh. A detailed description of the calculations was published in Reference [71].

The solid cube made out of aluminium forms a microwave resonator with the shape of a cylindrical cavity inside (see **Figure 6**). The rotational axis of the cylindrical MW cavity coincides with the axis of the optical cavity of the CRD spectrometer. The MW resonator does not have any movable parts. The two loops of MW antennas are inserted in the MW cavity on the

opposite sides of the resonator around the discharge tube. The first antenna delivers high RF power, about 20 W, in order to ignite glow discharge in the gas mixture and as a result to form plasma inside the microwave and optical cavity. The second mission of the first antenna is to probe the resonance frequencies of the MW cavity by low input power of about 1 mW. The second antenna transmits microwave power from the cylindrical MW resonator to the MW detector while the first antenna works as a probing device.
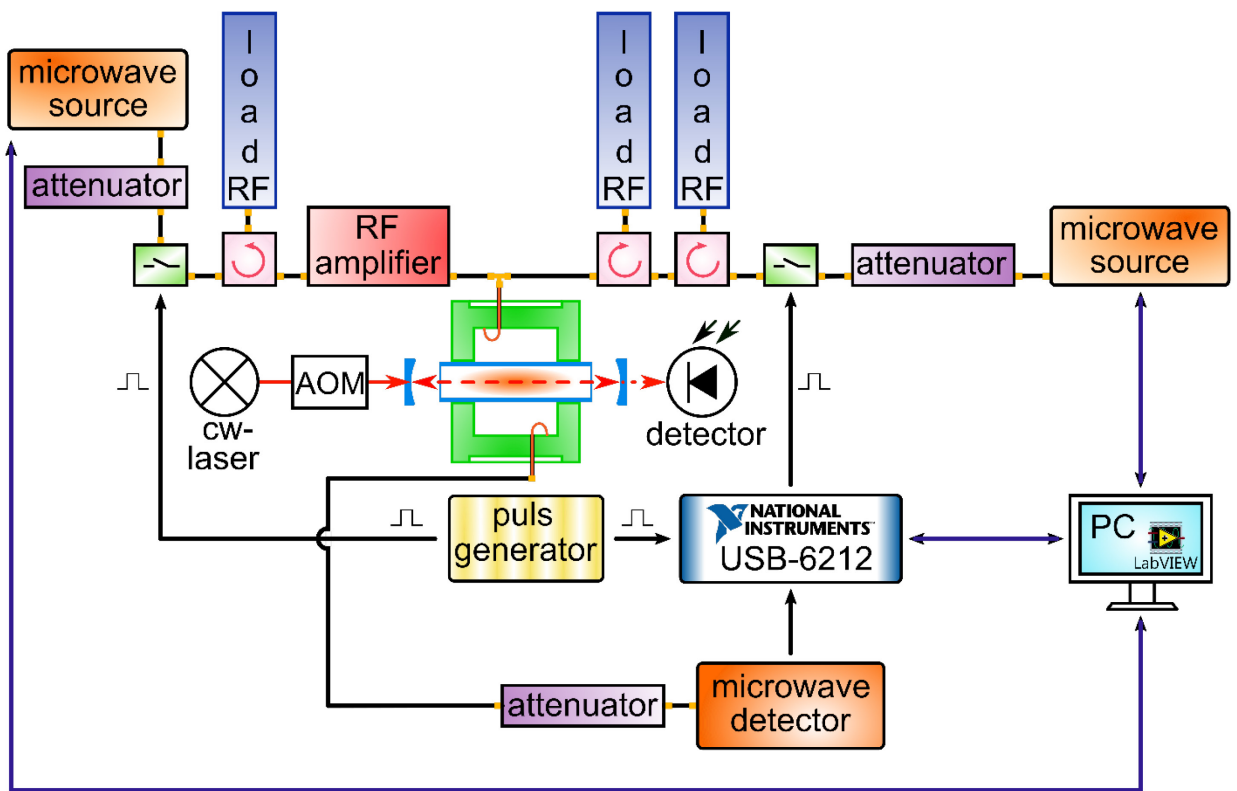


**Figure 5.** The schematic diagram of microwave system for MW diagnostics of plasmas in Cryo-SA-CRDS. Within the blue rectangle denoting the sapphire gas discharge tube, the MW discharge zone can be identified by the presence of an orange cloud of plasma. The solid and dashed red lines in the diagram represent the path of the laser beam, which starts from the continuous wave (CW) laser and passes through the acousto-optic modulator (AOM) before entering an optical cavity composed of a pair of

high-reflective planoconcave mirrors (denoted by light blue brackets on both sides of the discharge tube). Following the optical cavity, the laser light leaks onto a detector, represented by the photodiode symbol in the figure. The discharge tube is encircled by a green frame that represents the cylindrical microwave resonator. The MW resonator is marked by orange semicircles at the top and bottom, which represent the loops of the MW antennas. These antennas are located on the inner surface of the MW resonator, around the discharge tube opposite to each other. The antenna connected to the top part of the MW resonator (labeled as "A" in **Figure 6**) delivers MW power to the MW cavity from the two MW sources (represented by orange rectangles at the top of the diagram), while the antenna connected to the bottom part of the MW resonator aim to deliver a probing MW signal to the MW detector (represented by an orange rectangular at the bottom of the diagram). The violet blocks on the path of microwaves denote attenuators that allow us to adjust the generated MW power to the desired level to ignite the discharge in the MW resonator or avoid damaging the MW detector. The white blocks with a light green corner and an electrical key symbol inside represent the PIN switch devices that serve as fast switching valves for microwaves from sources to the MW cavity. The rose squares with the circle arrow inside display the circulator devices, which aim to prevent the backflow of microwaves to the sources and avoid damaging them. The circulators are connected to the RF loads (dark blue rectangles), which can safely transform back-reflected MW power into ohmic losses. The RF amplifier (red block) increases the MW power to reach the essential level of energy (20 W) on the TM010 mode of the MW cavity for plasma ignition out of a gas mixture in a sapphire tube. The white block with the yellow blurred lines represents the pulse generator unit, which synchronizes the MW delivery and measurement process by generating transistor-transistor-logic (TTL) pulses with a level of 5 V. The TTL signals are marked as single histogram peaks above the

communication arrows, which denote BNC cables (black lines with arrow endings), while the SubMiniature version A (SMA) cables for MW power transport are marked as black lines with yellow block endings. The Universal Serial Bus (USB) communication lines are displayed as dark deep purple lines with arrow endings. The National Instrument USB 6212 multichannel device manages the TTL signals and transfers measured data to the Personal Computer (PC). The whole process of plasma ignition, together with the CRDS and MW diagnostics measurements, is controlled by several PC programs that were developed by our scientific team using the graphical programming environment LabView$^{TM}$.
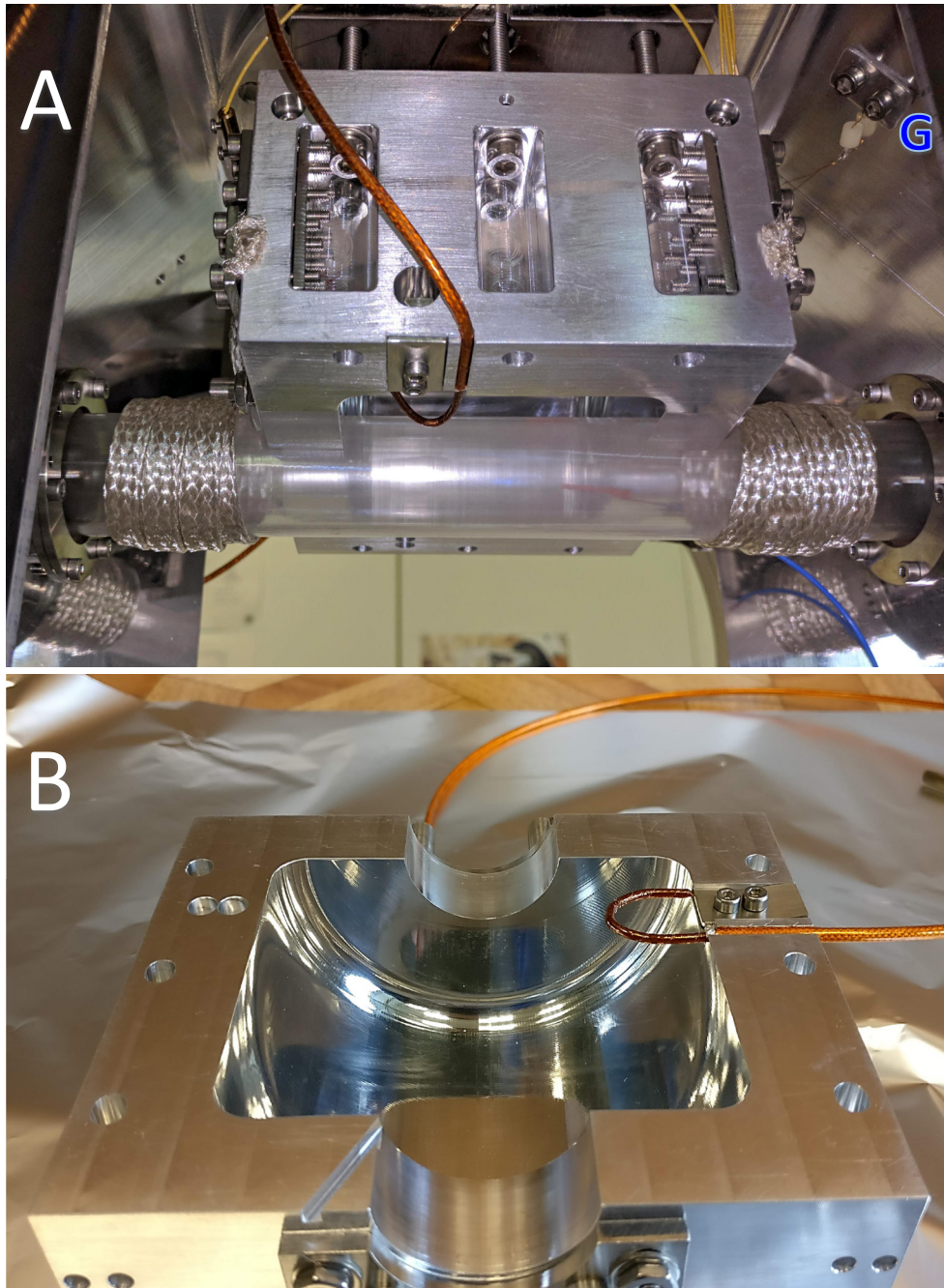
**Figure 6.** Panel A of the figure shows the photo of the upper part of the microwave resonator, consisting of an aluminium block in tight contact with the second stage of the Sumitomo RDK 408S cold head. To ensure reliable heating contact of the monocrystalline sapphire tube to the cooled aluminium block, the upper part of the MW cavity is connected to the gas discharge tube via copper braids with silver coating. The inlet and outlet of the discharge tube are fixed by vacuum bellows on the walls of the heating shield, which covers the entire MW resonator together with the discharge tube to prevent

heat leaks to the discharge region. The first stage of the cold head is attached to the ceiling of the heat shield. The panel also shows the location of the MW antenna (dark orange wire) which delivers power to the MW cavity from the two MW sources. The yellow wires on the top of the figure represent connections to the heating elements. The Pt resistance temperature detector (RTD) made by Cryo-Con, model XP-1K, is labeled as the G spot in the upper right corner of panel A, and the positions of other temperature sensors are shown in **Figure 4**. Panel B displays the photo of the lower part of the MW resonator, with the well-recognizable cylindrical form of the inner cavity. The loop antenna for MW diagnostics is denoted by the orange wire with the dark orange loop and is connected to the MW detector (ZX47-40-S+ power detector from Min-Circuits).

Low input power for MW diagnostics is yielded by a similarly solid-state synthesizer as used for high-power input MW but without the amplifier. The synthesizer SLSM5 is produced by Luff Research Inc for the output MW with frequencies in the range of 2.4 GHz to 2.6 GHz. Before the entrance to the MW resonator, the microwaves are controlled by a fast absorptive PIN switch. The role of the PIN switch fulfills diode SR-DA10-15 made by Universal Microwave Components Corp. The detailed description of the microwave detection unit is shown in **Figure 7**.
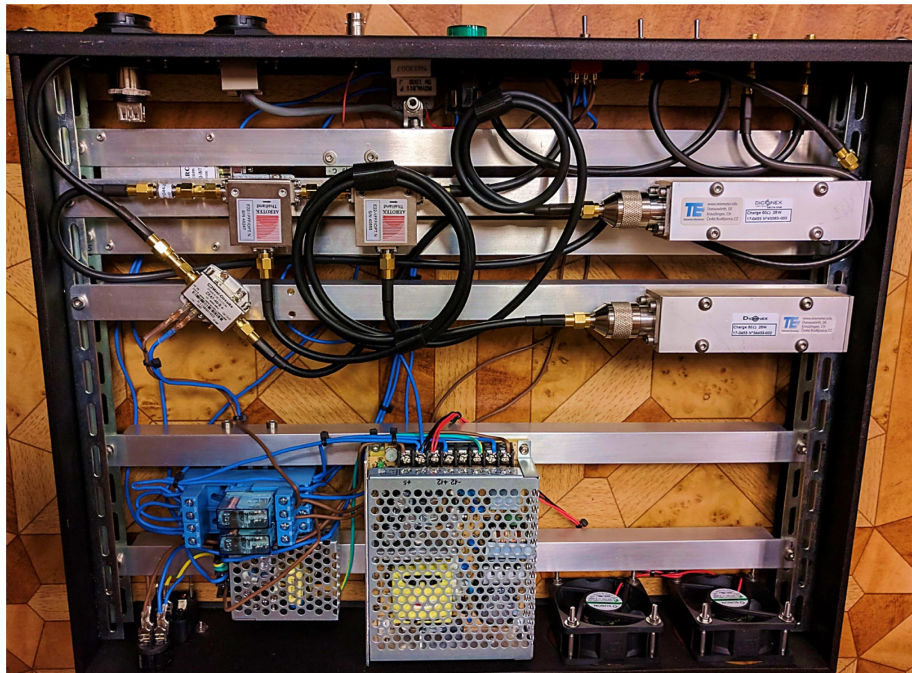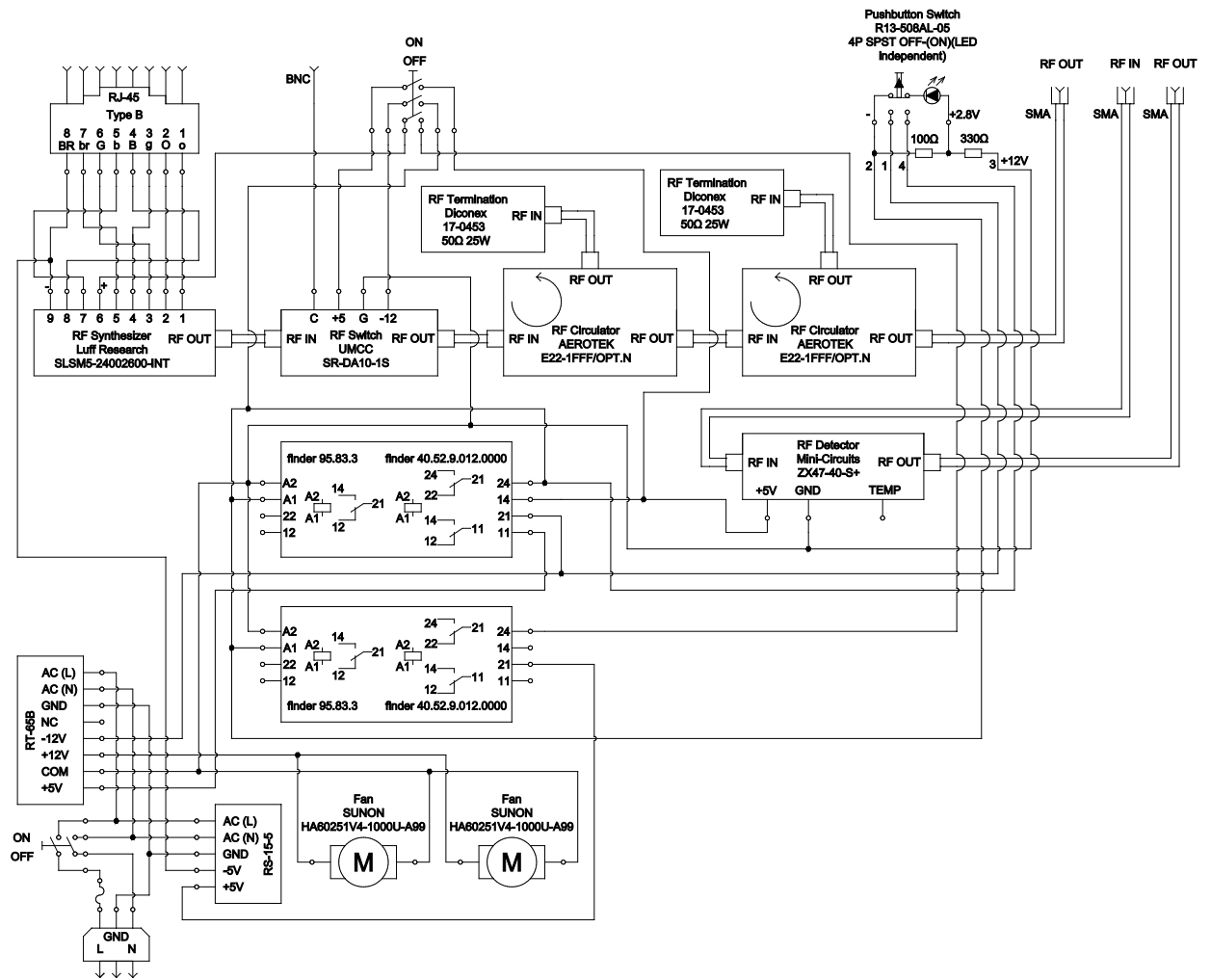
**Figure 7.** Schematic diagram and a photo of the measurement unit used for microwave diagnostics of plasmas in the Cryo-SA-CRDS apparatus. This

unit, marked as MW Detector Box in **Figure 9**, comprises a solid-state microwave source from Luff Research, marked as RF synthesizer here, with the model number SLSM5-24002600INT. All communication channels of the RS485 output of the synthesizer are connected to the RJ-45 type B output of the box. Additionally, PINs number 6 and 9 of the RS485 serial port connector are connected to a separate power source, RS-15-5 from Mean Well, through a relay. The 12V DC coil non-latching relay with Double Pole Double Throw (DPDT) switch, model 40.52.9.012.0000 from the brand Finder, is mounted on the 8-PIN screw terminal socket, model Finder 95.83.3. The separate power source ensures stable operation of the RF synthesizer and minimizes noise in the generated microwave signal. The connection of the microwave source to the PC is illustrated in **Figure 9**. In the photo, the RF synthesizer is hidden under the aluminum rails, and only the capital letter "RC" from its label is visible in the top left corner of the box. Another output of the RF synthesizer has an SMA connector that transmits microwaves to the RF switch (marked as PIN switch in **Figure 5**), SR-DA10-1S made by UMCC. This device can conduct or stop microwaves depending on the input TTL signal, which it receives directly from the BNC input connector on the front panel of the MW Detector Box. In the photo, the device is hidden under the aluminum rail, and it can be located by tracing the red wire that connects the BNC input with the RF switch in the top part of the photo. Only the corner of the device with the reversed "c" letter is visible. The microwaves from the SMA output of the RF switch are directed to a series of two RF circulators from AEROTECH, model E22-1FFF/OPT.N, which prevent the backflow of microwaves and protect the RF synthesizer. In the photo, the small arrows to the right in the label of the square-shaped shells of the circulators indicate the main direction of the RF wave through them. There may be a possible backflow of RF power from the microwave resonator, which the RF circulators redirect to the two RF terminations

(denoted as RF loads in **Figure 5**). These devices are made by Diconex and are model 17-0453. Each RF coaxial termination can absorb up to 25 W of microwave power and transform input energy into ohmic losses. The pair of massive metal blocks in the top right corner of the photo represents the termination set. The SMA output of the second circulator is connected to the SMA output connector on the front panel of the MW Detector Box, located in the top right corner of the photo. The microwave input and output SMA connectors leading to the MW detector are also situated on the front panel of the MW Detector Box next to the SMA output of the second circulator (synthesizer line). All three SMA connectors on the front panel have corresponding labels (synthesizer – top connector, detector input – bottom left, detector output – bottom right) to make it clear how to plug wires from antennas in vacuum chambers to the MW Detector Box. The ZX47-40-S+ RF power detector, produced by Mini-Circuits, operates within a range of -40 dBm up to +20 dBm (0.1 μW – 0.1 W). The power of the microwave signal used for MW diagnostics is approximately 1 mW, and its frequency is around 2.44 GHz, which falls within the operating range of the MW detector (0.001 – 8 GHz). The input and output of the MW detector are represented by SMA connectors. However, the input requires an RF power source, while the output provides a DC signal within the range of 0.5 to 2.1 V. This allows for safe transmission of an output signal to the NI USB6212 using a BNC cable, as shown in **Figure 9**. The output of the temperature sensor in the MW detector is not connected due to the low level of the input MW signal and the sufficient cooling system. The cooling system of the MW Detector Box comprises passive and active elements, including a pair of fans and aluminum rails. The aluminum rails not only provide a structure for holding all the microwave and electrical components in place, but also aid in effective heat dissipation due to the high thermal conductivity of aluminum. The active part of the cooling system consists of a pair of cooling fans

(identified as electric motors in the diagram) from SUNON, model HA60251V4-1000U-A99, which can be seen in the bottom right corner of the photo. The fans are $60 \times 60 \times 25$ mm in size, run on 12 V DC, and operate at 2500 Revolutions Per Minute (RPM) while producing a low noise level of 13.8 dB. These fans can effectively cool not only the existing components but also those that may be added in the future. For example, a future upgrade may allow the MW Detector box to generate microwaves sufficient for igniting the discharge in the CRDS discharge tube. In this case, the RF amplifier would be installed right in front of the fans for effective cooling. This possible upgrade is also the reason why the photo shows more buttons and outputs on the box than what is shown in the diagram, which only describes the existing MW diagnostics part. The Micro Wave Detector box was designed as a standard box for a 19-inch rack, making it easy to install in the laboratory.

With the aim to measure the shift in resonance frequency of the MW resonator, every discharge cycle the synthesizer was tuned to the specific probing frequency and switched on at several time intervals from the beginning of the discharge. The switching on time was not longer than 10 microseconds in order not to overheat electrons in the plasma. This approach allows us to track the full-time evolution of the resonance frequency of the microwave cavity during the whole afterglow process and at the same time prevent the undesirable influence of measurement instruments on the internal plasma processes during the afterglow. **Figure 8** shows an example of the time evolution of the resonance frequency of the microwave cavity as a response to the decreasing electron number densities in the afterglow plasma.
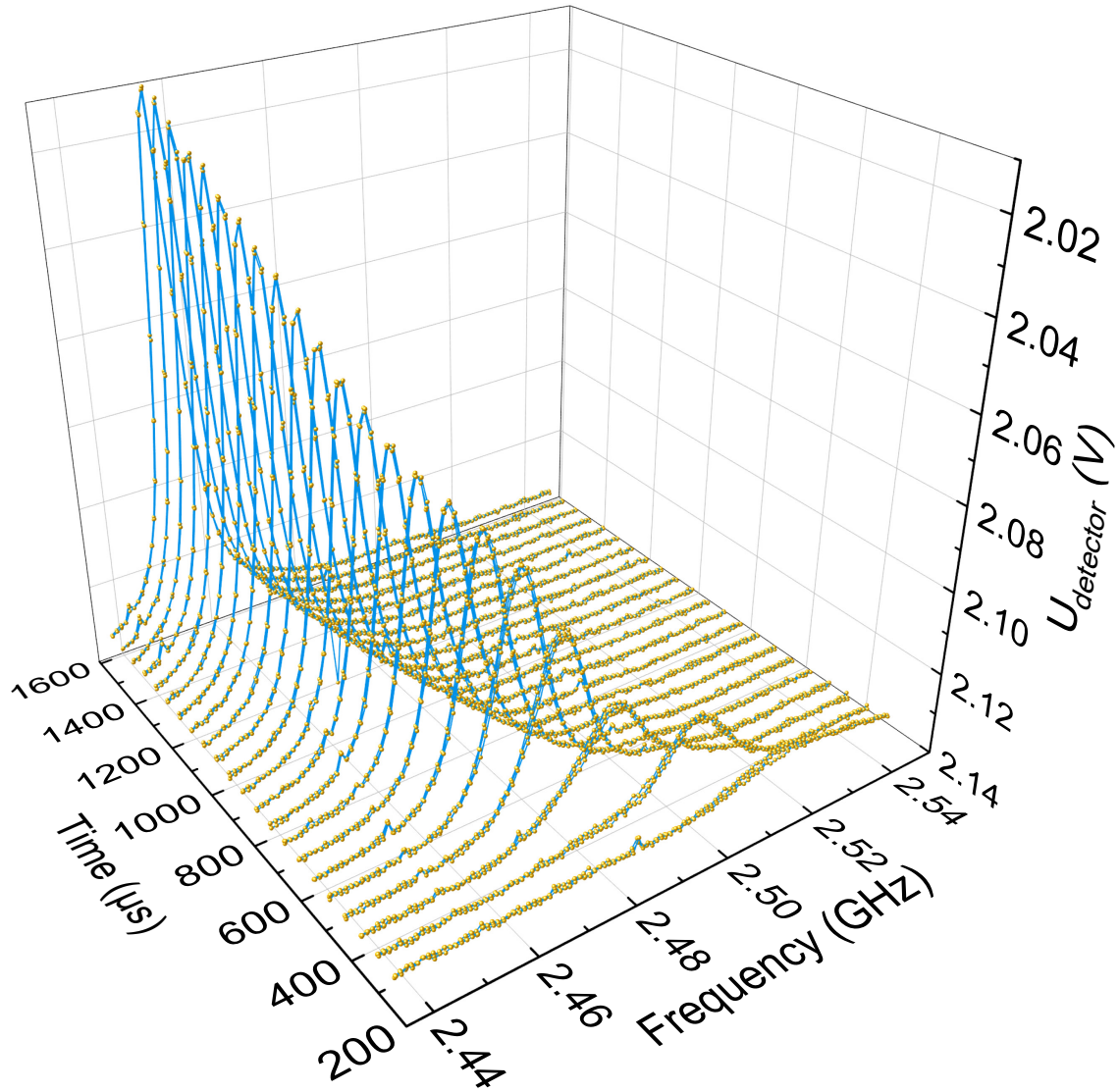
**Figure 8.** Time evolution of the resonance frequency of microwave cavity as a response to the decreasing electron number densities in the He-based afterglow plasma at $T = 200$ K. The gas mixture consists of $[He] = 3 \times 10^{17}$ cm$^{-3}$, $[H_2] = 4.6 \times 10^{13}$ cm$^{-3}$, $[Ar] = 2 \times 10^{14}$ cm$^{-3}$. The positions of the centers of the peaks in the graph give the values of resonant frequencies of the MW resonator at a certain time in the afterglow, which can be transformed into electron number density by applying Equation (5).
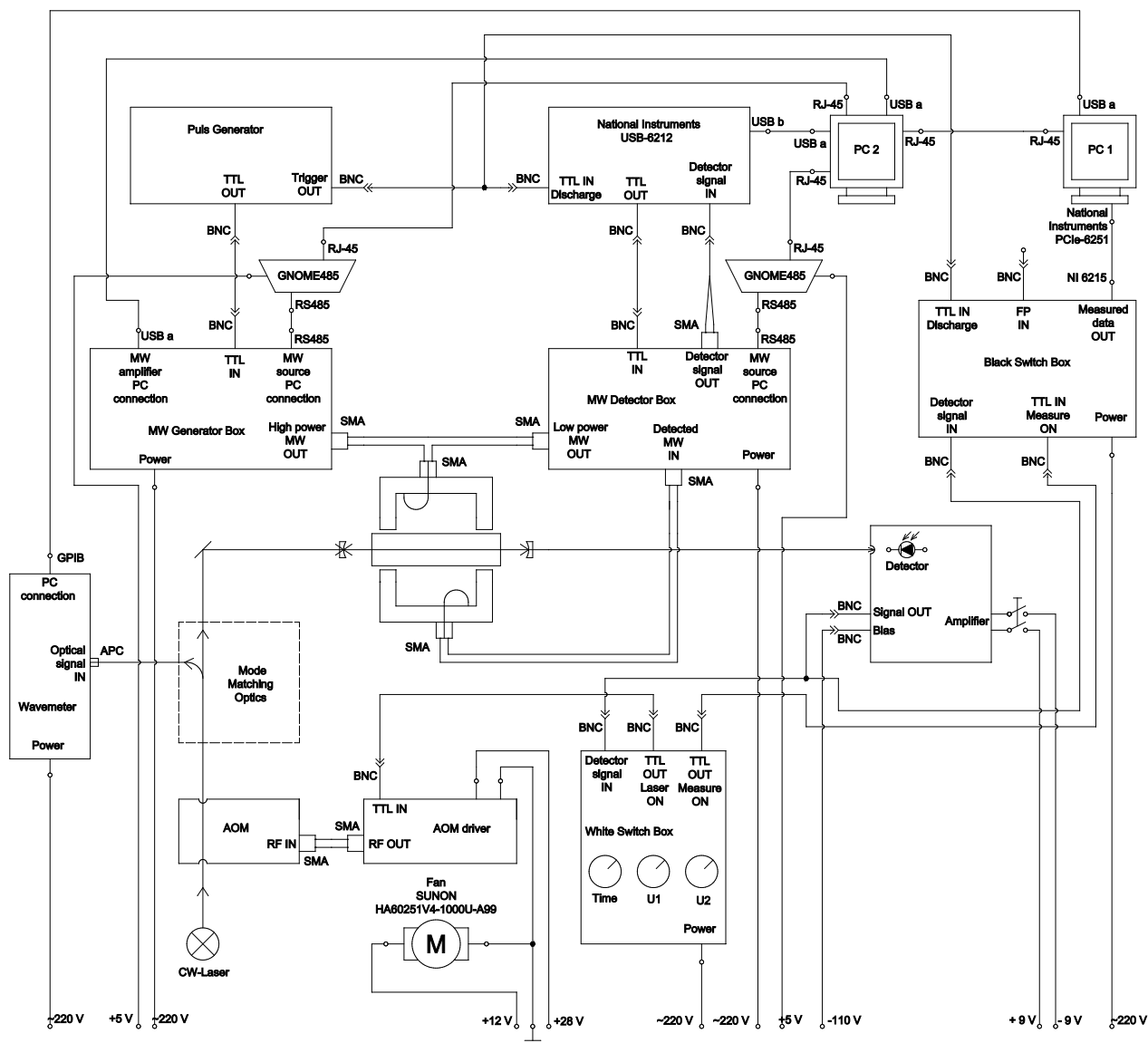
**Figure 9.** The primary layout of the Cryo-SA-CRDS measurement system in conjunction with the microwave diagnostics setup. The experimental setup is initiated using a commercial Pulse Generator, model TG2511A from AIM-TTI, located in the top left corner of the figure, which sends two TTL signals simultaneously with a frequency of about 330 kHz. The first signal, which typically lasts for about 218 μs and approximately 7% duty cycle, is transmitted through a coaxial cable with BNC connectors to the MW Generator Box, while the second signal, approximately 50% duty cycle, is transmitted to the National Instruments USB-6212 multichannel

device. The NI USB device then redirects the signal to a LabView-based program on PC 2 via a USB communication channel. The first TTL signal received by the MW Generator Box opens the PIN switch inside the box, allowing microwaves to pass from a solid-state MW source to the MW amplifier situated in the same box. The MW amplifier communicates with PC 2 through a USB A connector on the front panel of the MW Generator Box. The solid-state MW source utilizes the RS485 protocol for communication, and this signal is transmitted out from the RJ-45 connector to the GNOME485 converter. The GNOME485 device converts the signal from RS485 protocol to Ethernet protocol and then delivers it to PC 2 via an internal laboratory network. The LabView-based program running on PC 2 allows us to adjust the frequency of the generated microwaves, typically within the range of 2.435 GHz to 2.488 GHz. This enables us to identify the resonance frequency of the microwave resonator under ongoing experimental conditions and to trigger plasma ignition in the gas discharge tube. The high-power microwaves, with a power of approximately 20 W, are emitted from the SMA connector on the front panel of the MW Generator Box and delivered to the SMA vacuum connector through a coaxial cable. The SMA connector leads to the loop antenna, which is connected to the top part of the microwave resonator (refer to **Figure 6**, panel A). Information regarding the second TTL signal is relayed to the LabView-based program on PC 2. The program then initiates a delay that lasts for as long as the duration of the first TTL signal, allowing for discharge ignition and subsequent measurements in the afterglow plasma. After the delay, the program sends a signal to the NI USB-6212, which in turn sends a TTL signal to the PIN switch in the MW Detector Box (as described in detail in **Figure 7**). The MW Generator Box and MW Detector Box share the same loop antenna as an inlet for microwaves into the MW resonator. However, they are designed to operate independently of each other to prevent damage

to the MW sources and the MW detector unit. This is ensured by a LabView-based program and an NI USB-6212 device. As the MW Detector Box uses the same solid-state microwave source model as the MW Generator Box, the communication process with PC 2 is established in the same manner, with the use of GNOME485. The data measured using the MW Detector Box is first transmitted to the NI USB-6212 multichannel unit and then to the LabView-based program developed in our laboratory specifically for MW diagnostics of electron number density in afterglow plasmas. To obtain information about ion number density in the plasma, CRDS measurements are initiated. The same MW Generator Box is used to ignite the plasma, but in this case, the Trigger output signal from the Pulse Generator is also transmitted to the Black Switch Box (located in the middle of the right side of the diagram). When a pulse is received by the TTL IN Discharge of the Black Switch Box, PC 1 is notified that the discharge has been ignited to enable synchronization between discharge time and ring-down time during data processing. A ring-down is the duration of the exponential decay of the accumulated light intensity inside an empty cavity until it reaches zero. This decay is caused by gradual leakage of the light during over 100,000 round trips of the laser beam between the first planoconcave mirror and the second, and then back to the first. The typical characteristic time of a ring-down decay is tens of microseconds, with each roundtrip taking around 5 nanoseconds. To obtain ring-down data, the laser must first be turned on. We use continuous wave (CW) DFB (distributed feedback) or ECD (external cavity diode) laser diodes with optical power ranging from 1 to 100 mW for near-infrared measurements. The laser beam passes through an Acousto-Optic Modulator (AOM) and then hits a beam splitter. The first beam is directed to a collimator that couples optical irradiation to an optical single-mode fiber with an APC connector on the end. This connector is then plugged into the optical input of the Wavemeter model WA-1650 from

EXFO. The Wavemeter sends the data, including the current wavelength and optical power, to PC 1 using the Institute of Electrical and Electronics Engineers (IEEE) Standard number 488 via its General Purpose Interface Bus (GPIB) output. The data collected from the Wavemeter is synchronized with the discharge data using a lab-developed LabView-based program on PC 1. The second beam, which follows the beam splitter, is directed to the Mode Matching Optics to achieve the correct optical coupling with the 820 mm long optical cavity. The two mirrors of the optical resonator, which have diameters of 7.75 mm or 12.75 mm, are made from fused silica by LAYERTEC GmbH and have a reflectivity higher than 99.99% in the desired wavelength regions (700 – 900 nm or 1250 – 1450 nm), ensuring that the characteristic time of the ring-down decay is approximately 200 μs. Each ring-down event results in the leak of optical energy to the detector, which consists of an InGaAs avalanche photodiode with a sensor surface area of approximately $1 \, mm^2$ with an amplifier. The analog signal, which characterizes the voltage of the optical power leak to the photodiode, is transmitted to the White Switch Box. When the analog signal reaches the required U1 level, the White Switch Box stops sending the TTL signal to the Acousto Optic Modulator driver (AOM driver) through the BNC connector TTL OUT Laser ON. After the White Switch Box stops sending a TTL signal to the Acousto Optic Modulator (AOM) driver, the AOM model AA.MGAS80/A1 made by AA Opto-Electronic will stop operating, causing it to cease sending RF output signal to the AOM. Consequently, the AOM will no longer generate a diffracted laser beam that goes into the optical cavity of the CRD spectrometer. This will cause the built-up optical power in the optical resonator to start decreasing due to plasma absorption processes and mirror-reflecting losses, including leaks to the photodiode detector through the second planoconcave mirror. As a result, the analog signal from the detector will decrease. When the analog signal becomes

stable and drops below the U2 level, the White Switch Box will send a TTL signal from the BNC output connector TTL OUT Measure ON to the TTL IN Measure ON input BNC connector of the Black Switch Box. At this point, the Black Switch Box will start reading data from the input Detector signal IN, which is directly connected to the Detector output signal OUT that transmits an analog signal from ring-down events. The analog signal data then go to PC 1 with the help of an analog-digital (AD) converter built into National Instruments PCIe-6251 16-Bit Multifunction Data Acquisition (DAQ) Module. This DAQ board provides 16 single-ended analog input channels with 16-bit resolution and maximum sample rates of 1.25 MS/s. The data will be processed in the LabView-based program and saved on PC 1. After the waiting delay time set by the Time knob on the front panel of the box, the White Switch Box will resume sending the TTL OUT Laser ON signal to the AOM driver, which causes a diffracted laser beam to appear, and the process of CRD measurements begins again. To ensure a full day of continuous measurement on the Cryo-SA-CRDS apparatus, the cooling fan Sunon HA60251V4-1000U-A99 is in place to prevent overheating of the AOM driver. The BNC connector labeled FP IN is currently not in use. Previously, this input was used for plugging the Fabry Perot Etalon cavity, which was utilized as an interferometer for measuring relative changes of the laser beam wavelength. However, since the EXFO wavemeter provides more precise wavelength measurements, FP IN is no longer needed for CRDS experiments. The White Switch Box also has an amplifier and tracking module for a piezo transducer HPCh 150/15-8/3 produced by Piezomechanic GmbH, but this module is not currently in use. The piezo driver's function was to slightly adjust the length of the optical cavity by moving the first planoconcave mirror for better optical coupling. During experiments, the vibrations from the membrane pump serve this function. The diagram does not display the cryogenic and vacuum parts of the system for simplicity.

# 3   RESULTS AND DISCUSSION

## 3.1 Dissociative recombination of $N_2H^+$ ions in He

The recorded electrical signal from the photodiode reveals the alteration of energy carried by the laser beam which passed through the discharge and afterglow plasmas. The obtained time dependence reflects the absorbance of the investigated medium and can be transformed into the number densities of diazenylium in the determined quantum states of the ions. The calculations are performed using recently obtained transition dipole moments (more details in reference [79]). According to the assumption of the thermal population of states, the total number densities of $N_2H^+$ ions then can be evaluated from the partial number densities of the ions in particular quantum states.

The upper part of **Figure 10** displays time decays of the number densities of diazenylium ions. The various rotational states of the ground vibrational state of the investigated ions are marked with different colors. As can be seen from the middle part of the figure, there are no significant changes in the ratio of number densities of the particular rotational states of ions in the $N_2H^+$ plasma after switching off the discharge. On the other hand, we cannot state that the recombination rate coefficients are equal for those rotational states of investigated ions. It is also possible that at our experimental conditions rotational relaxation process could proceed much more rapidly than the recombination process. Fonseca dos Santos *et al.* [24] stated that vibrational or rotational excited states of $N_2H^+$ ions could have an enormous impact on the recombination process and its rate coefficient. However, the theoretical treatment in the paper [24] did not take into account such effects. In the present work, we show the results of the measurements

with the proper processing of thermal recombination rate coefficients. We carried out a due check that the ion temperatures such as vibrational, kinetic, and rotational are the same within the error of the measurement ($T_{vib} = T_{kin} = T_{rot}$).
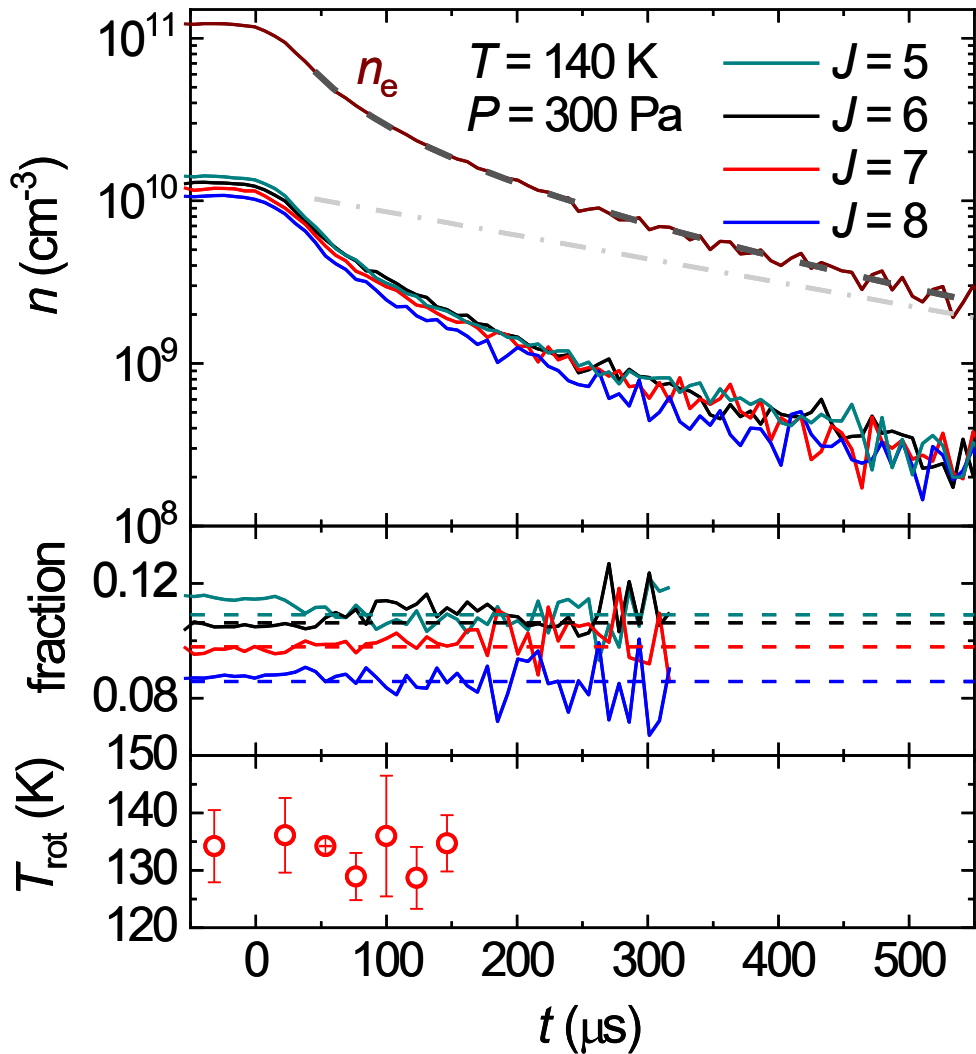


**Figure 10.** Top panel: the time decays of number densities of $N_2H^+$ ions in various rotational states of $N_2H^+$. All the transitions originated in the ground vibrational state of diazenylium. The data for discharge and afterglow plasmas are shown. Based on the assumption of a thermal population of states and plasma quasineutrality we calculate the electron number densities $n_e$. The zero time represents the start of the afterglow

processes. The fit to the data by means of Equation (8) is denoted by a dashed line. The fitted exponential losses of diazenylium ions are illustrated by a dot-dashed line. The conditions of the experiment were $T = 140$ K, $T_{kin} = 139 \pm 6$ K, $[He] = 1.5 \times 10^{17}$ cm$^{-3}$, $[Ar] = 2.5 \times 10^{14}$ cm$^{-3}$, $[H_2] = 5 \times 10^{14}$ cm$^{-3}$, and $[N_2] = 4 \times 10^{13}$ cm$^{-3}$. Middle panel: the fractional populations of the various rotational states of diazenylium evolving in plasma during the time of switching On (before 0 on X-axis) and switching Off the discharge. The values for the corresponding thermal populations at 140 K are shown by dashed lines. In the lower part of the figure: several values of rotational temperature of $N_2H^+$ ions were calculated based on the measurement of the relative population of rotational states in the ground vibrational state of ions. The time evolutions for the discharge and early afterglow are shown. Figure was adapted from reference [80].

According to our measurements, the neutral atoms of the carrier gas in the afterglow plasmas have the same temperature ($T_{He}$) as the kinetic temperatures of recombining ions. The effect of Doppler broadening of the absorption lines was utilized for the evaluation of the kinetic temperature of diazenylium. The significant pressure-induced broadening was detected under our experimental conditions and number densities of carrier gases, hence the absorption lines were fitted by using a Voigt profile. We obtain related pressure broadening coefficient $B_p$ from the dependence of the Lorentzian width of the fitted Voigt profile on buffer gas number density. In the **Table 2** are summarized results of measurement of the pressure broadening coefficients $B_p$ in the He carrier gas for the temperatures from 78 to 300 K. The P(6) overtone transition in the $(200) \leftarrow (000)$ vibrational band of $N_2H^+$ was used for $B_p$ evaluation. The value of the $B_p$ for other P branch transitions should be similar according to our assumption.

The measurement of relative populations of various rotational sates from the ground vibration state of the $N_2H^+$ ions give us enough data for precise evaluation of rotational temperature of the investigated ions.

**Table 2.** Coefficients of pressure broadening effect $B_p$ obtained for the P(6) overtone transition in the $(200) \leftarrow (000)$ vibrational band

| $T$ (K) | $B_P$ ($10^{-21}$ cm$^{-1}$cm$^3$) |
|---------|-------------------------------------|
| 78 | $6.2 \pm 0.5$ |
| 140 | $7.7 \pm 0.6$ |
| 200 | $8.9 \pm 0.3$ |
| 300 | $9.4 \pm 0.5$ |

According to the bottom part of **Figure 10**, the temperatures measured during discharge and early afterglow plasma time intervals are close to each other. The difference between the values is within experimental accuracy. The kinetic temperature $T_{kin}$ of the $N_2H^+$ ions and the wall temperature $T$ of fused silica discharge tube also almost coincide with the rotational temperature of diazenylium. **Figure 11** represents a relation between rotational temperature and kinetic temperature of the investigated ions measured in the discharge. As it is shown on the graph, the results of the evaluation for both temperatures of diazenylium for the whole examined temperature range are in good agreement.

The temperature measurements were not limited only by the determination of the rotational and kinetic temperature of the investigated ions. The vibration temperature evaluation was done as well. With the aim to obtain vibrational temperatures of the investigated diazenylium ions several number densities of various rotational states were taken. All these rotational states were situated in the ground vibrational state (000) and in the

first excited vibrational state $(01^10)$ of $N_2H^+$. As stated in reference [81], the distinction between the ground vibrational state and the first vibrationally excited state is approximately 690 cm$^{-1}$. Under the conditions of the thermal equilibrium at 300 K, only 10% of all diazenylium ions will be in the excited $(01^10)$ vibrational state.
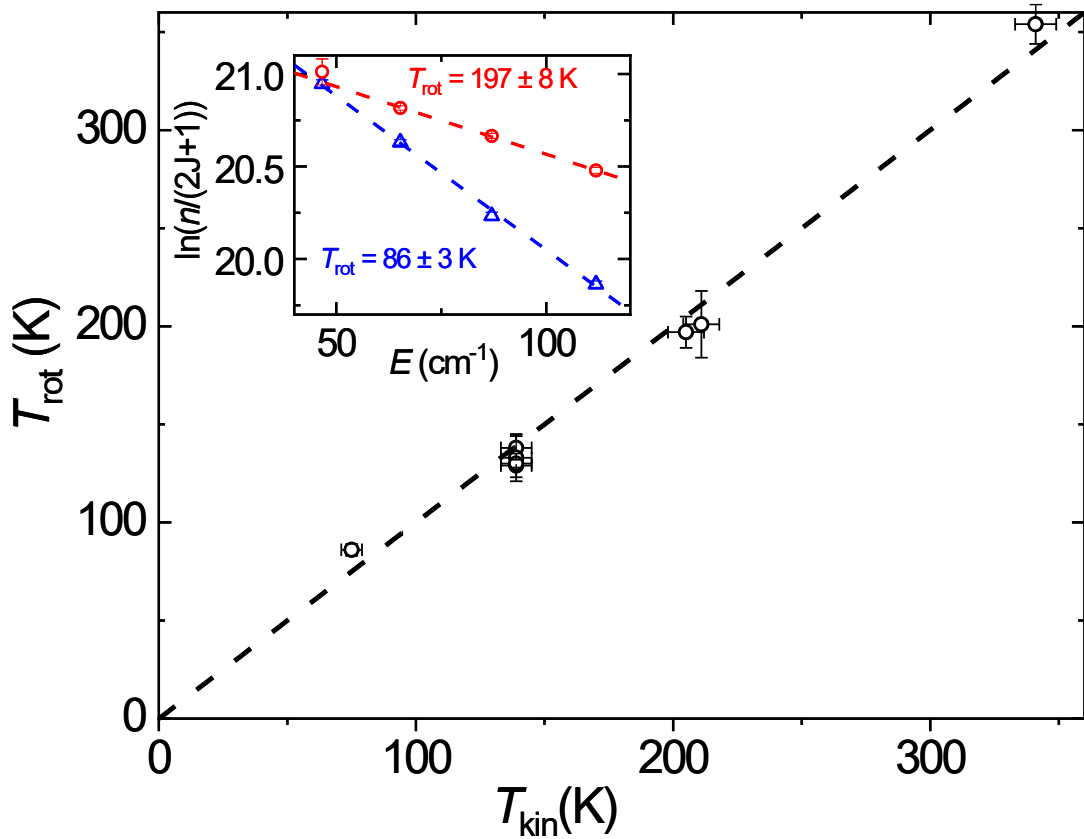


**Figure 11.** Relation between the rotational temperature and kinetic temperature of $N_2H^+$ ions obtained in the discharge. The measurements were carried out in the He buffered plasma. In order to evaluate the rotational temperatures measured at $T = 78$ K and $T = 200$ K the Boltzmann plot was used as it is shown in the inset. Figure was adapted from reference [80].

In **Figure 12** the decay for the number densities of diazenylium ions is traced in time for the ground (000) and excited $(01^10)$ state, respectively. The data which was measured during discharge and afterglow at the discharge

tube temperatures around $T = 300$ K are shown in the top part of **Figure 12**. An excellent agreement between relative population of the excited vibrational state $(01^{1}0)$ and the population corresponding to thermal equilibrium was observed. The data prove the statement for the discharge time as well as for the afterglow plasmas.
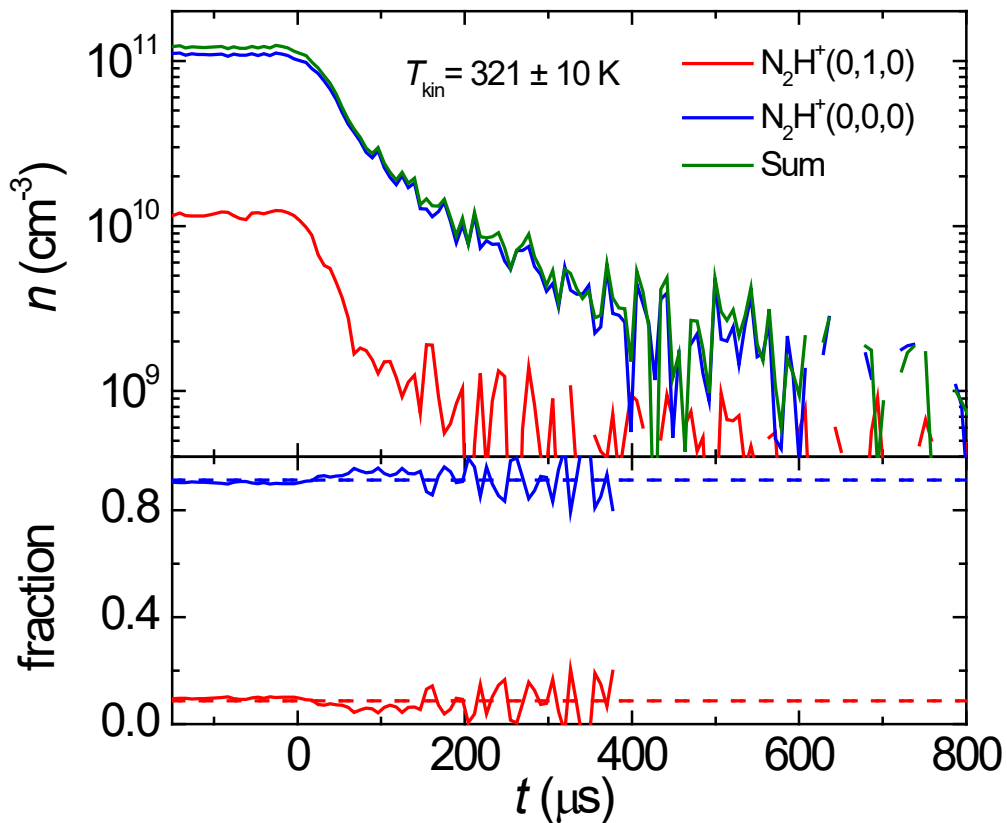


**Figure 12.** The decays in time of number densities of various vibrational states of $N_2H^+$. The data were measured for the ground vibrational state as well as for the first excited vibrational state. The bottom part of the figure represents relative fractions of the vibrational states. The corresponding fractions for the conditions of thermal equilibrium at 321 K are marked by the dashed lines. From the measured number densities of selected rotational states, the particular number densities of vibrational states were derived. Assuming of the equal rotational temperature in both

vibrational states, for the calculation were taken $J = 6$ rotational state of the ground vibrational state of $N_2H^+$ and $J = 9$ state of the excited vibrational state $(01^10)$ of the investigated ion. Figure was adapted from reference[80].

The plot in the **Figure 13** shows the dependence of ions vibrational temperature obtained during the discharge on the kinetic temperature of diazenylium. At lower temperatures, a substantial decrease of the number densities measured for the excited state was observed.
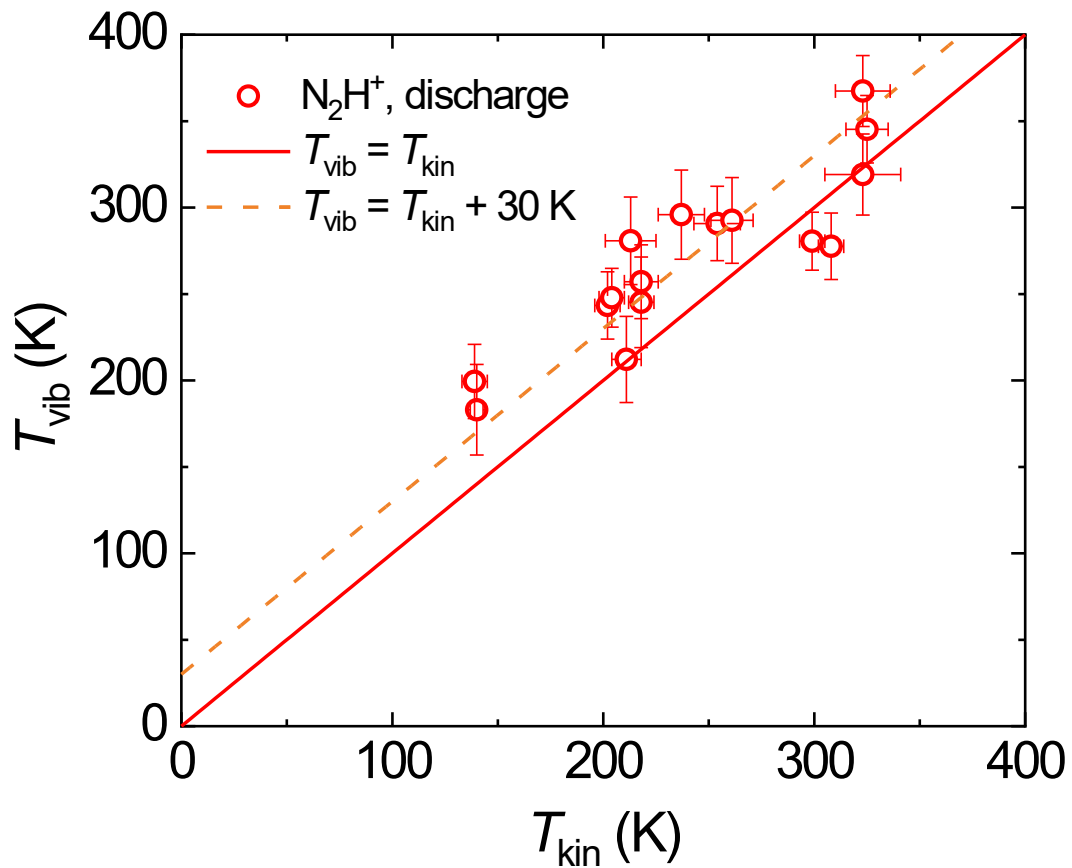


**Figure 13.** Relation between the vibrational $T_{vib}$ temperature and kinetic temperature $T_{kin}$ of $N_2H^+$ ions measured in discharge. For the evaluation of the kinetic temperature of the ions, we use Doppler broadening of the (P6) transition line in the $(200) \leftarrow (000)$ vibrational band of $N_2H^+$ ions.

We assumed that the rotational temperatures for the (010) and (000) states are equal to the kinetic temperature. The vibrational temperature of the $N_2H^+$ ions was then determined using the $R(9)^f$ line of the (210) ← (010) vibrational band and by utilizing the P(6) transition from the (210) ← (010) vibrational band of the diazenylium. Equality between two temperatures $T_{kin} = T_{vib}$ is shown by a full line on the graph and the dashed line represents $T_{kin} = T_{vib} + 30$ K. The statistical errors of the fits are indicated by error bars. Figure was adapted from reference [80].

The absorption lines corresponding to the $(21^10) - (01^10)$ vibrational band of diazenylium disappear at a temperature of about 80 K. During the discharge, the vibrational temperature is insignificantly higher than the related kinetic temperature. For our measurement, it was possible to take data by probing only the two lowest vibrational states of diazenylium.

Based on the above-described results of the measurements it is possible to state that the vibrational population, as well as rotational population of the diazenylium ions, are almost equal to the kinetic temperature of the recombining ions and that is quite close to the temperature $T$ of the discharge tube.

In discharge, the kinetic temperature $T_{kin}$ of the neutral species and the ions is considerably lower than the electron temperature $T_e$. The reason is the heating of electrons in plasma by means of the electric field in the microwave resonator during the discharge mode. The equilibrium between the temperatures is feasibly reached during the afterglow when the microwave power is turned off. The processes which can be responsible for the temperature equilibration are the collisions between electrons along with the collisions of neutral species with electrons in addition to ion-neutral collisions [36]. Another source of electron heating in afterglow can be the

presence of metastable helium. In the He-buffered plasmas it is very probable to find $2^1S$ and $2^3S$ states of helium which are long-lived. He atoms in these states can be observed even in the afterglow plasmas and due to inelastic collisions, these atoms are also responsible for the heating of the electrons. With the aim to investigate influence of metastable particles to our afterglow plasmas we made several experiments [71, 82, 83]. The process of removal of the highly excited species such as excited Ar atoms and He dimers was monitored in the plasmas after switching off the discharge. The removal rate was obtained as a function of $H_2$ and argon number densities. According to the results of those researches, under the present experimental conditions in particular Ar and $H_2$ number densities, after the discharge is switched off, the metastable He are removed from the afterglow plasma within the characteristic time of 30 μs or even faster.

Since we do not have any electron emission source (like filament etc.) in our system with microwave glow discharge the plasma can be considered as a quasineutral one. According to the assumption that we have $N_2H^+$ dominant plasma the decay in time of the number density of diazenylium $n_{N2H}$ in the afterglow plasma can be describe by equation

$$\frac{dn_{N2H}}{dt} = -\alpha_{eff}n_{N2H}n_e - k_R n_{N2H}[R] - \frac{n_{N2H}}{\tau_D}$$
$$= -\alpha_{eff}n_{N2H}^2 - \frac{n_{N2H}}{\tau}. \tag{6}$$

In the formula (6), $\alpha_{eff}$ is the effective recombination rate coefficient, $n_e$ denotes the electron number density, $k_R$ represents the rate coefficient for reaction of diazenylium with the admixtures (e.g., $NH_3$) of number density [R]. The time constant of charged particle losses due to ambipolar diffusion is labelled by $\tau_D$. Exponential losses of the charged species have the time constant $\tau$

$$\frac{1}{\tau} = \frac{1}{\tau_D} + \frac{1}{\tau_R} , \tag{7}$$

and here $1/\tau_R = k_R[R]$.

The solution of equation (6) can be expressed by using analytical formula:

$$n_{N2H} = \frac{1}{\alpha_{eff}\tau \left( e^{\frac{t-t_0}{\tau}} - 1 \right) + \frac{1}{n_0} e^{\frac{t-t_0}{\tau}}} , \tag{8}$$

and here $n_0$ denotes the number density of diazenylium at time $t = t_0$.

In this case label "eff" – "effective" means that we take in to account the possibility of existence of a dependence of recombination rate coefficient $\alpha_{eff}$ on the number densities of the reactants or carrier gas. For instance, the diazenylium ions can take part in both – two body and three body dissociative recombination at high number densities of carrier gas ($H_2$ or He in our experiments). The effective recombination rate coefficient for $N_2H^+$ can be written as

$$\alpha_{eff} = \alpha_{bin} + K_M[M] , \tag{9}$$

here $K_M$ is three body recombination rate coefficient and [M] represent number density of buffer gas (molecular hydrogen or helium). **Figure 14** shows the measured data for the relation between $\alpha_{eff}$ and $[H_2]$ or [He] which were produced at $T_{kin} = 350 \pm 15$ K and $T_{kin} = 325 \pm 10$ K, respectively. The number density of He was varied in the range of $(1 - 7) \times 10^{17}$ cm$^{-3}$. According to the results of our experiments, the effective recombination rate coefficient $\alpha_{eff}$ of $N_2H^+$ does not change significantly with He at the relatively stable temperature mentioned above. The increasing of [He] did not lead to

the increasing $\alpha_{\text{eff}}$ of $N_2H^+$ in our investigation. The values of effective recombination rate coefficient of diazenylium in the helium buffered plasma and molecular hydrogen buffered plasma are the same within the error of the measurement. The respective conditions of the presented measurements were $[H_2] = (5 - 8) \times 10^{16}$ cm$^{-3}$ with an admixture of $(3 - 10) \times 10^{14}$ cm$^{-3}$ of $N_2$ at $T_{\text{kin}} = 350 \pm 15$ K and for helium buffer gas at $T_{\text{kin}} = 325 \pm 10$ K.
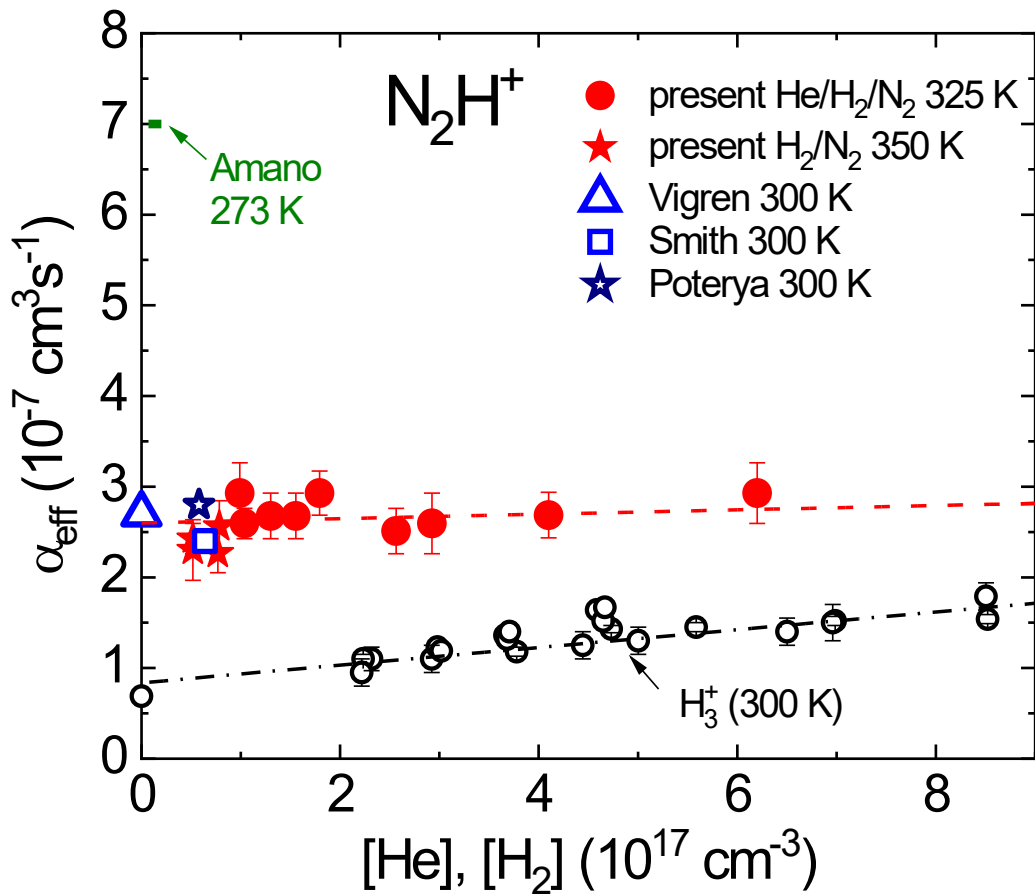


**Figure 14.** Relation between the measured effective recombination rate coefficient $\alpha_{\text{eff}}$ and number density of helium or molecular hydrogen buffer gas. The data for [He] were obtained at $T_{\text{kin}} = 325 \pm 10$ K with the admixture of $[N_2] = 3 \times 10^{14}$ cm$^{-3}$ and $[H_2] = 3 \times 10^{14}$ cm$^{-3}$. For the results obtained in the $[H_2]$ carrier gas, denoted by full stars, the conditions were $T_{\text{kin}} = 350 \pm 15$ K, $[N_2] = (3 - 10) \times 10^{14}$ cm$^{-3}$. The results obtained by other experimental

setups, ion storage ring [11] and FALP [17, 18], were measured at 300 K and are denoted by triangles, squares, and open stars, respectively. For the comparison, the results of $\alpha_{\text{eff}}$ for $H_3^+$ ions obtained in various experiments [35, 39, 84] are plotted as empty circles. All shown data for $H_3^+$ were measured at 300 K (for more details see reference [39]) and no distinction between various experimental researches on $H_3^+$ recombination is shown here. The linear fit to the $H_3^+$ data is displayed by dashed-dotted line and the linear fit to the $N_2H^+$ data is marked by dashed line. The value of $\alpha_{\text{eff}}$ for $N_2H^+$ obtained by Amano [21] at 273 K in hydrogen buffered plasma mixed with $N_2$ ([$H_2$] = $7 \times 10^{15} - 2 \times 10^{16}$ cm$^3$ s$^{-1}$) is marked by green arrow. Figure was adapted from reference [80].

Similar experimental researches were carried out by Amano [21] at 273 K on stationary afterglow experimental setup in the hydrogen buffered plasma at number densities of [$H_2$] = $(0.7 - 2.1) \times 10^{16}$ cm$^{-3}$, [$N_2$] = $(7 - 11) \times 10^{14}$ cm$^{-3}$. According to the Amano paper, the value of effective recombination rate coefficient of $N_2H^+$ at this temperature is $\alpha_{\text{eff}} = 7.0 \times 10^{-7}$ cm$^{-3}$. The value of $\alpha_{\text{eff}}$ for diazenylium in He or $H_2$ buffered plasmas is almost two time smaller based on our current experiments. On the contrary to Amano results, the data from ion storage ring [11] and flowing afterglow Langmuir probe [17, 18], which are in **Figure 14** denoted by triangles, squares, and open stars respectively, are in good agreement with the data from our SA-CRDS experiment. For the comparison, the results of $H_3^+$ measurement at 300 K are plotted on **Figure 14** too. Helium was used as a buffer gas for the evaluation of influence of the carrier gas on effective recombination rate coefficient of $H_3^+$ dominated plasma. More details are displayed in the figure 4 in reference [39]. As can be seen in the graph in **Figure 14**, the relation between $\alpha_{\text{eff}}$ of $H_3^+$ and number density of He makes

steeper line on the chart in comparison to the same dependence for $N_2H^+$ dominated plasma.

If the number density of $N_2$ surpasses certain value in investigated plasma, the helium assisted three body reaction between diazenylium and $N_2$ became possible with the production of $N_4H^+$ ions in plasma,

$$N_2H^+ + N_2 + He \xrightarrow{k_{N4H}} N_4H^+ + He . \tag{10}$$
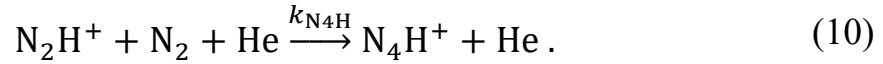
Experimental studies of the reaction (10) were done by Adams *et al.* [15] on the SIFT experimental setup at 80 K. The Adams research group obtained the three-body reaction rate coefficient $k_{N4H} = 2.8 \times 10^{-29}$ cm$^6$s$^{-1}$. We suppose that the inverse reaction to the equation (10) is negligible in our temperature range due to relatively high binding energy of $N_4H^+$ which is about 0.6 eV [85]. According to the formula (10), the number densities of $N_2$ and He should be limited in our present experiment. According to the findings mentioned in reference [15], at a temperature of 80 K, the reaction rate coefficient for the three-body association of $N_2H^+$ with $H_2$ in the presence of He does not exceed $5 \times 10^{-30}$ cm$^6$s$^{-1}$. The relation between the measured effective recombination rate coefficient of diazenylium and number density of diatomic nitrogen is displayed in the **Figure 15**. The data were acquired in helium buffered plasma with argon admixture at $T = 200$ K ([He] = (1 − 5) $\times 10^{17}$ cm$^{-3}$, [Ar] $\approx 5 \times 10^{14}$ cm$^{-3}$, [H$_2$] = (3 − 7) $\times 10^{14}$ cm$^{-3}$). The similar dependence of the measured effective recombination rate coefficient of diazenylium on number density of diatomic hydrogen is displayed in **Figure 16** in the inset.
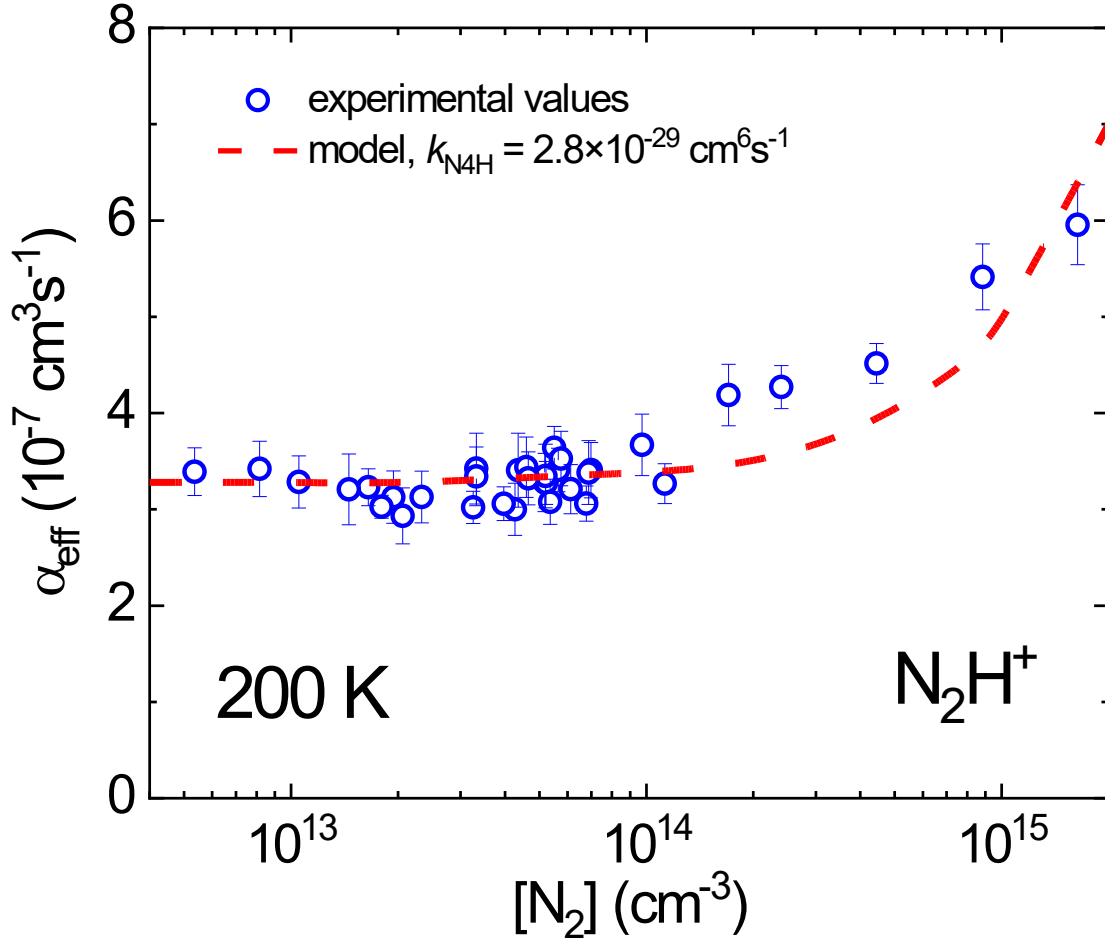
**Figure 15.** Relation between the measured effective recombination rate coefficient $\alpha_{eff}$ and number density of molecular [$N_2$]. The He-buffered plasma with Ar admixture had $T = 200 \pm 5$ K ([He] = $(1 - 5) \times 10^{17}$ cm$^{-3}$, [Ar] $\approx 5 \times 10^{14}$ cm$^{-3}$, [$H_2$] = $(3 - 7) \times 10^{14}$ cm$^{-3}$). The dashed line represent data fitted to the $N_2H^+$ time decays obtained from the model of chemical kinetics. The procedure of the fit for the experimental data and model data is the same. The parameters of the computational model were chosen the same as the conditions of the current experiment $T = 200$ K, [He] = $1.9 \times 10^{17}$ cm$^{-3}$, [Ar] = $5 \times 10^{14}$ cm$^{-3}$, [$H_2$] = $5 \times 10^{14}$ cm$^{-3}$ [80].
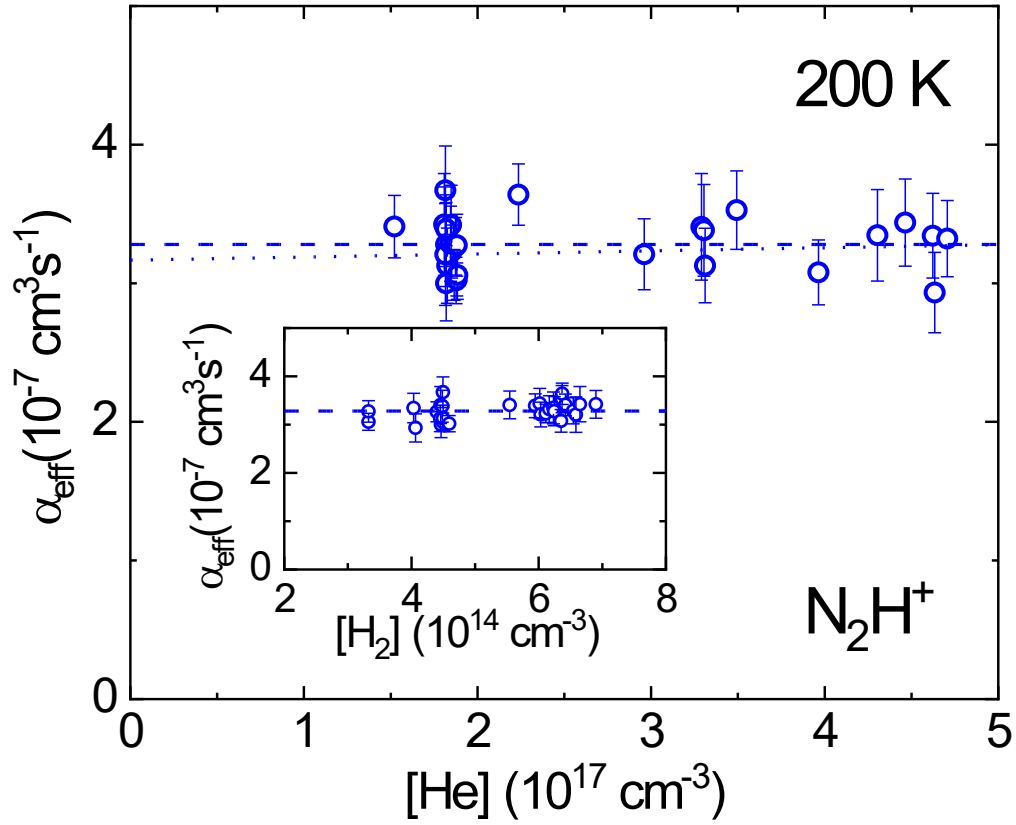
**Figure 16.** Relation between the measured effective recombination rate coefficient $\alpha_{eff}$ of diazenylium and number density of helium [He]. The number density of molecular nitrogen was $[N_2] < 1.0 \times 10^{14}$ cm$^{-3}$. The temperatures were $T = 200 \pm 5$ K, $T_{kin} = 217 \pm 9$ K, $T_{rot} = 197 \pm 8$ K and $T_{vib} = 230 \pm 40$ K. The number densities in a gas mixture were $[He] = (1 - 5) \times 10^{17}$ cm$^{-3}$, $[H_2] = (3 - 7) \times 10^{14}$ cm$^{-3}$, $[Ar] \approx 5 \times 10^{14}$ cm$^{-3}$. The linear fit to the measured data is marked by dotted line. The average value of all measured $\alpha_{eff}$ is shown by dashed line. Inset: relation between the measured effective recombination rate coefficient $\alpha_{eff}$ of $N_2H^+$ and number density of molecular hydrogen $[H_2]$. The main figure and the inset use the same dataset. The figure was adapted from reference [80].

Based on **Figure 15** and **Figure 16** it became obvious that for the low number density of molecular nitrogen $[N_2] < 10^{14}$ cm$^{-3}$, the effective

recombination rate coefficient does not depend on the number densities of particular gas [He], [H$_2$], [N$_2$] in a gas mixture. The rise of $\alpha_{\text{eff}}$ during the increase of dinitrogen number density was observed only for values [N$_2$] > $10^{14}$ cm$^{-3}$. These results from our SA-CRDS experimental setup (open circles) are in good qualitative agreement with our numerical model of the chemical kinetics (dashed line) as displayed in **Figure 15**. According to our computer model, under the conditions of a high number density of molecular nitrogen [N$_2$] the probability of the creation of N$_4$H$^+$ cluster ions in the three-body association reaction (10) is also high. The common evaluation of the recombination rate coefficient is based on the assumption that electron number density is equal to the diazenylium ions number density during the time decay in the afterglow plasma. The assumption is not valid anymore for the values [N$_2$] > $10^{14}$ cm$^{-3}$ and as a result, $\alpha_{\text{eff}}$ rises with the increasing of dinitrogen number density.

Similar measurements were also carried out at $T = 80$ K and $T = 140$ K. The model of chemical kinetics was also applied. It was important to check that there is no influence of ion clusters formation on the measured effective recombination rate coefficient. As it turned out, the producing of the ion clusters of N$_4$H$^+$ is proportional to the number densities of the gases [N$_2$] and [He]. Consequently, the portions of these two gases were limited in the gas mixture of our experiment, particularly at low-temperature conditions. Hence, this leads to the limitation of precision in the determination of the ternary recombination rate coefficient $K_{\text{He}}$. The obtained results were quite similar to those for the 200 K and 325 K temperature conditions. We have not observed a statistically significant dependence of $\alpha_{\text{eff}}$ on buffer gas number density [He] in the whole studied temperature range. Taking into account the cluster formation, only the upper estimate of the ternary recombination rate coefficient was obtained for data sets at 80 K and 140 K.

All our measured values of $K_{He}$ are summarized in the **Table 3**. For comparison, in the **Table 3** are also presented data for the $H_3^+$ ternary recombination rate coefficient which was obtained in He buffered plasma in our previous experiments [38, 40]. It is important to mention, that for the He positive ions value of $K_{He}$ was predicted to be $K_{He} \approx 10^{-27}$ cm$^6$ s$^{-1}$ at 300 K [26].

**Table 3.** The measured value of ternary recombination rate coefficient $K_{He}$ of $N_2H^+$ ions obtained in the present experiment compared to the $K_{He}$ of $H_3^+$ species measured in the He-buffered plasma [38, 40]. The $K_{He}$ of He$^+$ ions in helium plasma at 300 K is $K_{He\text{-Bates}} = 10^{-27}$ cm$^6$s$^{-1}$ according to the prediction by Bates and Khare [26].

| $T$ (K) | | $K_{He}(N_2H^+)$ | $K_{He}(H_3^+)$ |
|---|---|---|---|
| $N_2H^+$ | $H_3^+$ | $(10^{-25}$ cm$^6$ s$^{-1})$ | $(10^{-25}$ cm$^6$ s$^{-1})$ |
| 78 | 80 | $1.8^{+2.9}_{-1.8}$ | $1.5 \pm 0.2$ |
| 140 | 145 | $0.1^{+1.7}_{-0.1}$ | $1.4 \pm 0.3$ |
| 200 | 200 | $0.2^{+0.5}_{-0.2}$ | $2.3 \pm 0.9$ |
| 325 | 300 | $0.2^{+0.6}_{-0.2}$ | $2.7 \pm 0.5$ |

The recombination of diazenylium with electrons measured in the temperature range of 80 – 350 K is represented by binary recombination rate coefficients $\alpha_{bin}$ in the **Figure 17**. From the lower temperature limit of the measurements up to the top one, the results obtained in our studies are in good agreement with the experimental data obtained by Poteyra *et al.* [18] by means of the FALP setup. Our results obtained in the higher temperature region coincide well with the latest data measured by Vigren *et al.* [11] by means of an ion storage ring. A possible reason for the disagreement of our

result with the ion storage ring data at low temperatures could be the higher rotational temperatures of the investigated ions in the storage ring setup [20]. The next-generation apparatus for cryogenic ion storage rings studies CSR in Heidelberg [86] probably is able to overcome this problem [87]. The obtained binary recombination rate coefficient does not follow the temperature dependence ($T^{-0.5}$) which is typical for the plasma processes with the direct type of dissociative recombination of ions with the electrons. A good example of a direct type recombination process can be $O_2^+$ ions [28].
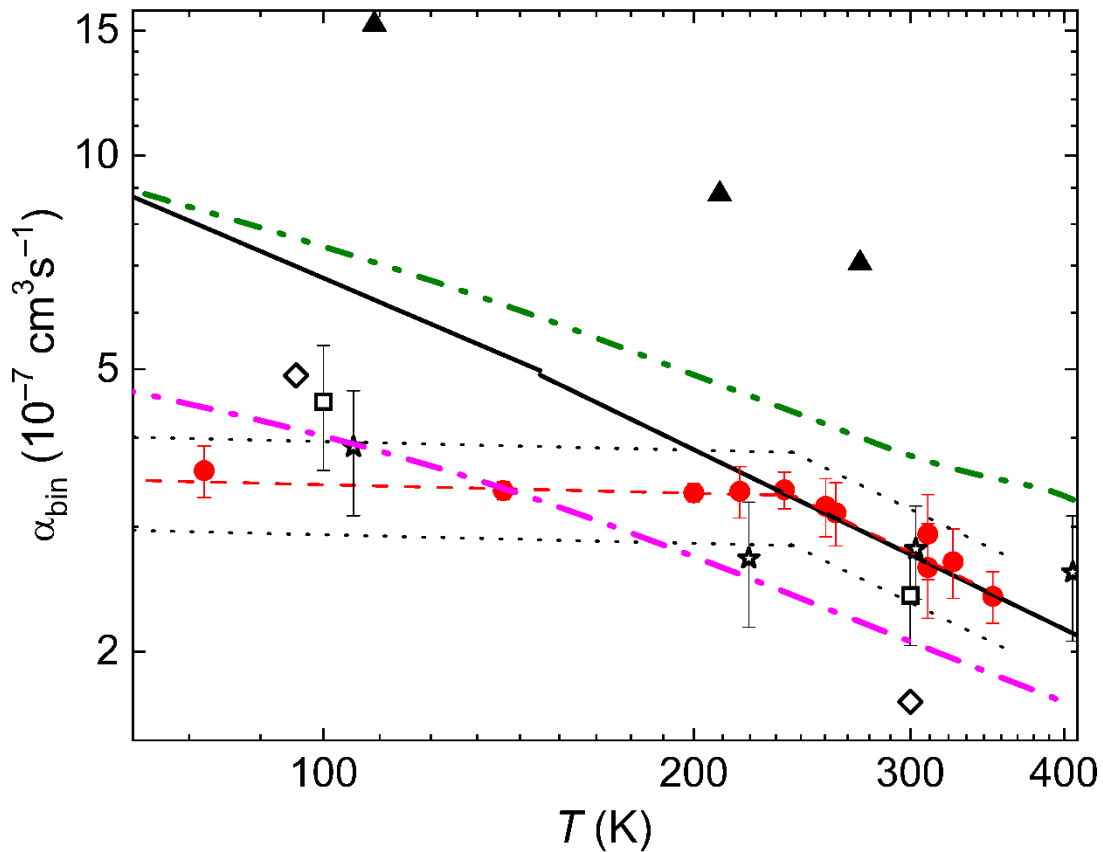


**Figure 17.** The comparison of measured results of the temperature dependence of $\alpha_{bin}$ of $N_2H^+$ obtained in our laboratory with the previous experiments. The full circles denote the values of the binary recombination rate coefficient ($\alpha_{bin}$) measured in $H_2$ buffered plasma at 350 K. The data points at other temperatures, marked also with full circles, were obtained in

He buffered plasma. The different FALP experiments are marked by rhomboids for [15], squares for [17] and stars for [18] measurements respectively. The triangles represent stationary afterglow experiment equipped with an absorption spectrometer [21]. The full line shows data from ion storage ring [11]. Merged beams experiments [12] marked by double-dot-dashed line. The dot-dashed line represents the theoretical calculations of the rate coefficient made by Fonseca dos Santos in recent study [25], based on the utilizing the cross section of indirect and direct recombination actions. The fits to the data are marked by dashed lines: $\alpha_{N2H+} = (3.29 \pm 0.04) \times 10^{-7}$ $(T/300 \text{ K})^{-(0.06 \pm 0.02)}$ cm$^3$s$^{-1}$ and for temperature range above 240 K $\alpha_{N2H+} = (2.81 \pm 0.04) \times 10^{-7}$ $(T/300 \text{ K})^{-(0.81 \pm 0.10)}$ cm$^3$s$^{-1}$ respectively. The deviation of 15% from the fitted value is marked by dotted lines. The estimated systematic error of the measurements reflects mainly the uncertainty in the effective discharge column length and in the calculated vibrational transition moments). Figure was adapted from reference [80].

For the high-temperature region of our studies, above 240 K, the measured value of binary recombination of diazenylium can be represented by a function $\alpha_{N2H+} = (2.81 \pm 0.04) \times 10^{-7}$ $(T/300 \text{ K})^{-(0.81 \pm 0.10)}$ cm$^3$s$^{-1}$. The lower temperature region of the measurement shows that $\alpha_{bin}$ of $N_2H^+$ almost does not change its value with the temperature alternation and can be described by an expression $\alpha_{N2H+} = (3.29 \pm 0.04) \times 10^{-7}$ $(T/300 \text{ K})^{-(0.06 \pm 0.02)}$ cm$^3$s$^{-1}$. The mentioned errors are statistical errors of the fit of the presented data. It is important to discuss the difference between the data of the present study and the results measured by Amano [21] by means of stationary afterglow infrared (IR) absorption spectroscopy utilizing hydrogen-buffered plasmas. The values of the recombination rate coefficient $\alpha_{eff}$ measured by us in hydrogen buffer gas at $\approx$ 350 K were almost the same as our results from measurements in helium buffer gas for the same

temperatures. According to Amano's paper [21] the value of the recombination rate coefficient for $H_3^+$ ions is extremely high in the $H_2$ buffered plasma. In our laboratory, we reproduced Amano's results for $H_3^+$ in the temperature range of 240 – 350 K using the same apparatus as in the present investigation [39, 40]. We explained, that the high value of the effective recombination rate coefficient for $H_3^+$ ions in hydrogen buffer gas is due to the fast $H_2$ assisted ternary recombination process [39, 40]. With the aim to calculate diazenylium ions number densities from measured data from absorption spectral lines, it is necessary to utilize transitional dipole moments which could be found in theoretical papers. The values of transition dipole moments, which Amano used, were calculated by Botschwina [88]. In the Botschwina paper, the transition dipole moments are higher than the most recent values calculated by Špirko [80] that we utilized in our study. By using the same transition dipole moments as Amano did, we obtain a 40 – 70% higher value of the recombination rate coefficient based on our measured data. The difference in the results can vary depending on the actual level of Botschwina's theory [88] on which Amano relied. This can largely explain the difference between our results for $\alpha_{eff}$ and Amano studies [21]. But different values of transition dipole moments are only one part of the explanation. Another one can be the cluster ions formation. With the decreasing of temperature, the formation of $N_4H^+$ cluster ions must be taken into account. The chemical kinetics of ions formation in low-temperature plasma at high number densities of $H_2$ was discussed in Reference [40]. As, similarly to us, Amano determined the recombination rate coefficients from measured ion number densities, the presence of other ions than $N_2H^+$ in afterglow could lead to a further apparent increase of the measured recombination rate coefficient.

For the low-temperature region, the data of present measurements are in good agreement with the recent quantum mechanical calculations made by Fonseca dos Santos [25]. The calculated result from Reference [25] is also two times lower than the results measured by CRYRING experimental setup [11]. At the same time, Fonseca dos Santos data at 300 K are around 40% lower than the results of the present experiment. Based on those differences, we can guess that there is a possible relation between the recombination rate coefficient and rotational excitation of the diazenylium positive ions which was not counted by the theory. A similar dependence was found by Novotny *et al.* [87] for HeH$^+$ ions. In his recent state selective research [87], the electron-ion recombination of HeH$^+$ ions was affected by the rotational excitation of investigated ions. The recombination rate coefficient of HeH$^+$ measured by Novotny *et al.* [87] is about order of magnitude higher for helium hydride ions in high rotational states than for the ions in rotational ground state $[\alpha_{HeH+}(J = 0, 100 \text{ K}) \approx 2 \times 10^{-9} \text{ cm}^3\text{s}^{-1}]$. The previous experiments on the ion storage ring show coefficient $\alpha_{HeH+}$ (100 K) $\approx$ $8 \times 10^{-8}$ cm$^3$s$^{-1}$ according to the measurements made by Strömholm *et al.* [89]. The real rotational excitation of HeH$^+$ ions in the Strömholm experiments could be higher and measured $\alpha_{HeH+}$ probably corresponded to the rotational population of helium hydride ions at 300 K. The relation between recombination rate coefficient and rotational population of states of diazenylium ions could be qualitatively described by the similar temperate dependence. It can explain the results which were obtained in the present experiments. The comparison of Vigren *et al.* [11] ion storage ring results with values measured in our laboratory gives excellent agreement of data of about 300 K. At this temperature, the rotational population of states of N$_2$H$^+$ is the same in both experiments and corresponds to 300 K. The situation undergoes a significant change around the temperature threshold of 80 K. The recombination rate coefficient of diazenylium ions with a rotational

population of states corresponding to 80 K, which was measured by our CRDS setup, is two times lower than the results obtained by ion storage ring apparatus for $N_2H^+$ ions with a 300 K rotational population of states.

### 3.1.1 Theoretical calculations by V. Špirko

As was already mentioned, for the calculation of $N_2H^+$ ion number densities the electric dipole moments were utilized. Those dipole moments, in turn, were determined by using electric dipole surfaces and the *ab initio* potential energy based on data from Reference [79]. The Suttcliffe-Tennyson Hamiltonian [90] for triatomic molecules was applied. Our reliable predictions guarantee good agreement between calculated values and their measured equivalents that are available for low-lying vibrational states, [91, 92], as can be seen from the results of our experiments. **Table 4** shows all vibrational transitional dipole moments $M$ of diazenylium, which were obtained during the present study. The vibrational transition moments which were calculated in the present experimental research turned out about 20% lower than the corresponding values in the Botschwina paper [88] utilized to obtain ion number densities in the absorption spectroscopy study by Amano [21]. The evaluated ion number density of diazenylium is proportional to the inverse of $M^2$. Therefore, Amano's [21] recombination rate coefficients are overestimated and thus the difference between his and our data can reach up to 40%.

**Table 4.** The comparison of the vibrational transition moments, marked as $M_{present} = |<v_1''v_2''v_3''|\mu_z|v_1'v_2'v_3'>|$, of diazenylium (in Debye) calculated in the present experimental research for two isotopes of nitrogen and of the corresponding values from Botschwina paper [88], marked as $M_{Botschwina}$, CEPA-1(ED) level of theory. The numbers in parentheses in the fourth

column are the IR intensities of absorption in $cm^2$ $mol^{-1}$ from Reference [88]. $M_{Botschwina}$ were calculated from these values using equation (2) in the paper [93]. Prime and double prime denote upper and lower states, respectively.

| Transition | $M_{present}$ | | $M_{Botschwina}$ |
|:---:|:---:|:---:|:---:|
| $v_1''v_2''v_3'' \leftrightarrow v_1'v_2'v_3'$ | $(^{14}N_2H^+)$ | $(^{15}N_2H^+)$ | $(^{14}N_2H^+)$ |
| $0\ 0\ 0 \leftrightarrow 0\ 0\ 0$ | $3.4906^a$ | 3.4910 | |
| $0\ 0\ 0 \leftrightarrow 2\ 0\ 0$ | 0.0153 | 0.0157 | 0.0191 (91.2) |
| $1\ 0\ 0 \leftrightarrow 3\ 0\ 0$ | 0.0256 | 0.0266 | |
| $0\ 0\ 0 \leftrightarrow 1\ 0\ 0$ | $0.2432^b$ | 0.2430 | 0.284 (20257) |
| $0\ 1^1\ 0 \leftrightarrow 2\ 1^1\ 0$ | 0.0153 | 0.0157 | |
| $0\ 2^0\ 0 \leftrightarrow 2\ 2^0\ 0$ | 0.0153 | 0.0154 | |
| $0\ 1^1\ 0 \leftrightarrow 1\ 1^1\ 0$ | 0.2430 | 0.2428 | |
| $0\ 0\ 1 \leftrightarrow 2\ 0\ 1$ | 0.0147 | 0.0152 | |
| $0\ 2^2\ 0 \leftrightarrow 2\ 2^2\ 0$ | 0.0154 | 0.0154 | |

[a] Experimental value from Reference [91]: $3.4 \pm 0.2$ D.
[b] Experimental value from Reference [92]: $0.23 \pm 0.02$ D.

### 3.1.2 Discussion of errors and their sources

The errors mentioned in the present study are statistical errors. The systematic errors of measured data in our experiments are mainly caused by difficulties with the estimation of discharge column length. The impact of this uncertainty on the systematic error of the recombination rate coefficient evaluation was evaluated as 10%. Another contribution to the systematic errors of our measurements makes the uncertainty of the utilized values of the vibrational transition moments. The comparison of the experimentally obtained vibrational transition moments in previous studies [91] and [92]

with our calculated values reveals systematic error not higher than 5% for the estimation of recombination rate coefficient and a maximum 15% can be the overall systematic error in this case.

### 3.1.3 Model of chemical kinetics

With the purpose to investigate the evolution of chemical processes in the afterglow plasma the model of chemical kinetics was developed and utilized for calculations in the frame of present experimental conditions. The number densities of each species, have been calculated via a system of differential rate equations. The assembly of differential equations consists of the set of corresponding chemical equations which include two body and three body interactions among all the investigated species, such as neutral molecules and atoms, electrons, atomic and molecular ions. The chemical evolution model contains also an ambipolar diffusion of charged particles as a first-order differential equation. Then, the multistep solver for stiff equations, which is embedded in the Isoda [94] routine, has been applied in order to find the solution of differential equations for chemical kinetics in our experimental stationary afterglow apparatus. The **Table 5** provides a summary of the reactions which are principal in the formation and destruction of diazenylium ions in a gas mixture of He / $N_2$ / $H_2$/ Ar. Based on the discussion in a paper [61], we assumed that, at the first stage of the afterglow, the number density of helium atoms in metastable states $He^m$ ($2^3S$ and $2^1S$) is the same or not higher than the number density of electrons. The values of reaction rate coefficients, indicated in the **Table 5**, are mostly calculated for 300 K or, in marked cases, at other temperature conditions. However, for some associative chemical reactions (like R20 and R14) in the He buffer gas, we used the rate coefficients measured in $H_2$ buffered plasmas. The values for R14 and R20 are taken from Reference [40].

**Table 5.** The list of the crucial chemical reactions for the formation of $N_2H^+$ ions which were considered in our model of chemical kinetics. The value of the recombination rate coefficient is corresponding to measurement conditions at 300 K excluding the reaction R26. The characteristic reaction times $\tau_{reaction}$ were calculated for $[He] = 2 \times 10^{17}$ cm$^{-3}$, $[Ar] = 5 \times 10^{14}$ cm$^{-3}$, $[H_2] = 5 \times 10^{14}$ cm$^{-3}$, $[N_2] = 5 \times 10^{13}$ cm$^{-3}$, $[NH_3] = 5 \times 10^{11}$ cm$^{-3}$, $[N] = 5 \times 10^{11}$ cm$^{-3}$, $[H] = 5 \times 10^{11}$ cm$^{-3}$, $n_e = 1 \times 10^{11}$ cm$^{-3}$ from the appropriate rate coefficient $k$ and reactant number densities [R] as $\tau_{reaction} = 1/(k[R])$ for two body reactions and similarly for the three body reactions. The values of the reaction rate coefficient for $H_2^+$ ions are represented for vibrational excitation v $\leq$ 1. The reaction R26 shows the reaction rate coefficient measured at 80 K.

| № | Reaction | Rate coefficient (cm$^3$s$^{-1}$, cm$^6$s$^{-1}$) | $\tau_{reaction}$ (µs) | References |
|---|---|---|---|---|
| R1 | $He^m + H_2 \rightarrow H_2^+ + He + e^-$ 90% | $3.2 \times 10^{-11}$ | 62.5 | [95] |
|  | $\rightarrow HeH^+ + H + e^-$ 10% |  |  | [96] |
| R2 | $He^m + Ar \rightarrow Ar^+ + He + e^-$ | $7 \times 10^{-11}$ | 28.6 | [97] |
| R3 | $He^+ + He + He \rightarrow He_2^+ + He$ | $1 \times 10^{-31}$ | 250.0 | [98] |
| R4 | $He^+ + N_2 \rightarrow N^+ + N + He$ 60% | $1.6 \times 10^{-9}$ | 13.0 | [99] |
|  | $\rightarrow N_2^+ + He$ 40% |  |  |  |
| R5 | $HeH^+ + H_2 \rightarrow H_3^+ + He$ | $1.5 \times 10^{-9}$ | 1.3 | [100] |
| R6 | $HeH^+ + N_2 \rightarrow N_2H^+ + He$ | $1.70 \times 10^{-9}$ | 11.8 | [101] |
| R7 | $He_2^+ + Ar \rightarrow Ar^+ + He + He$ | $2 \times 10^{-10}$ | 10.0 | [98] |
| R8 | $He_2^+ + N_2 \rightarrow N_2^+ + He + He$ | $1.12 \times 10^{-9}$ | 17.9 | [102] |
| R9 | $Ar^+ + H_2 \rightarrow ArH^+ + H$ 85% | $8.6 \times 10^{-10}$ | 2.7 | [103] |
|  | $\rightarrow H_2^+ + Ar$ 15% |  |  |  |
| R10 | $Ar^+ + N_2 \rightarrow N_2^+ + Ar$ | $1.0 \times 10^{-11}$ | 2000 | [104] |

| R11 | $ArH^+ + H_2 \rightarrow H_3^+ + Ar$ | $1.5 \times 10^{-9}$ | 1.3 | [105] |
|---|---|---|---|---|
| R12 | $ArH^+ + N_2 \rightarrow N_2H^+ + Ar$ | $8.0 \times 10^{-10}$ | 25 | [105] |
| R13 | $H^+ + He + He \rightarrow HeH^+ + He$ | $9 \times 10^{-32}$ | 277.8 | [106] |
| R14 | $H^+ + H_2 + He \rightarrow H_3^+ + He$ | $3 \times 10^{-29}$ | 333.3 | [40] |
| R15 | $H_2^+ + Ar \rightarrow ArH^+ + H$ | $2.3 \times 10^{-9}$ | 0.9 | [107] |
| R16 | $H_2^+ + H_2 \rightarrow H_3^+ + H$ | $2 \times 10^{-9}$ | 1.0 | [107] |
| R17 | $H_2^+ + N_2 \rightarrow N_2H^+ + H$ | $2 \times 10^{-9}$ | 10.0 | [108] |
| R18 | $H_3^+ + N_2 \rightarrow N_2H^+ + H_2$ | $1.8 \times 10^{-9}$ | 11.1 | [101] |
| R19 | $H_3^+ + e^- \rightarrow products$ | $1.10 \times 10^{-7}$ | 90.9 | [40] [109] |
| R20 | $H_3^+ + H_2 + He \rightarrow H_5^+ + He$ | $2 \times 10^{-30}$ | 5000.0 | [40] |
| R21 | $H_3^+ + NH_3 \rightarrow NH_4^+ + H_2$ | $4.39 \times 10^{-9}$ | 455.6 | [110] |
| R22 | $N^+ + H_2 \rightarrow NH^+ + H$ | $3.7 \times 10^{-10}$ | 4.0 | [111] [112] |
| R23 | $N_2^+ + H_2 \rightarrow N_2H^+ + H$ | $2 \times 10^{-9}$ | 1.0 | [113] |
| R24 | $N_2H^+ + e^- \rightarrow products$ | $2.80 \times 10^{-7}$ | 35.6 | Present |
| R25 | $N_2H^+ + NH_3 \rightarrow NH_4^+ + N_2$ | $2.30 \times 10^{-9}$ | 869.6 | [69] |
| R26 | $N_2H^+ + N_2 + He \rightarrow N_4H^+ + He$ | $2.80 \times 10^{-29}$ | 3571.4 | [15] |
| R27 | $NH_4^+ + e^- \rightarrow products$ | $1.4 \times 10^{-6}$ | 7.1 | [114] |
| R28 | $N_4H^+ + e^- \rightarrow products$ | $2 \times 10^{-7}$ | 50.0 | Estimate |

The comparison between the calculated and measured characteristics is shown in **Figure 18** as the time-resolved evolution of the number density of diazenylium ions in the afterglow plasma at 140 K. Since the actual composition of ion mixture in the plasma at the end of the discharge is not well known, the initial conditions for the beginning of the afterglow plasma

were varied. In particular, the different initial ion number densities for the early afterglow period were used. The developed model of chemical kinetics was applied to afterglow plasma and shows that $N_2H^+$ ions are dominant species in 200 microseconds after the discharge was switched off.
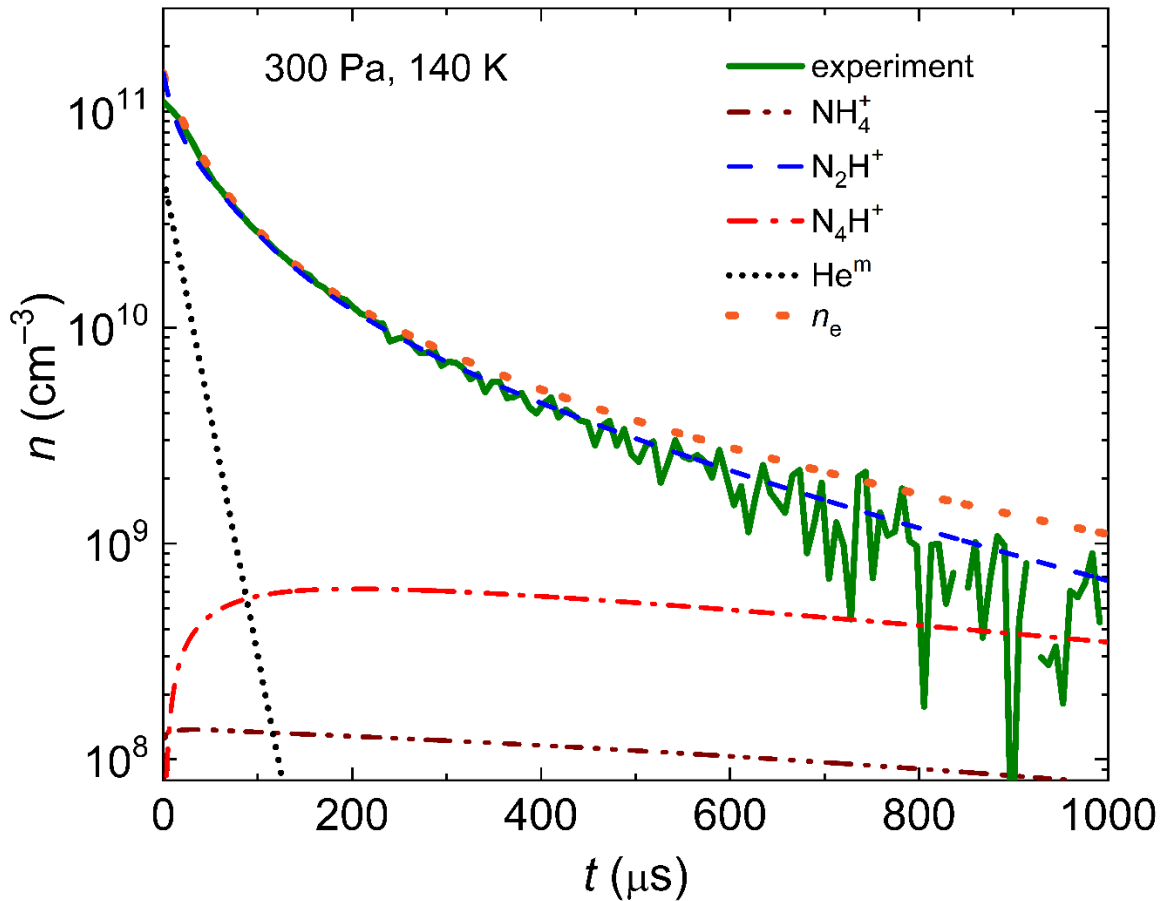


**Figure 18.** The comparison of results of the time evolution of $N_2H^+$ ion number density measured in our laboratory with the calculated values from our model of chemical kinetics. The data were obtained at $T = 140$ K, the number densities of gases were [He] $= 1.5 \times 10^{17}$ cm$^{-3}$, [H$_2$] $= 5 \times 10^{14}$ cm$^{-3}$, [Ar] $= 2.5 \times 10^{14}$ cm$^{-3}$, [N$_2$] $= 4 \times 10^{13}$ cm$^{-3}$ (same as in **Figure 10**) and [NH$_3$] $= 5 \times 10^{11}$ cm$^{-3}$, [He$^m$] $(t = 0) = 1/3\ n_e\ (t = 0)$. The figure was adapted from reference [80].

However, the results of the model are changed significantly if plasma contains a sufficient amount, tens of percent, of $N^+$ ionic species. The atomic nitrogen ions react rapidly with molecular hydrogen which leads to the formation of $NH^+$ ions due to reaction R22. In the next stage, the collision of $NH^+$ with molecular hydrogen initiates the production of $NH_4^+$ through subsequent reactions with hydrogen involving intermediate ions $NH_2^+$ and $NH_3^+$. Detailed information about this reaction chain is available in Reference [115]. In the present study, the aim was to find the possible correlation between carrier gas number densities and the effective recombination rate coefficient of $N_2H^+$ which was measured in afterglow plasma (**Figures 15** and **16**). According to results obtained in the present experiments, the effective recombination rate coefficient of diazenylium does not change significantly when the number densities of initial reactants are varied by almost an order of magnitude and does not have a observable dependence on the buffer gas number density. Therefore, we assume that the afterglow plasma in our apparatus contains less than 10% of atomic nitrogen ions in the first microsecond of afterglow, which definitely leads to the formation of $N_2H^+$ dominant plasma instead of faster recombining $NH_4^+$ dominant plasmas.

## 3.2 Dissociative recombination of $H_3^+$ ions in He or Ne

The investigation focused on the dissociative recombination of $H_3^+$ ions in their lowest rotational state, specifically targeting second overtone transitions: $3\nu_2^1(2,1) \leftarrow 0\nu_2^0(1,1)$ for the para nuclear spin state symmetry, and $3\nu_2^1(2,0) \leftarrow 0\nu_2^0(1,0)$ for the ortho nuclear spin state symmetry. The quantum numbers $J$ and $G$ are shown in parentheses, where $G$ can be found as $G = |K - l|$. Here $K$ represents the quantum number for the projection of the rotational angular momentum $J$ on the body-frame symmetry axis and $l$ is the quantum number for vibrational angular momentum. More information about symmetry and notation can be found in Reference [116]. Based on Einstein coefficients and energies from the Reference [117] and measured values of absorbance obtained in the present study, the relevant rotational state number densities were determined. According to the results of the previous measurements [36, 118] on the similar or same experimental apparatus and relevant conditions, it is safe to assume that at the given temperature $H_3^+$ ions have rotational levels populated pursuant to thermal equilibrium. Consequently, the ion number density of $H_3^+$ considered in the present study was obtained according to the assumption of the thermal population of states. We decided to use the strongest transition $3\nu_2^1(2,0) \leftarrow 0\nu_2^0(1,0)$ which was available for measured values of number density from the ortho nuclear spin state $H_3^+(1,0)$. Only with the purpose of confirmation of thermal ratio between para and ortho states, the transition $3\nu_2^1(2,1) \leftarrow 0\nu_2^0(1,1)$ was utilized.

The probability of the formation of $H_3^+$ ions during the afterglow processes in plasma is not equal to zero. However, for the determination of the time evolution of number densities those ions an assumption was applied

that there is no $H_3^+$ ions formation after switching off the discharge. As a result, time evolution of $H_3^+$ ions can be described by the equation:

$$\frac{dn_{H_3}}{dt} = -\alpha_{eff}\, n_{H_3} n_e - \frac{n_{H_3}}{\tau}. \tag{11}$$

Here, the ion number density of the $H_3^+$ ions marked as $n_{H_3}$ and electron number density showed as $n_e$, respectively. The effective recombination rate coefficient of $H_3^+$ ions is marked as $\alpha_{eff}$, where the subscript "eff" means the possible influence [34] of the number density of buffer gas on the measured value of the recombination rate:

$$\alpha_{eff} = \alpha_0 + K_M[M]. \tag{12}$$

Here, $\alpha_0$ denotes the binary recombination rate coefficient relevant for different low-density media which could be found, for example, in interstellar gas clouds. The ternary recombination rate coefficient is marked as $K_M$, where M is the particular third body species with the number density [M]. The $\tau$ from Equation (11) denotes the time constant that represents losses caused by neutral-ion reactions and by the ambipolar diffusion:

$$\frac{1}{\tau} = \frac{1}{\tau_D} + \frac{1}{\tau_R}. \tag{13}$$

Here, $\tau_D$ denotes time constant which represents losses of charged species due to the ambipolar diffusion processes. The losses caused by the collisions of $H_3^+$ ions with the neutral species during ion-molecule reactions are shown by symbol $\tau_R$. In the case of our experimental conditions such as temperature, pressure, number densities of reactant, the losses can mainly be results of the formation of $H_5^+$ ions which recombine relatively fast. The emergence of $H_5^+$ ions is the outcome of the reactions of three body

association, for instance, $H_3^+$ ions collisions with the neutral $H_2$ in the ambient of neon or helium as a buffer gas:

$$H_3^+ + H_2 + He \rightarrow H_5^+ + He \,, \tag{14}$$

$$H_3^+ + H_2 + Ne \rightarrow H_5^+ + Ne \,. \tag{15}$$

There are two main processes which are responsible for the time evolution of number density of electrons in $H_3^+$ dominated afterglow plasmas. Those processes are ambipolar diffusion and electron-ion recombination:

$$\frac{dn_e}{dt} = -\alpha_{eff} n_{H_3} n_e - n_e \sum_i \alpha_i n_i - \frac{n_e}{\tau_D} \,. \tag{16}$$

Here, the ion number density and the recombination rate coefficient of other ions (not $H_3^+$) in $H_3^+$-dominated afterglow plasmas are marked as $n_i$ and $\alpha_i$ respectively. The model of chemical kinetics for He-buffered afterglow plasma in the Reference [40] predicts that $H_5^+$ ions can be the main reason for changes in electron number density at present experimental conditions.

The rate coefficient for the recombination of investigated ion species can be determined by means of acquiring experimental data on the time evolution of $H_3^+$ number density and of the number density of electrons. Then the set of the corresponding differential equations must be numerically solved. The new approach allows us to carry out the correct interpretation of the data even from the measurements in the afterglow plasmas where the dominant ionic specie is not the $H_3^+$ ion. However, it is important to notice that an assumption about other possible reactions and processes in afterglow plasma is needed to be taken into account for the utilization of a new approach. The evolution of ion number densities can be easily determined in a helium-buffered plasma containing a mixture of hydrogen and argon,

thanks to the customizable conditions that can be set. Only ions such as $H_5^+$ and $H_3^+$ are predominantly present in this case [40]. Consequently, the set of the corresponding differential equations then will consist of only Equation (16) for electrons, number density of $H_3^+$ will be described by Equations (11) and $H_5^+$ number density evolution will be, respectively, described by Equation:

$$\frac{dn_{H_5}}{dt} = -\alpha_5\, n_{H_5} n_e - \frac{n_{H_5}}{\tau_{DH5}} + \frac{n_{H_3}}{\tau_R}. \tag{17}$$

Here, the number density of $H_5^+$ ions is marked as $n_{H5}$ and the corresponding recombination rate coefficient of these ions is shown as $\alpha_5$. The time constant $\tau_R$ can be found as $\tau_R = 1/(k_3[H_2][He])$ and $k_3$ here denotes the reaction rate coefficient for the reaction of tree-body association (14).

For the cases where processes of chemical kinetics are not known in sufficient detail for the description of all possible reactions, like in the situation of plasmas with Ne buffer gas mixture, the direct integration of Equation (11) is the solution which produces the values of number density of $H_3^+$ in the corresponding time $t_i$:

$$n_{H_3}(t_i) = n_{H_3}(t_0)e^{-\alpha_{eff}X(t_i)-\frac{1}{\tau}Y(t_i)}. \tag{18}$$

Here the initial number density of $H_3^+$ ions is marked as $n_{H_3}(t_0)$,

$$X(t_i) = \int_{t_0}^{t_i} n_e(t)dt. \tag{19}$$

and

$$Y(t_\text{i}) = t_\text{i} - t_0. \tag{20}$$

All the values of variables $Y(t_\text{i})$, $X(t_\text{i})$ and $n_{\text{H}_3}(t_\text{i})$ can either be measured or calculated based on the measured data. Therefore, the plasma characteristics such as $\tau$, $n_{\text{H}_3}(t_0)$ and $\alpha_\text{eff}$ can be easily found when solving equation (18) in the least square sense.

### 3.2.1 H₃⁺ recombination in ambient helium gas

With the help of the model of chemical kinetics described in Reference [40], the conditions for the present experiment were chosen with the intention to get helium-buffered plasmas where $\text{H}_3^+$ ions are dominant in the early afterglow stage. Thereby the value of the ion number density of $\text{H}_3^+$ ions, measured by means of a cavity ring-down spectrometer, should be equal to the value of the electron number density, obtained through the shift of the resonant frequency of the microwave resonator. The coincidence of those two measured plasma parameters at the beginning of the plasma decay evolution must be in the range of uncertainty of the measurement.

The time evolution of the number densities of $\text{H}_3^+$ ions and of electrons measured in the He-buffered plasma during the afterglow at $T = 200$ K is represented in **Figure 19**. The temperature $T$ hereinafter denotes measured temperature data from the sensor H which is situated on the holder of the sapphire discharge tube as can be seen in **Figure 4**. According to the Reference [71], the temperature measured by sensor H equals the kinetic temperature of $\text{H}_3^+$ ions, which was evaluated using the Doppler broadening effect based on the measured data of absorption spectral lines.
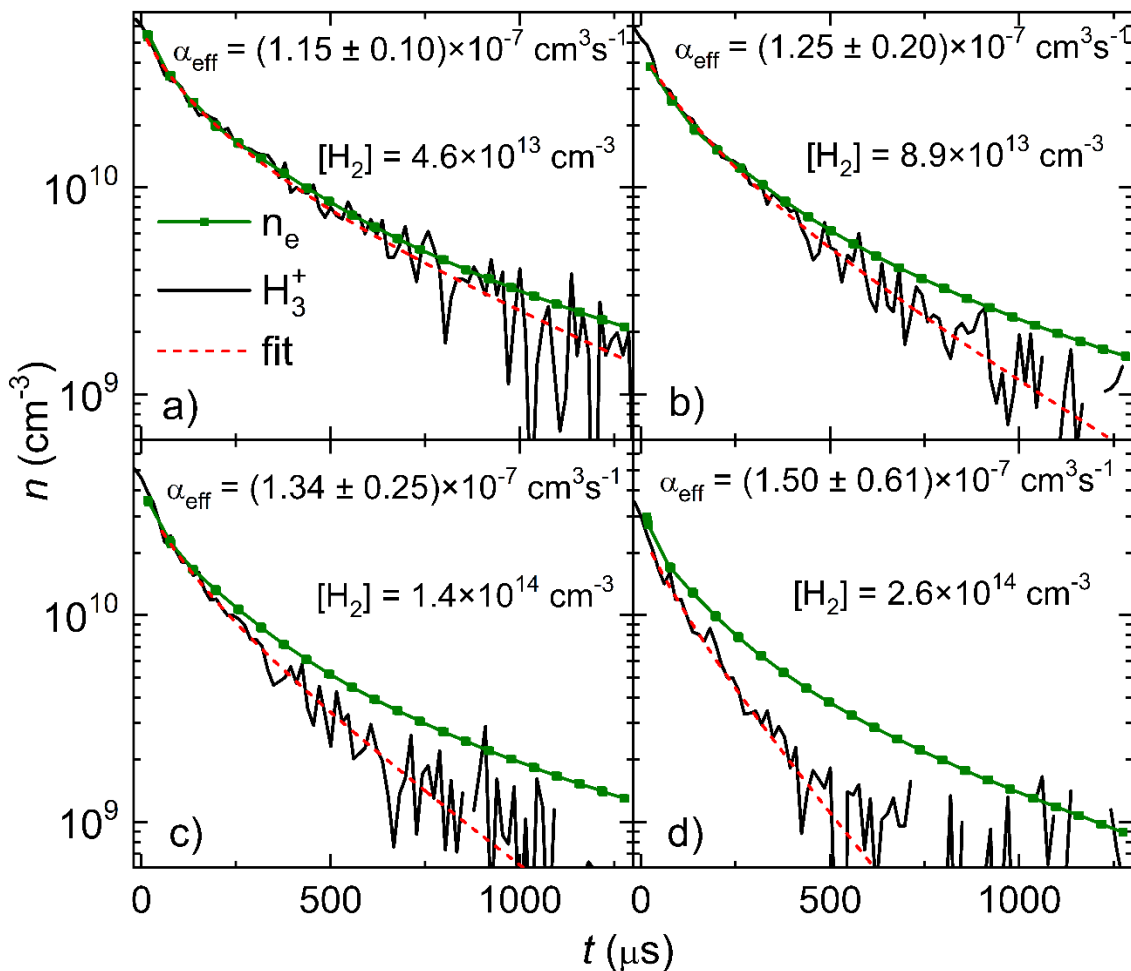
**Figure 19.** The dependence of the time evolution of number densities of $H_3^+$ ions and of electrons, which are marked by full lines and full squares respectively, on the various number densities of $H_2$. The measurements were carried out in the afterglow plasma using helium as a carrier gas. The fit to the data was applied by means of Equation (18) and is shown as a dashed line. The details of the fitting procedure are described in the text. The effective recombination rate coefficients for each experiment are denoted in the corresponding panels. The errors of the recombination rate represent the statistical errors of the fitting procedure. The experiments were carried out at $T = 200$ K. The number densities of the reactants in a gas mixture were

[He] = 3 × 10$^{17}$ cm$^{-3}$, [Ar] = 2 × 10$^{14}$ cm$^{-3}$, [H$_2$] portion varying in the range of 4.6 × 10$^{13}$ to 2.6 × 10$^{14}$ cm$^{-3}$. The figure was adapted from reference [72].

The experiments differ by the various fraction of the hydrogen reactant gas. The obtained data set was fitted via applying the integration method which was already explained above. The coincidence of the values of effective recombination rate coefficients within the statistical error of the fitting procedure is obvious. But what is more important in the present case, is that the equality of the measured recombination rate coefficients was observed even for the experimental conditions where the number densities of electron and H$_3^+$ ions and, as a result, the curves diverge greatly on the graph. It means that the rapid recombination of H$_5^+$ ions, which amount increases with the rising of H$_2$ number density due to reaction (14), does not make a crucial problem for the new procedure of the determination of the effective recombination rate coefficient of the investigated ionic species.

As known from the previous low-temperature studies (200 K) of H$_3^+$ ions in He-buffered plasmas, the binary recombination rate coefficient of those molecular ions is equal to $\alpha_0$ = (6.9 ± 2.0) × 10$^{-8}$ cm$^3$s$^{-1}$. The corresponding ternary rate coefficient of H$_3^+$ recombination there was $K_{He}$ = (1.6 ± 0.5) × 10$^{-25}$ cm$^6$s$^{-1}$ [70, 79]. The substitution of these data into equation (12) gives excellent results such as getting $\alpha_{eff}$ (200 K, [He] = 3 × 10$^{17}$ cm$^{-3}$) = (1.17 ± 0.25) × 10$^{-7}$ cm$^3$s$^{-1}$, which are in good agreement with the results of present experiments that are showed in **Figure 19**. The present study includes measurements at several temperatures, such as: $T$ = 200 K, $T$ = 150 K, and $T$ = 115 K. The number density of carrier gas, helium, varied from 1 × 10$^{17}$ up to 3 × 10$^{17}$ cm$^{-3}$. The number density of the molecular hydrogen was in the range of 4 × 10$^{13}$ to 5 × 10$^{14}$ cm$^{-3}$. According to the result of the present experimental research, the simultaneous measurement

of ion and electron number densities and the subsequent appliance of the new fitting procedure, described above, for data processing allows us to obtain a reliable value of recombination rate coefficient even in a case where the investigated ions are not dominant in the afterglow. The standard approach of determination of $\alpha_{\text{eff}}$ (e.g. $1/n_e$ graph in the source [1]) is unusable at this experimental conditions and cannot be applicable in this situation.

## 3.2.2 Determination of A coefficient for $3v_2^1(2,0) \leftarrow 0v_2^0(1,0)$ overtone transition

The multifunctional features of Cryo-SA-CRDS apparatus such as the ability to scan investigated absorption spectrum by means of CRD spectrometer, precise measurement of the strength of chosen absorption line, direct probing of the time evolution of electron number density in afterglow plasma by MW diagnostics, carrying out simultaneous measurement of electron and ion number density evolutions, measurement of the absorbance bonded to the specific transition, allow calculate even more plasma and ion characteristics. According to the model of chemical kinetics mention above [40], the low number densities of molecular hydrogen (e.g. see panel "a" in **Figure 19**) in the plasma right after the MW power outage leads to the domination of $H_3^+$ ions above other ionic species. Based on the measured electron number density, with the assumption of a thermal population of states of $H_3^+$ ions, using the particular absorption line profile, the Einstein A coefficient can be calculated. According to the definition in paper [119], the Einstein A coefficient for the $3v_2^1(2,0) \leftarrow 0v_2^0(1,0)$ transition of $H_3^+$ ions can be determined by:

$$A = \frac{S_{abs}}{n_e L} \frac{8\pi v^2 c Q(T)}{g_u} e^{\frac{hcE_l}{k_B T}} \sqrt{\frac{\pi}{4\ln 2}} w = \frac{S_{abs}}{n_e} C_A \ [s^{-1}] . \qquad (21)$$

Here $S_{abs}$ denotes the measured absorbance at the middle of the absorption line with the Doppler broadening effect. The full width at half maximum (FWHM) of the absorption line is marked as $w$ and was measured in cm⁻¹. The transition wavenumber is shown as $v = 7241.245$ cm⁻¹. The energy of the lower state is $E_l = 86.9591$ cm⁻¹. $Q$ here means the partition function and it has a value of $Q = 20.66$ at $T = 200$ K. The Boltzmann and Planck constants are displayed as $k_B$ and $h$ respectively. The speed of light is denoted as $c$ and it was utilized in cm s⁻¹. $g_u$ represents the statistical weight of the upper state and has a value of 20. The discharge column length was estimated as $L = 6$ cm. The partition function together with the lower and upper energies of the states was obtained from the paper [120]. Based on Equation (21) and the data from **Figure 19** panel a), the Einstein A coefficients were calculated and plotted in **Figure 20**. With the purpose to obtain the same time scale for measured electron number density and measured absorbance $S_{abs}$, the linear interpolation for $n_e$ was applied. As a result, from the first 600 microseconds of afterglow, the value of A Einstein coefficient was determined as $A_{present} = (8.7 \pm 0.5)$ s⁻¹. The current value is in good agreement with the recent theoretical result from the paper [117] where it was reported as $A_{theory} = 9.0758$ s⁻¹.

## 3.2.3 Recombination of H₃⁺ ions with electrons in Ne buffer gas

With the aim to study the recombination of $H_3^+$ ions under the possible influence of third bodies in Ne-buffered plasma, the gas mixture of Ne/Ar/H₂ was periodically ignited by MW discharge. The number densities of the

reactants were in the range of $3 \times 10^{13} - 1 \times 10^{14}$ cm⁻³ for $H_2$, $5 \times 10^{13} - 2 \times 10^{14}$ cm⁻³ for Ar, and $3 \times 10^{17} - 1.2 \times 10^{18}$ cm⁻³ for Ne, respectively. The recombination of $H_3^+$ ions in Ne carrier gas was previously done in one study [60] at 240 K. In that study, the stationary afterglow technique was utilized together with microwave diagnostics for electron number density measurements. By using the mass spectrometer, it was possible to identify ions during the recombination processes. The experiments [60] had
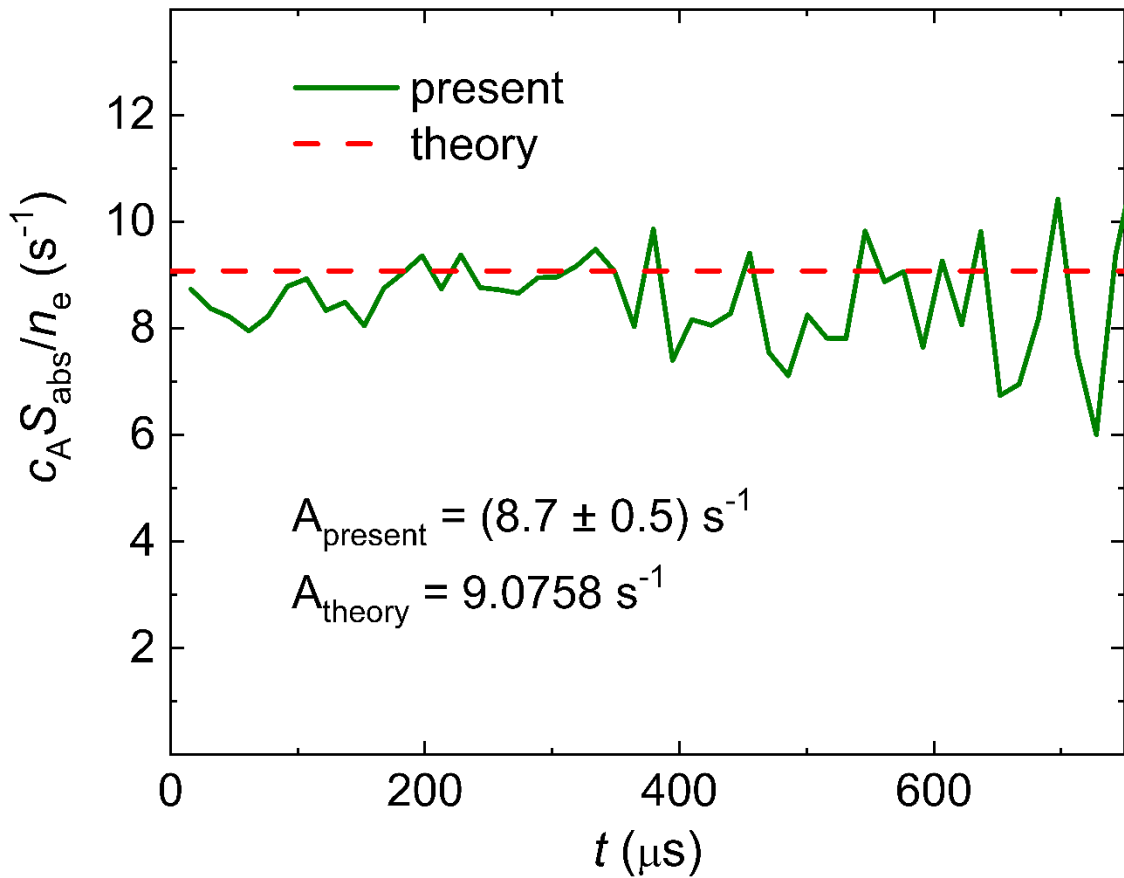


**Figure 20.** The comparison between the Einstein A coefficients for transition $3v_2^1(2,0) \leftarrow 0v_2^0(1,0)$ calculated in present study (full line) and the theoretical data (dashed line). Our calculations use Equation (21) and as a source utilize data from the plot a) in **Figure 12**. The theoretical value

$A_{theory}$ = 9.0758 $s^{-1}$ was taken from the Reference [117]. The figure was adapted from reference [72].

neon number densities in the range from $5.6 \times 10^{17}$ up to $8.0 \times 10^{17}$ $cm^{-3}$ with the amount of molecular hydrogen in a gas mixture $4 \times 10^{13}$ $cm^{-3}$. The results of the measurements [60] show the recombination rate coefficient for $H_3^+$ species in Ne as $\alpha = (1.6 \pm 0.3) \times 10^{-7}$ $cm^3s^{-1}$ which is very close to the values obtained in plasmas with He carrier gas under the similar experimental conditions such as temperature and pressure [34, 40]. The temperature range of the study [60] was limited by the production of $H_5^+$ ions in the probed plasmas which became an obstacle to the measurement at lower temperatures. It is important to note, that the experimental research [60] has a time scale on the order of tens milliseconds. Our present experiment was carried out using hundreds of microseconds as a time scale. That is why the approach that was utilized in our laboratory is more sensitive to the influence of $H_5^+$ ions formation via reaction (15) and this impact must be minimized for the correct experimental results.

The discharge in the present experiment produces plasma which includes such ions as $H_2^+$, $Ar^+$, and $Ne^+$. According to the paper [40], the chain of fast ion molecular reactions with hydrogen transforms argon ions and $H_2^+$ ions into $H_3^+$ species. At the approximately same time, the three-body association reaction will form $Ne_2^+$ molecular ions:

$$Ne^+ + Ne + Ne \rightarrow Ne_2^+ + Ne . \qquad (22)$$
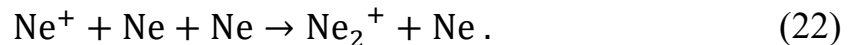
The study conducted by Johnsen $et\ al.$ [118] at 80 K describes a three-body reaction (22) and provides rate coefficients for the two lowest fine structure states of Ne ions: $k(Ne^+\ ^2P_{1/2}) = (3.5 \pm 1.8) \times 10^{-32}$ $cm^6s^{-1}$ and $k(Ne^+\ ^2P_{3/2}) =$

$(12 \pm 3) \times 10^{-32}$ cm$^6$s$^{-1}$. Then, according to the paper [121], molecular neon ions will react with molecular hydrogen:

$$Ne_2^+ + H_2 \rightarrow NeH^+ + Ne + H \, . \tag{23}$$
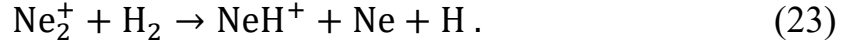
The value of the reaction rate coefficient for reaction (23) at 200 K was determined as $1.1 \times 10^{-10}$ cm$^3$s$^{-1}$ [121]. The production of NeH$^+$ ions is the main channel of the reaction (23). The minor reaction channels, with the possibility of production of NeH$_2^+$ and Ne$_2$H$^+$ ionic species, are also described by Adams *et al.* in the paper [121]. As Adams group reported, the further reaction of the minor channel products with the molecular hydrogen will take place with the reaction rate coefficients not higher than $4.0 \times 10^{-13}$ cm$^3$s$^{-1}$ for NeH$_2^+$ and $9.6 \times 10^{-11}$ cm$^3$s$^{-1}$ for Ne$_2$H$^+$ ions, respectively. One of the main possible limits for H$_3^+$ ions production can be the reaction between molecular hydrogen and NeH$^+$:

$$NeH^+ + H_2 \rightarrow H_3^+ + Ne \, . \tag{24}$$
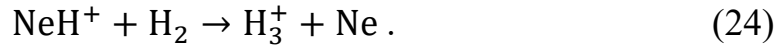
According to Reference [121] this reaction (24) has an extremely low rate coefficient with the value of $2 \times 10^{-11}$ cm$^3$s$^{-1}$. The characteristic time constant for H$_3^+$ ion production through the reaction (24) can be up to 1 ms at the number density of molecular hydrogen [H$_2$] $= 5 \times 10^{13}$. Consequently, only an insignificant amount of H$_3^+$ ionic species in the afterglow plasma will arise thanks to the reaction (24), due to the time scale that was utilized in the present experiment. Hence, our data analysis will not take into account the process (24). To summarize the above-mentioned reactions, it is important to notice that, it is possible to find such ionic species in the early afterglow plasma as H$_3^+$, NeH$^+$, NeH$_2^+$, and H$_5^+$. H$_3^+$ ions are the final products of the ion molecular processes in discharge with the main reactants H$_2$, H$_2^+$, and

Ar$^+$. Ions of NeH$^+$ are produced in the reaction (23) from Ne$_2^+$ ions. Such ions as NeH$_2^+$ or H$_5^+$ are formed in minor reaction channels.

The time evolution of the number densities of H$_3^+$ ions and electrons in the afterglow plasma with Ne buffer gas is displayed in **Figure 21**. The measurements were carried out at $T$ = 110 K. As was already mentioned above, based on the chemical kinetics, H$_3^+$ cannot be dominant ions in afterglow plasmas at such experimental conditions. The estimated amount of H$_3^+$ ions in the present case cannot be higher than one third of all ion species in the afterglow. Measurement showed similar plasma composition even for different number densities of buffer gas and reactant gases. The data were



$$\alpha_{eff} = (1.55 \pm 0.31) \times 10^{-7}\ cm^3 s^{-1}$$
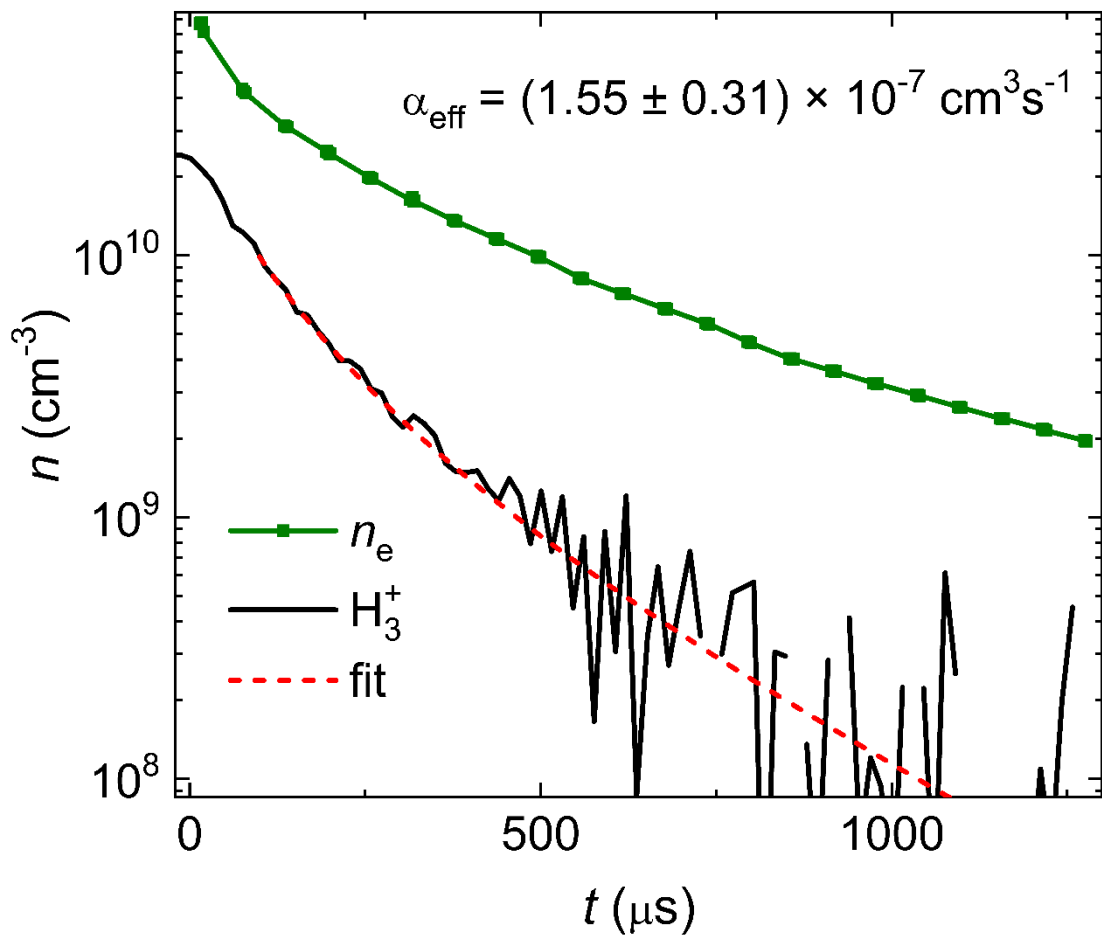
**Figure 21.** The comparison between the time evolution of number densities of H$_3^+$ ions (full line) and electrons (squares) in the afterglow

plasma with Ne carrier gas at $T = 110$ K. The corresponding number densities of reactant gases were: $[Ne] = 6.3 \times 10^{17}$ cm$^{-3}$, $[H_2] = 1.0 \times 10^{14}$ cm$^{-3}$, $[Ar] = 5.4 \times 10^{13}$ cm$^{-3}$. The dashed line denotes the fit to the measured data by means of Equation (18). The obtained effective recombination rate coefficient of $H_3^+$ ions is marked as $\alpha_{eff}$ and the value is displayed in the top part of the plot. The figure was adapted from reference [72].

then fitted by means of Equation (18). In order to show a correlation between obtained recombination rate coefficient of $H_3^+$ ions and Ne buffer gas number density **Figure 22** was plotted. The dependence was fitted by means of Equation (12). As a result, the values of binary and ternary recombination rate coefficient were determined as $\alpha_0$ (110 K) = $(7.0 \pm 1.7) \times 10^{-8}$ cm$^3$s$^{-1}$ and $K_{Ne}$ (110 K) = $(1.8 \pm 0.2) \times 10^{-25}$ cm$^6$s$^{-1}$, respectively. With the purpose to compare present data of ion recombination with our previous results for other carrier gases, the fit for the effective recombination rate coefficient of $H_3^+$ measured in He buffered plasma at 125 K is also displayed in **Figure 22**. The plot in **Figure 22** shows that the values of measured binary and ternary recombination rate coefficients of $H_3^+$ are very close for experiments in helium [36] and neon buffer gases. The conditions of both measurements were similar. In paper [26], Bates and Khare suggested that the rate of recombination of atomic ions with electrons in carrier gas will be proportional to the reciprocal reduced mass of the positive ion-buffer gas atom system at the condition of low temperatures and number densities. According to Reference [26], the ternary recombination rate coefficients of ions of $H_3^+$ should show a difference by a factor of 1.5 between the measurements which were carried out in Ne and He buffer gases. Considering all the uncertainties involved in the measurements and evaluation of the recombination rate coefficient, our findings do not

contradict the aforementioned statement made by Bates and Khare [26]. However, the theory in Reference [26] gives wrong predictions for the estimation of values of ternary recombination rate coefficient of $H_3^+$ in He at 300 K by several orders of magnitude. Consequently, the theory should be improved or utilized only in particular low-temperature situations.
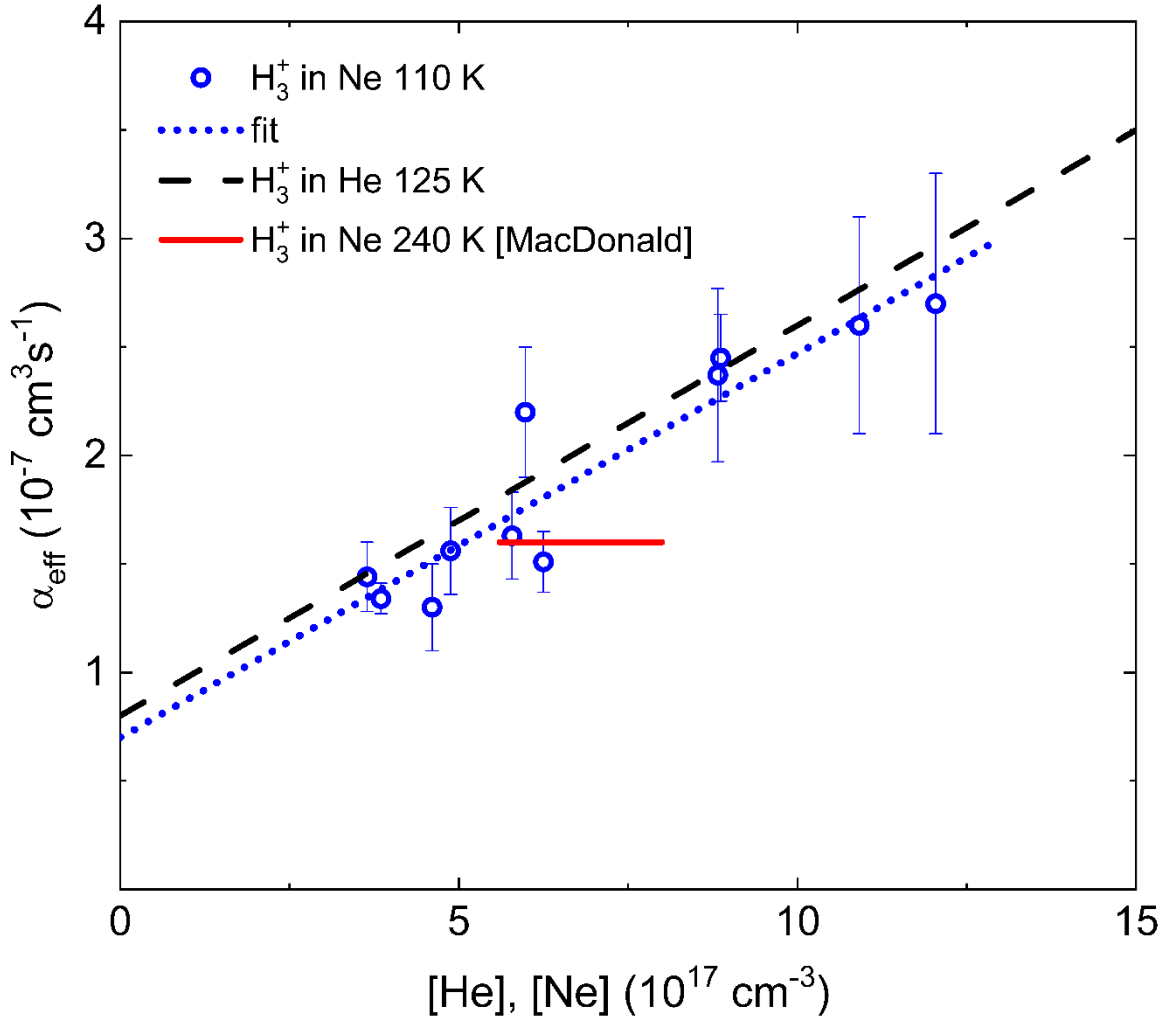


**Figure 22.** The comparison between the effective recombination rate coefficients for recombination of $H_3^+$ ions with electrons measured in the present experiments in neon-buffered plasmas (circles) and values obtained by Dohnal et. al. [36] in helium-buffered plasmas (dashed line). The results are shown in the form of dependence of the effective recombination rate coefficient $\alpha_{\text{eff}}$ on the number densities of utilized buffer gases [Ne] and [He].

The present measurements and Dohnal group experiments were carried out at 110 K and 125 K, respectively. The only previous study of $H_3^+$ recombination in Ne carrier gas was done by MacDonald *et al.* [60] at 240 K and is plotted as a full line. The dotted line denotes the fit to the data of present experiments by applying Equation (12). The figure was adapted from reference [72].

### 3.2.4 Uncertainties and their sources

The value of statistical uncertainty is on the order of $10^9$ cm$^{-3}$ for evaluation of the number density of ions, which can be seen from the scatter of the data in **Figure 19** and **Figure 21**. A source of the systematic uncertainty of experimental determination of ion number density can be the uncertainty of evaluation of the length of the discharge column inside the MW resonator, this value is estimated to reach up to 10%. Another possible source of systematic uncertainty can be the uncertainty of vibrational transition moments which were utilized in the present study. The value is estimated to reach up to 5% [72]. In the case of electron number density determination, the temporal resolution was 2.5 μs and the statistical uncertainty was small, comparable with the width of the corresponding lines in **Figure 19** and **Figure 21**. The source of the systematic uncertainty of the electron number density determination is largely connected with the precision of the evaluation of the resonant frequency of the empty cavity of the cylindrical resonator. Hence, the estimated value of the systematic uncertainty of the electron number density is not bigger than $3 \times 10^8$ cm$^{-3}$. As a result, the overall systematic uncertainty in the determination of the effective recombination rate coefficient of $H_3^+$ ions with electrons is evaluated as 15%.

# 4  CONCLUSIONS

## 4.1 Recombination N$_2$H$^+$ in He

The experimental study of the recombination rate coefficient of N$_2$H$^+$ ions with electrons were done. The experiments covered a temperature range between 80 and 350 K by means of a stationary afterglow setup which was cooled by liquid nitrogen and equipped with a continuous wave modification of cavity ring-down absorption spectrometer. The vibrational and rotational temperatures of the investigated ions were also tracked by measuring the relative population of the corresponding excited states of diazenylium. As a result, we can confidently state, that the internal excitation of N$_2$H$^+$ ions in the afterglow plasma were thermal during the recombination process. A detailed analysis was conducted to investigate the potential impact of ternary recombination processes, facilitated by neutral atoms of the buffer gas, on the measurement of the recombination rate coefficient of N$_2$H$^+$ with electrons. The influence of the three-body recombination channel was not detected. The recombination rate coefficient of diazenylium ions with electrons does not show any statistically significant increase with the variation of the number density of buffer gas in the temperature range of present experiments. Only an upper estimation can be given. It is important to notice also that the effective recombination rate coefficient of diazenylium was the same for the experiments with He buffered plasma and for H$_2$ buffered plasma at corresponding kinetic temperatures $T_{kin} = 325 \pm 10$ K and $T_{kin} = 350 \pm 15$ K.

For the low-temperature range, below 240 K, almost constant values of binary recombination rate coefficient of diazenylium were obtained: $\alpha_{N2H+} = (3.29 \pm 0.04) \times 10^{-7} (T/300 \text{ K})^{-(0.06 \pm 0.02)}$ cm$^3$s$^{-1}$. For the higher temperature

region, the decline of the binary recombination rate coefficient of $N_2H^+$ with the rising in temperature as $\alpha_{N2H+}$ = $(2.81 \pm 0.04) \times 10^{-7}$ $(T/300 \text{ K})^{-(0.81 \pm 0.10)}$ $cm^3s^{-1}$ was observed. The experimental results and calculated characteristics could be useful for creating and developing models of interstellar chemistry which include diazenylium, especially at low temperatures. The data from the present study possibly also could be applied for improving quantum mechanical calculations for the dissociation of polyatomic ions during the recombination processes.

# 4.2 Recombination H$_3^+$ in Ne or He

The new Cryogenic Stationary Afterglow apparatus in conjunction with the near-infrared Cavity Ring-Down Spectrometer was complemented by the Micro-Wave diagnostic for direct precise determination of electron number density in the gas discharge tube. The MW diagnostic uses the effect of the shift of resonance frequency of the MW cavity while plasma electrons change the dielectric permittivity of the MW resonator. The first tests of the new experimental system were carried out utilizing the well-known process of H$_3^+$ ions recombination with electrons in He buffered plasma at conditions that were already reported by the Glosík group in the paper [40]. According to the findings, it is possible to derive dependable recombination rate coefficients under circumstances where the ions being studied are not the dominant ions present in the afterglow plasma. The study employed the current experimental arrangement to determine the Einstein coefficients of a particular observed transition, specifically the $3v_2^1(2,0) \leftarrow 0v_2^0(1,0)$ second overtone transition. The obtained value of $A_{\text{present}}$ was $(8.6 \pm 0.7)$ s$^{-1}$, which agrees well with the latest theoretical prediction of $A_{\text{theory}} = 9.0758$ s$^{-1}$ in the paper [117]. A study was carried out to investigate the third body-assisted recombination of H$_3^+$ ions and electrons in neon carrier gas at a temperature of 110 K. The resulting ternary recombination rate coefficient, $K_{\text{Ne}}$ (110 K), was found to be $(1.8 \pm 0.2) \times 10^{-25}$ cm$^6$s$^{-1}$, which is similar to the value observed in plasmas buffered with helium.

# REFERENCES

[1]    Larsson, M.; Orel, A. E. *Dissociative Recombination of Molecular Ions*; Cambridge molecular science; Cambridge University Press: Cambridge, UK ; New York, **2008**.

[2]    Bates, D. R. Dissociative Recombination. *Phys. Rev.* **1950**, *78* (4), 492 – 493. https://doi.org/10.1103/PhysRev.78.492.

[3]    Kálosi, Á. Elementary Processes at Low Temperatures - Reactions of $H_3^+$ and $N_2H^+$ in Afterglow Plasmas. Prague, **2019**. *Dissertation thesis.* Charles University, Faculty of Mathematics and Physics, Department of Surface and Plasma Science. Supervisor Plašil, R.

[4]    Райзер, Ю. П. *Физика газового разряда*, 3-е изд., перераб. и допа.; Интеллект: Долгопрудный, 2009.

[5]    Gupta, V. P. Interaction of Radiation and Matter and Electronic Spectra. In *Principles and Applications of Quantum Chemistry*; Elsevier, 2016; pp 291 – 337. https://doi.org/10.1016/B978-0-12-803478-1.00009-1.

[6]    Vuitton, V.; Yelle, R. V.; McEwan, M. J. Ion Chemistry and N-Containing Molecules in Titan's Upper Atmosphere. *Icarus* **2007**, *191* (2), 722 – 742. https://doi.org/10.1016/j.icarus.2007.06.023.

[7]    Turner, B. E. U93.174: A New Interstellar Line with Quadrupole Hyperfine Splitting. *Astrophys. J.* **1974**, *193*, L83. https://doi.org/10.1086/181638.

[8]    Turner, B. E. The Physics and Chemistry of Translucent Molecular Clouds. IV. $HCO^+$ and $N_2H^+$. *Astrophys. J.* **1995**, *449*, 635. https://doi.org/10.1086/176085.

[9]    Anderson, D. E.; Blake, G. A.; Bergin, E. A.; Zhang, K.; Carpenter, J. M.; Schwarz, K. R.; Huang, J.; Öberg, K. I. Probing the Gas Content of Late-Stage Protoplanetary Disks with $N_2H^+$. *Astrophys. J.* **2019**, *881* (2), 127. https://doi.org/10.3847/1538-4357/ab2cb5.

[10] Caselli, P.; Walmsley, C. M.; Zucconi, A.; Tafalla, M.; Dore, L.; Myers, P. C. Molecular Ions in L1544. II. The Ionization Degree. *Astrophys. J.* **2002**, *565* (1), 344. https://doi.org/10.1086/324302.

[11] Vigren, E.; Zhaunerchyk, V.; Hamberg, M.; Kaminska, M.; Semaniak, J.; Ugglas, M. af; Larsson, M.; Thomas, R. D.; Geppert, W. D. Reassessment of the Dissociative Recombination of $N_2H^+$ At Cryring. *Astrophys. J.* **2012**, *757* (1), 34. https://doi.org/10.1088/0004-637X/757/1/34.

[12] Mul, P. M.; McGowan, J. W. Dissociative Recombination of $N_2H^+$ and $N_2D^+$. *Astrophys. J.* **1979**, *227*, L157 – L159. https://doi.org/10.1086/182889.

[13] Brian, J.; Mitchell, A. The Dissociative Recombination of Molecular Ions. *Phys. Rep.* **1990**, *186* (5), 215 – 248. https://doi.org/10.1016/0370-1573(90)90159-Y.

[14] Smith, D.; Adams, N. G. Dissociative Recombination Coefficients for $H_3^+$, $HCO^+$, $N_2H^+$, and $CH_5^+$ at Low Temperature: Interstellar Implications. *Astrophys. J.* **1984**, *284*, L13 – L16. https://doi.org/10.1086/184342.

[15] Adams, N. G.; Smith, D.; Alge, E. Measurements of Dissociative Recombination Coefficients of $H_3^+$, $HCO^+$, $N_2H^+$, and $CH_5^+$ at 95 and 300 K Using the FALP Apparatus. *J. Chem. Phys.* **1984**, *81* (4), 1778 – 1784. https://doi.org/10.1063/1.447849.

[16] Geppert, W. D.; Thomas, R.; Semaniak, J.; Ehlerding, A.; Millar, T. J.; Österdahl, F.; Ugglas, M. af; Djurić, N.; Paál, A.; Larsson, M. Dissociative Recombination of $N_2H^+$: Evidence for Fracture of the N-N Bond. *Astrophys. J.* **2004**, *609* (1), 459. https://doi.org/10.1086/420733.

[17] Smith, D.; Španěl, P. Dissociative Recombination of $H_3^+$ and Some Other Interstellar Ions: A Controversy Resolved. *Int. J. Mass Spectrom. Ion*

Process. **1993**, *129*, 163 – 182. https://doi.org/10.1016/0168-1176(93)87040-Y.

[18] Poterya, V.; McLain, J. L.; Adams, N. G.; Babcock, L. M. Mechanisms of Electron-Ion Recombination of $N_2H^+/N_2D^+$ and $HCO^+/DCO^+$ Ions: Temperature Dependence and Isotopic Effect. *J. Phys. Chem. A* **2005**, *109* (32), 7181 – 7186. https://doi.org/10.1021/jp051945b.

[19] Rosati, R. E.; Johnsen, R.; Golde, M. F. Yield of Electronically Excited $N_2$ Molecules from the Dissociative Recombination of $N_2H^+$ with $e^-$. *J. Chem. Phys.* **2004**, *120* (17), 8025 – 8030. https://doi.org/10.1063/1.1695314.

[20] Petrignani, A.; Altevogt, S.; Berg, M. H.; Bing, D.; Grieser, M.; Hoffmann, J.; Jordon-Thaden, B.; Krantz, C.; Mendes, M. B.; Novotný, O.; Novotny, S.; Orlov, D. A.; Repnow, R.; Sorg, T.; Stützel, J.; Wolf, A.; Buhr, H.; Kreckel, H.; Kokoouline, V.; Greene, C. H. Resonant Structure of Low-Energy $H_3^+$ Dissociative Recombination. *Phys. Rev. A* **2011**, *83* (3), 032711. https://doi.org/10.1103/PhysRevA.83.032711.

[21] Amano, T. The Dissociative Recombination Rate Coefficients of $H_3^+$, $HN_2^+$, and $HCO^+$. *J. Chem. Phys.* **1990**, *92* (11), 6492 – 6501. https://doi.org/10.1063/1.458594.

[22] Hickman, A. P.; Kashinski, D. O.; Malenda, R. F.; Gatti, F.; Talbi, D. Calculation of Dissociating Autoionizing States Using the Block Diagonalization Method: Application to $N_2H$. *J. Phys. Conf. Ser.* **2011**, *300* (1), 012016. https://doi.org/10.1088/1742-6596/300/1/012016.

[23] Talbi, D. A Quantum Chemical Study of the $N_2H^+ + e^- \rightarrow N_2 + H$ Reaction I: The Linear Dissociation Path. *Chem. Phys.* **2007**, *332* (2), 298 – 303. https://doi.org/10.1016/j.chemphys.2006.12.009.

[24] Fonseca dos Santos, S.; Douguet, N.; Kokoouline, V.; Orel, A. E. Scattering Matrix Approach to the Dissociative Recombination of $HCO^+$

and $N_2H^+$. *J. Chem. Phys.* **2014**, *140* (16), 164308. https://doi.org/10.1063/1.4871982.

[25] dos Santos, S. F.; Ngassam, V.; Orel, A. E.; Larson, Å. Dissociative Recombination of $N_2H^+$. *Phys. Rev. A* **2016**, *94* (2), 022702. https://doi.org/10.1103/PhysRevA.94.022702.

[26] Bates, D. R.; Khare, S. P. Recombination of Positive Ions and Electrons in a Dense Neutral Gas. *Proc. Phys. Soc.* **1965**, *85* (2), 231. https://doi.org/10.1088/0370-1328/85/2/305.

[27] Deloche, R.; Monchicourt, P.; Cheret, M.; Lambert, F. High-Pressure Helium Afterglow at Room Temperature. *Phys. Rev. A* **1976**, *13* (3), 1140 – 1176. https://doi.org/10.1103/PhysRevA.13.1140.

[28] Dohnal, P.; Rubovič, P.; Kotrík, T.; Hejduk, M.; Plašil, R.; Johnsen, R.; Glosík, J. Collisional-Radiative Recombination of $Ar^+$ Ions with Electrons in Ambient Helium at Temperatures from 50 K to 100 K. *Phys. Rev. A* **2013**, *87* (5), 052716. https://doi.org/10.1103/PhysRevA.87.052716.

[29] Berlande, J.; Cheret, M.; Deloche, R.; Gonfalone, A.; Manus, C. Pressure and Electron Density Dependence of the Electron-Ion Recombination Coefficient in Helium. *Phys. Rev. A* **1970**, *1* (3), 887 – 896. https://doi.org/10.1103/PhysRevA.1.887.

[30] Cao, Y. S.; Johnsen, R. Neutral-stabilized Electron-Ion Recombination in Ambient Helium Gas. *J. Chem. Phys.* **1991**, *94* (8), 5443 – 5446. https://doi.org/10.1063/1.460505.

[31] van Sonsbeek, R. J.; Cooper, R.; Bhave, R. N. Pulse Radiolysis Studies of Ion-Electron Recombination in Helium. Pressure and Temperature Effects. *J. Chem. Phys.* **1992**, *97* (3), 1800 – 1808. https://doi.org/10.1063/1.463167.

[32] Schregel, C.-G.; Carbone, E. A. D.; Luggenhölscher, D.; Czarnetzki, U. Ignition and Afterglow Dynamics of a High Pressure Nanosecond Pulsed

Helium Micro-Discharge: I. Electron, Rydberg Molecules and He (23S) Densities. *Plasma Sources Sci. Technol.* **2016**, *25* (5), 054003. https://doi.org/10.1088/0963-0252/25/5/054003.

[33]  Flannery, M. R. Transport-collisional Master Equations for Termolecular Recombination as a Function of Gas Density. *J. Chem. Phys.* **1991**, *95* (11), 8205 – 8226. https://doi.org/10.1063/1.461300.

[34]  Glosik, J.; Korolov, I.; Plasil, R.; Novotny, O.; Kotrik, T.; Hlavenka, P.; Varju, J.; Mikhailov, I. A.; Kokoouline, V.; Greene, C. H. Recombination of $H_3^+$ Ions in the Afterglow of a He-Ar-$H_2$ Plasma. *J. Phys. B At. Mol. Opt. Phys.* **2008**, *41* (19), 191001. https://doi.org/10.1088/0953-4075/41/19/191001.

[35]  Glosík, J.; Plašil, R.; Korolov, I.; Kotrík, T.; Novotný, O.; Hlavenka, P.; Dohnal, P.; Varju, J.; Kokoouline, V.; Greene, C. H. Temperature Dependence of Binary and Ternary Recombination of $H_3^+$ Ions with Electrons. *Phys. Rev. A* **2009**, *79* (5), 052707. https://doi.org/10.1103/PhysRevA.79.052707.

[36]  Dohnal, P.; Hejduk, M.; Varju, J.; Rubovič, P.; Roučka, Š.; Kotrík, T.; Plašil, R.; Glosík, J.; Johnsen, R. Binary and Ternary Recombination of Para-$H_3^+$ and Ortho-$H_3^+$ with Electrons: State Selective Study at 77 – 200 K. *J. Chem. Phys.* **2012**, *136* (24), 244304. https://doi.org/10.1063/1.4730162.

[37]  Dohnal, P.; Kálosi, Á.; Plašil, R.; Roučka, Š.; Kovalenko, A.; Rednyk, S.; Johnsen, R.; Glosík, J. Binary and Ternary Recombination of $H_2D^+$ and $HD_2^+$ Ions with Electrons at 80 K. *Phys. Chem. Chem. Phys.* **2016**, *18* (34), 23549 – 23553. https://doi.org/10.1039/C6CP04152C.

[38]  Plašil, R.; Dohnal, P.; Kálosi, Á.; Roučka, Š.; Johnsen, R.; Glosík, J. Stationary Afterglow Measurements of the Temperature Dependence of the Electron-Ion Recombination Rate Coefficients of and in He/Ar/$H_2$/$D_2$

Gas Mixtures at $T = 80 - 145$ K. *Plasma Sources Sci. Technol.* **2017**, *26* (3), 035006. https://doi.org/10.1088/1361-6595/aa5916.

[39]   Dohnal, P.; Rubovič, P.; Kálosi, Á.; Hejduk, M.; Plašil, R.; Johnsen, R.; Glosík, J. $H_2$-Assisted Ternary Recombination of $H_3^+$ with Electrons at 300 K. *Phys. Rev. A* **2014**, *90* (4), 042708. https://doi.org/10.1103/PhysRevA.90.042708.

[40]   Glosík, J.; Dohnal, P.; Rubovič, P.; Kálosi, Á.; Plašil, R.; Roučka, Š.; Johnsen, R. Recombination of $H_3^+$ Ions with Electrons in $He/H_2$ Ambient Gas at Temperatures from 240 K to 340 K. *Plasma Sources Sci. Technol.* **2015**, *24* (6), 065017. https://doi.org/10.1088/0963-0252/24/6/065017.

[41]   Thomson, J. J. XXVI. Rays of Positive Electricity. *Lond. Edinb. Dublin Philos. Mag. J. Sci.* **1911**, *21* (122), 225 – 249. https://doi.org/10.1080/14786440208637024.

[42]   Hogness, T. R.; Lunn, E. G. The Ionization of Hydrogen by Electron Impact as Interpreted by Positive Ray Analysis. *Phys. Rev.* **1925**, *26* (1), 44 – 55. https://doi.org/10.1103/PhysRev.26.44.

[43]   Coulson, C. A. The Electronic Structure of $H_3^+$. *Math. Proc. Camb. Philos. Soc.* **1935**, *31* (2), 244 – 259. https://doi.org/10.1017/S0305004100013347.

[44]   Oka, T. Observation of the Infrared Spectrum of $H_3^+$. *Phys. Rev. Lett.* **1980**, *45* (7), 531 – 534. https://doi.org/10.1103/PhysRevLett.45.531.

[45]   Herbst, E.; Klemperer, W. The Formation and Depletion of Molecules in Dense Interstellar Clouds. *Astrophys. J.* **1973**, *185*, 505 – 534. https://doi.org/10.1086/152436.

[46]   Oka, T. Interstellar $H_3^+$. *Proc. Natl. Acad. Sci.* **2006**, *103* (33), 12235 – 12242. https://doi.org/10.1073/pnas.0601242103.

[47]   Drossart, P.; Maillard, J.-P.; Caldwell, J.; Kim, S. J.; Watson, J. K. G.; Majewski, W. A.; Tennyson, J.; Miller, S.; Atreya, S. K.; Clarke, J. T.;

Waite Jr., J. H.; Wagener, R. Detection of $H_3^+$ on Jupiter. *Nature* **1989**, *340* (6234), 539 – 541. https://doi.org/10.1038/340539a0.

[48] Geballe, T. R.; Jagod, M.-F.; Oka, T. Detection of $H_3^+$ Infrared Emission Lines in Saturn. *Astrophys. J.* **1993**, *408*, L109. https://doi.org/10.1086/186843.

[49] Trafton, L. M.; Geballe, T. R.; Miller, S.; Tennyson, J.; Ballester, G. E. Detection of $H_3^+$ from Uranus. *Astrophys. J.* **1993**, *405* (2), 761 – 766. https://doi.org/10.1086/172404.

[50] Oka, T. Chemistry, Astronomy and Physics of $H_3^+$. *Philos. Trans. R. Soc. Math. Phys. Eng. Sci.* **2012**, *370* (1978), 4991 – 5000. https://doi.org/10.1098/rsta.2012.0243.

[51] Geppert, W. D.; Larsson, M. Dissociative Recombination in the Interstellar Medium and Planetary Ionospheres. *Mol. Phys.* **2008**, *106* (16 – 18), 2199 – 2226. https://doi.org/10.1080/00268970802322074.

[52] Sundström, G.; Mowat, J. R.; Danared, H.; Datz, S.; Broström, L.; Filevich, A.; Källberg, A.; Mannervik, S.; Rensfelt, K. G.; Sigray, P.; Ugglas, M. af; Larsson, M. Destruction Rate of $H_3^+$ by Low-Energy Electrons Measured in a Storage-Ring Experiment. *Science* **1994**, *263* (5148), 785 – 787. https://doi.org/10.1126/science.263.5148.785.

[53] McCall, B. J.; Huneycutt, A. J.; Saykally, R. J.; Djuric, N.; Dunn, G. H.; Semaniak, J.; Novotny, O.; Al-Khalili, A.; Ehlerding, A.; Hellberg, F.; Kalhori, S.; Neau, A.; Thomas, R. D.; Paal, A.; Österdahl, F.; Larsson, M. Dissociative Recombination of Rotationally Cold $H_3^+$. *Phys. Rev. A* **2004**, *70* (5), 052716. https://doi.org/10.1103/PhysRevA.70.052716.

[54] Leu, M. T.; Biondi, M. A.; Johnsen, R. Measurements of Recombination of Electrons with $H_3^+$ and $H_5^+$ Ions. *Phys. Rev. A* **1973**, *8* (1), 413 – 419. https://doi.org/10.1103/PhysRevA.8.413.

[55] Glosík, J.; Novotný, O.; Pysanenko, A.; Zakouřil, P.; Plašil, R.; Kudrna, P.; Poterya, V. The Recombination of $H_3^+$ and $H_5^+$ Ions with

Electrons in Hydrogen Plasma: Dependence on Temperature and on Pressure of $H_2$. *Plasma Sources Sci. Technol.* **2003**, *12* (4), S117 – S122. https://doi.org/10.1088/0963-0252/12/4/027.

[56] Michels, H. H.; Hobbs, R. H. Low-temperature dissociative recombination of $e^- + H_3^+$. *Astrophys J* **1984**, *286*.

[57] Kokoouline, V.; Greene, C. H.; Esry, B. D. Mechanism for the Destruction of $H_3^+$ Ions by Electron Impact. *Nature* **2001**, *412* (6850), 891 – 894. https://doi.org/10.1038/35091025.

[58] Jungen, Ch.; Pratt, S. T. Jahn-Teller Interactions in the Dissociative Recombination of $H_3^+$. *Phys. Rev. Lett.* **2009**, *102* (2), 023201. https://doi.org/10.1103/PhysRevLett.102.023201.

[59] Glosík, J.; Korolov, I.; Plašil, R.; Kotrík, T.; Dohnal, P.; Novotný, O.; Varju, J.; Roučka, Š.; Greene, C. H.; Kokoouline, V. Binary and Ternary Recombination of $D_3^+$ Ions with Electrons in He-$D_2$ Plasma. *Phys. Rev. A* **2009**, *80* (4), 042706. https://doi.org/10.1103/PhysRevA.80.042706.

[60] Macdonald, J. A.; Biondi, M. A.; Johnsen, R. Recombination of Electrons with $H_3^+$ and $H_5^+$ Ions. *Planet. Space Sci.* **1984**, *32* (5), 651 – 654. https://doi.org/10.1016/0032-0633(84)90117-X.

[61] Romanini, D.; Kachanov, A. A.; Stoeckel, F. Diode Laser Cavity Ring down Spectroscopy. *Chem. Phys. Lett.* **1997**, *270* (5), 538 – 545. https://doi.org/10.1016/S0009-2614(97)00406-5.

[62] Romanini, D.; Kachanov, A. A.; Sadeghi, N.; Stoeckel, F. CW Cavity Ring down Spectroscopy. *Chem. Phys. Lett.* **1997**, *264* (3), 316 – 322. https://doi.org/10.1016/S0009-2614(96)01351-6.

[63] Macko, P.; Bánó, G.; Hlavenka, P.; Plašil, R.; Poterya, V.; Pysanenko, A.; Votava, O.; Johnsen, R.; Glosík, J. Afterglow Studies of $H_3^+$(V=0) Recombination Using Time Resolved Cw-Diode Laser Cavity Ring-down Spectroscopy. *Int. J. Mass Spectrom.* **2004**, *233* (1), 299 – 304. https://doi.org/10.1016/j.ijms.2003.12.035.

[64] Hlavenka, P.; Korolov, I.; Plašil, R.; Varju, J.; Kotrík, T.; Glosík, J. Near Infrared Second Overtone Cw-Cavity Ringdown Spectroscopy of $H_2D^+$ Ions. *Czechoslov. J. Phys.* **2006**, *56* (2), B749 – B760. https://doi.org/10.1007/s10582-006-0280-6.

[65] Hlavenka, P.; Plašil, R.; Bánó, G.; Korolov, I.; Gerlich, D.; Ramanlal, J.; Tennyson, J.; Glosík, J. Near Infrared Second Overtone Cw-Cavity Ringdown Spectroscopy of $D_2H^+$ Ions. *Int. J. Mass Spectrom.* **2006**, *255 – 256*, 170 – 176. https://doi.org/10.1016/j.ijms.2006.02.002.

[66] Glosík, J.; Hlavenka, P.; Plašil, R.; Windisch, F.; Gerlich, D.; Wolf, A.; Kreckel, H. Action Spectroscopy of $H_3^+$ and $D_2H^+$ Using Overtone Excitation. *Philos. Trans. R. Soc. Math. Phys. Eng. Sci.* **2006**, *364* (1848), 2931 – 2942. https://doi.org/10.1098/rsta.2006.1866.

[67] Hejduk, M. Reactions of Hydrogen Molecules with Ions and Recombination of $H_3^+$ Ions with Electrons at Cryogenic Temperatures. Prague, **2013**. *Dissertation thesis.* Charles University, Faculty of Mathematics and Physics, Department of Surface and Plasma Science. Supervisor Glosík, J.

[68] Gordon, I. E.; Rothman, L. S.; Hill, C.; Kochanov, R. V.; Tan, Y.; Bernath, P. F.; Birk, M.; Boudon, V.; Campargue, A.; Chance, K. V.; Drouin, B. J.; Flaud, J.-M.; Gamache, R. R.; Hodges, J. T.; Jacquemart, D.; Perevalov, V. I.; Perrin, A.; Shine, K. P.; Smith, M.-A. H.; Tennyson, J.; Toon, G. C.; Tran, H.; Tyuterev, V. G.; Barbe, A.; Császár, A. G.; Devi, V. M.; Furtenbacher, T.; Harrison, J. J.; Hartmann, J.-M.; Jolly, A.; Johnson, T. J.; Karman, T.; Kleiner, I.; Kyuberis, A. A.; Loos, J.; Lyulin, O. M.; Massie, S. T.; Mikhailenko, S. N.; Moazzen-Ahmadi, N.; Müller, H. S. P.; Naumenko, O. V.; Nikitin, A. V.; Polyansky, O. L.; Rey, M.; Rotger, M.; Sharpe, S. W.; Sung, K.; Starikova, E.; Tashkun, S. A.; Auwera, J. V.; Wagner, G.; Wilzewski, J.; Wcisło, P.; Yu, S.; Zak, E. J. The HITRAN2016 Molecular Spectroscopic Database. *J. Quant.*

*Spectrosc. Radiat. Transf.* **2017**, *203*, 3 – 69. https://doi.org/10.1016/j.jqsrt.2017.06.038.

[69]  Hemsworth, R. S.; Payzant, J. D.; Schiff, H. I.; Bohme, D. K. Rate Constants at 297°K for Proton Transfer Reactions with $NH_3$. Comparisons with Classical Theories and Exothermicity. *Chem. Phys. Lett.* **1974**, *26* (3), 417 – 421. https://doi.org/10.1016/0009-2614(74)89061-5.

[70]  Kálosi, Á.; Dohnal, P.; Shapko, D.; Roučka, Š.; Plašil, R.; Johnsen, R.; Glosík, J. Overtone Spectroscopy of $N_2H^+$ Molecular Ions—Application of Cavity Ring-down Spectroscopy. *J. Instrum.* **2017**, *12* (10), C10010. https://doi.org/10.1088/1748-0221/12/10/C10010.

[71]  Plašil, R.; Dohnal, P.; Kálosi, Á.; Roučka, Š.; Shapko, D.; Rednyk, S.; Johnsen, R.; Glosík, J. Stationary Afterglow Apparatus with CRDS for Study of Processes in Plasmas from 300 K down to 30 K. *Rev. Sci. Instrum.* **2018**, *89* (6), 063116. https://doi.org/10.1063/1.5036834.

[72]  Shapko, D.; Dohnal, P.; Roučka, Š.; Uvarova, L.; Kassayová, M.; Plašil, R.; Glosík, J. Cavity Ring-down Spectroscopy Study of Neon Assisted Recombination of $H_3^+$ Ions with Electrons. *J. Mol. Spectrosc.* **2021**, *378*, 111450. https://doi.org/10.1016/j.jms.2021.111450.

[73]  Dohnal, P.; Shapko, D.; Kálosi, Á.; Kassayová, M.; Roučka, Š.; Rednyk, S.; Plašil, R.; Hejduk, M.; Glosík, J. Towards State Selective Recombination of $H_3^+$ under Astrophysically Relevant Conditions. *Faraday Discuss.* **2019**, *217* (0), 220 – 234. https://doi.org/10.1039/C8FD00214B.

[74]  Brown, S. C.; Rose, D. J. Methods of Measuring the Properties of Ionized Gases at High Frequencies. I. Measurements of Q. *J. Appl. Phys.* **2004**, *23* (7), 711 – 718. https://doi.org/10.1063/1.1702287.

[75] Sícha, M.; Gajdusek, J.; Veprek, S. Comparison of Microwave and Probe Methods of Plasma Diagnostics. *Br. J. Appl. Phys.* **1966**, *17* (11), 1511 – 1514. https://doi.org/10.1088/0508-3443/17/11/417.

[76] Gwarek, W. K. Analysis of an Arbitrarily-Shaped Planar Circuit—A Time-Domain Approach. *IEEE Trans. Microw. Theory Tech.* **1985**, *MTT-33* (10), 1067 – 1072. https://doi.org/10.1109/TMTT.1985.1133170.

[77] Rennings, A.; Mosig, J.; Caloz, C.; Erni, D.; Waldow, P. Equivalent Circuit (EC) FDTD Method for the Modeling of Surface Plasmon Based Couplers. *J. Comput. Theor. Nanosci.* **2008**, *5* (4), 690 – 703. https://doi.org/10.1166/jctn.2008.040.

[78] Liebig, T.; Rennings, A.; Held, S.; Erni, D. OpenEMS – a Free and Open Source Equivalent-Circuit (EC) FDTD Simulation Platform Supporting Cylindrical Coordinates Suitable for the Analysis of Traveling Wave MRI Applications. *Int. J. Numer. Model. Electron. Netw. Devices Fields* **2013**, *26* (6), 680 – 696. https://doi.org/10.1002/jnm.1875.

[79] Špirko, V.; Bludský, O.; Kraemer, W. P. Energies and Electric Dipole Moments of the Bound Vibrational States of $HN_2^+$ and $DN_2^+$. *Collect. Czechoslov. Chem. Commun.* **2008**, *73* (6), 873 – 897. https://doi.org/10.1135/cccc20080873.

[80] Shapko, D.; Dohnal, P.; Kassayová, M.; Kálosi, Á.; Rednyk, S.; Roučka, Š.; Plašil, R.; Augustovičová, L. D.; Johnsen, R.; Špirko, V.; Glosík, J. Dissociative Recombination of $N_2H^+$ Ions with Electrons in the Temperature Range of 80 – 350 K. *J. Chem. Phys.* **2020**, *152* (2), 024301. https://doi.org/10.1063/1.5128330.

[81] Kabbadj, Y.; Huet, T. R.; Rehfuss, B. D.; Gabrys, C. M.; Oka, T. Infrared Spectroscopy of Highly Excited Vibrational Levels of Protonated Nitrogen, $HN_2^+$. *J. Mol. Spectrosc.* **1994**, *163* (1), 180 – 205. https://doi.org/10.1006/jmsp.1994.1016.

[82] Kálosi, Á.; Dohnal, P.; Augustovičová, L.; Roučka, Š.; Plašil, R.; Glosík, J. Monitoring the Removal of Excited Particles in He/Ar/H$_2$ Low Temperature Afterglow Plasma at 80 – 300 K. *Eur. Phys. J. Appl. Phys.* **2016**, *75* (2), 24707. https://doi.org/10.1051/epjap/2016150587.

[83] Glosík, J.; Dohnal, P.; Kálosi, Á.; Augustovičová, L. D.; Shapko, D.; Roučka, Š.; Plašil, R. Electron-Ion Recombination in Low Temperature Hydrogen/Deuterium Plasma. *Eur. Phys. J. Appl. Phys.* **2017**, *80* (3), 30801. https://doi.org/10.1051/epjap/2017170228.

[84] Tom, B. A.; Zhaunerchyk, V.; Wiczer, M. B.; Mills, A. A.; Crabtree, K. N.; Kaminska, M.; Geppert, W. D.; Hamberg, M.; af Ugglas, M.; Vigren, E.; van der Zande, W. J.; Larsson, M.; Thomas, R. D.; McCall, B. J. Dissociative Recombination of Highly Enriched Para-H$_3^+$. *J. Chem. Phys.* **2009**, *130* (3), 031101. https://doi.org/10.1063/1.3065970.

[85] Meot-Ner, M.; Field, F. H. Kinetics and Thermodynamics of Association Reactions of CO$^{+\bullet}$ and HCO$^+$ with CO and of N$_2^{+\bullet}$ and N$_2$H$^+$ with N$_2$ between 120 and 650 °K. *J. Chem. Phys.* **2003**, *61* (9), 3742 – 3749. https://doi.org/10.1063/1.1682560.

[86] von Hahn, R.; Becker, A.; Berg, F.; Blaum, K.; Breitenfeldt, C.; Fadil, H.; Fellenberger, F.; Froese, M.; George, S.; Göck, J.; Grieser, M.; Grussie, F.; Guerin, E. A.; Heber, O.; Herwig, P.; Karthein, J.; Krantz, C.; Kreckel, H.; Lange, M.; Laux, F.; Lohmann, S.; Menk, S.; Meyer, C.; Mishra, P. M.; Novotný, O.; O'Connor, A. P.; Orlov, D. A.; Rappaport, M. L.; Repnow, R.; Saurabh, S.; Schippers, S.; Schröter, C. D.; Schwalm, D.; Schweikhard, L.; Sieber, T.; Shornikov, A.; Spruck, K.; Sunil Kumar, S.; Ullrich, J.; Urbain, X.; Vogel, S.; Wilhelm, P.; Wolf, A.; Zajfman, D. The Cryogenic Storage Ring CSR. *Rev. Sci. Instrum.* **2016**, *87* (6), 063115. https://doi.org/10.1063/1.4953888.

[87] Novotný, O.; Wilhelm, P.; Paul, D.; Kálosi, Á.; Saurabh, S.; Becker, A.; Blaum, K.; George, S.; Göck, J.; Grieser, M.; Grussie, F.; von Hahn, R.;

Krantz, C.; Kreckel, H.; Meyer, C.; Mishra, P. M.; Muell, D.; Nuesslein, F.; Orlov, D. A.; Rimmler, M.; Schmidt, V. C.; Shornikov, A.; Terekhov, A. S.; Vogel, S.; Zajfman, D.; Wolf, A. Quantum-State-Selective Electron Recombination Studies Suggest Enhanced Abundance of Primordial HeH$^+$. *Science* **2019**, *365* (6454), 676 – 679. https://doi.org/10.1126/science.aax5921.

[88]    Botschwina, P. An Ab Initio Calculation of the Frequencies and IR Intensities of the Stretching Vibrations of HN$_2^+$. *Chem. Phys. Lett.* **1984**, *107* (6), 535 – 541. https://doi.org/10.1016/S0009-2614(84)85152-0.

[89]    Strömholm, C.; Semaniak, J.; Rosén, S.; Danared, H.; Datz, S.; van der Zande, W.; Larsson, M. Dissociative Recombination and Dissociative Excitation of $^4$HeH$^+$: Absolute Cross Sections and Mechanisms. *Phys. Rev. A* **1996**, *54* (4), 3086 – 3094. https://doi.org/10.1103/PhysRevA.54.3086.

[90]    Sutcliffe, B. T.; Tennyson, J. A Generalized Approach to the Calculation of Ro-Vibrational Spectra of Triatomic Molecules. *Mol. Phys.* **1986**, *58* (6), 1053 – 1066. https://doi.org/10.1080/00268978600101801.

[91]    Havenith, M.; Zwart, E.; Leo Meerts, W.; ter Meulen, J. J. Determination of the Electric Dipole Moment of HN$_2^+$. *J. Chem. Phys.* **1990**, *93* (12), 8446 – 8451. https://doi.org/10.1063/1.459282.

[92]    Keim, E. R.; Polak, M. L.; Owrutsky, J. C.; Coe, J. V.; Saykally, R. J. Absolute Infrared Vibrational Band Intensities of Molecular Ions Determined by Direct Laser Absorption Spectroscopy in Fast Ion Beams. *J. Chem. Phys.* **1990**, *93* (5), 3111 – 3119. https://doi.org/10.1063/1.458845.

[93]    Botschwina, P. Infrared Intensities of Polyatomic Molecules Calculated from SCEP Dipole-Moment Functions and Anharmonic Vibrational Wavefunctions. I. Stretching Vibrations of the Linear Molecules HCN,

HCP and $C_2N_2$. *Chem. Phys.* **1983**, *81* (1), 73 – 85. https://doi.org/10.1016/0301-0104(83)85303-8.

[94] Hindmarsh, A. C. "ODEPACK: A systematized collection of ODE solvers," in *Scientific Computing*, IMACS Transactions on Scientific Computation Vol. 1, edited by R. S. Stepleman (North-Holland, **1983**), pp. 55 – 64.

[95] Lindinger, W.; Schmeltekopf, A. L.; Fehsenfeld, F. C. Temperature Dependence of De-excitation Rate Constants of He($2\,^3S$) by Ne, Ar, Xe, $H_2$, $N_2$, $O_2$, $NH_3$, and $CO_2$. *J. Chem. Phys.* **1974**, *61* (7), 2890 – 2895. https://doi.org/10.1063/1.1682429.

[96] Martin, D. W.; Weiser, C.; Sperlein, R. F.; Bernfeld, D. L.; Siska, P. E. Collision Energy Dependence of Product Branching in Penning Ionization: He*($2\,^1S$, $2\,^3S$) + $H_2$, $D_2$, and HD. *J. Chem. Phys.* **1989**, *90* (3), 1564 – 1576. https://doi.org/10.1063/1.456049.

[97] Glosík, J.; Bánó, G.; Plašil, R.; Luca, A.; Zakouřil, P. Study of the Electron Ion Recombination in High Pressure Flowing Afterglow: Recombination of $NH_4 \cdot + (NH_3)_2$. *Int. J. Mass Spectrom.* **1999**, *189* (2), 103 – 113. https://doi.org/10.1016/S1387-3806(99)00058-5.

[98] Ikezoe, Y.; Matsuoka, S.; Takebe, M.; Viggiano, A. A. Gas Phase Ion-Molecule Reaction Rate Constants Through 1986 (Maruzen Company Ltd, Tokyo, 1987). *Search PubMed* **1986**.

[99] Adams, N. G.; Smith, D. Product-Ion Distributions for Some Ion-Molecule Reactions. *J. Phys. B At. Mol. Phys.* **1976**, *9* (8), 1439. https://doi.org/10.1088/0022-3700/9/8/024.

[100] Bohme, D. K.; Mackay, G. I.; Schiff, H. I. Determination of Proton Affinities from the Kinetics of Proton Transfer Reactions. VII. The Proton Affinities of $O_2$, $H_2$, Kr, O, $N_2$, Xe, $CO_2$, $CH_4$, $N_2O$, and CO. *J. Chem. Phys.* **2008**, *73* (10), 4976 – 4986. https://doi.org/10.1063/1.439975.

[101] Adams, N. G.; Smith, D. The Selected Ion Flow Tube (SIFT); A Technique for Studying Ion-Neutral Reactions. *Int. J. Mass Spectrom. Ion Phys.* **1976**, *21* (3), 349 – 359. https://doi.org/10.1016/0020-7381(76)80133-7.

[102] Lindinger, W.; Fehsenfeld, F. C.; Schmeltekopf, A. L.; Ferguson, E. E. Temperature Dependence of Some Ionospheric Ion-Neutral Reactions from $300° – 900°K$. *J. Geophys. Res. 1896-1977* **1974**, *79* (31), 4753 – 4756. https://doi.org/10.1029/JA079i031p04753.

[103] Bedford, D. K.; Smith, D. Variable-Temperature Selected Ion Flow Tube Studies of the Reactions of $Ar^+$, $Ar_2^+$ and $ArH^+_n$ (n = 1-3) Ions With $H_2$, HD and $D_2$ at 300 K and 80 K. *Int. J. Mass Spectrom. Ion Process.* **1990**, *98* (2), 179 – 190. https://doi.org/10.1016/0168-1176(90)85017-V.

[104] Smith, D.; Adams, N. G. Charge-Transfer Reaction $Ar^+ + N_2 \rightleftarrows N_2^+ + Ar$ at Thermal Energies. *Phys. Rev. A* **1981**, *23* (5), 2327 – 2330. https://doi.org/10.1103/PhysRevA.23.2327.

[105] Villinger, H.; Futrell, J. H.; Howorka, F.; Duric, N.; Lindinger, W. The Proton Transfer from $ArH^+$ to Various Neutrals. *J. Chem. Phys.* **1982**, *76* (7), 3529 – 3534. https://doi.org/10.1063/1.443454.

[106] Chatterjee, B. K.; Johnsen, R. An Estimating Formula for Ion-Atom Association Rates in Gases. *J. Chem. Phys.* **1990**, *93* (8), 5681 – 5684. https://doi.org/10.1063/1.459561.

[107] Glosík, J. Measurement of the Reaction Rate Coefficients of Reactions of $H_2^+$ with Ne, Ar, Kr, Xe, $H_2$, $D_2$, $N_2$ and $CH_4$ at Thermal Energy. *Int. J. Mass Spectrom. Ion Process.* **1994**, *139*, 15 – 23. https://doi.org/10.1016/0168-1176(94)90004-3.

[108] Kim, J. K.; Huntress, W. T., Jr. Ion Cyclotron Resonance Studies on the Reaction of $H_2^+$ and $D_2^+$ Ions with Various Simple Molecules and Hydrocarbons. *J. Chem. Phys.* **2008**, *62* (7), 2820 – 2825. https://doi.org/10.1063/1.430817.

[109] Rubovič, P.; Dohnal, P.; Hejduk, M.; Plašil, R.; Glosík, J. Binary Recombination of $H_3^+$ and $D_3^+$ Ions with Electrons in Plasma at $50 - 230$ K. *J. Phys. Chem. A* **2013**, *117* (39), $9626 - 9632$. https://doi.org/10.1021/jp3123192.

[110] Praxmarer, C.; Hansel, A.; Lindinger, W. Interaction between the Ion Dipole and the Ion-induced Dipole in Reactions of the Polar Ion $ArH_3^+$. *J. Chem. Phys.* **1994**, *100* (12), $8884 - 8889$. https://doi.org/10.1063/1.466691.

[111] Adams, N. G.; Smith, D. A Study of the Nearly Thermoneutral Reactions of $N^+$ with $H_2$, HD and $D_2$. *Chem. Phys. Lett.* **1985**, *117* (1), $67 - 70$. https://doi.org/10.1016/0009-2614(85)80407-3.

[112] Zymak, I.; Hejduk, M.; Mulin, D.; Plašil, R.; Glosík, J.; Gerlich, D. Low-temperature Ion Trap Studies of $N^+(^3P_{ja}) + H_2(j) \rightarrow NH^+ + H$. *Astrophys.J.* **2013**, *768* (1), 86. https://doi.org/10.1088/0004-637X/768/1/86.

[113] de Gouw, J. A.; Ding, L. N.; Frost, M. J.; Kato, S.; Bierbaum, V. M.; Leone, S. R. Vibrational Energy Dependence of the Reaction $N_2^+(v) + H_2 \rightarrow N_2H^+ + H$ at Thermal Energies. *Chem. Phys. Lett.* **1995**, *240* (4), $362 - 368$. https://doi.org/10.1016/0009-2614(95)00545-F.

[114] Alge, E.; Adams, N. G.; Smith, D. Measurements of the Dissociative Recombination Coefficients of $O_2^+$, $NO^+$ and $NH_4^+$ in the Temperature Range $200 - 600$ K. *J. Phys. B At. Mol. Phys.* **1983**, *16* (8), 1433. https://doi.org/10.1088/0022-3700/16/8/017.

[115] Rednyk, S.; Roučka, Š.; Kovalenko, A.; Tran, T. D.; Dohnal, P.; Plašil, R.; Glosík, J. Reaction of $NH^+$, $NH_2^+$, and $NH_3^+$ Ions with $H_2$ at Low Temperatures - The Pathway to Ammonia Production in the Interstellar Medium. *Astron. Astrophys.* **2019**, *625*, A74. https://doi.org/10.1051/0004-6361/201834149.

[116] Crabtree, K. N.; McCall, B. J. On the Symmetry and Degeneracy of $H_3^+$. *J. Phys. Chem. A* **2013**, *117* (39), 9950 – 9958. https://doi.org/10.1021/jp400080j.

[117] Mizus, I. I.; Alijah, A.; Zobov, N. F.; Lodi, L.; Kyuberis, A. A.; Yurchenko, S. N.; Tennyson, J.; Polyansky, O. L. ExoMol Molecular Line Lists – XX. A Comprehensive Line List for $H_3^+$. *Mon. Not. R. Astron. Soc.* **2017**, *468* (2), 1717 – 1725. https://doi.org/10.1093/mnras/stx502.

[118] Johnsen, R.; Rubovič, P.; Dohnal, P.; Hejduk, M.; Plašil, R.; Glosík, J. Ternary Recombination of $H_3^+$ and $D_3^+$ with Electrons in He – $H_2$ ($D_2$) Plasmas at Temperatures from 50 to 300 K. *J. Phys. Chem. A* **2013**, *117* (39), 9477 – 9485. https://doi.org/10.1021/jp311978n.

[119] Rothman, L. S.; Rinsland, C. P.; Goldman, A.; Massie, S. T.; Edwards, D. P.; Flaud, J.-M.; Perrin, A.; Camy-peyret, C.; Dana, V.; Mandin, J.-Y.; Schroeder, J.; Mccann, A.; Gamache, R. R.; Wattson, R. B.; Yoshino, K.; Chance, K. V.; Jucks, K. W.; Brown, L. R.; Nemtchinov, V.; Varanasi, P. The HITRAN Molecular Spectroscopic Database and HAWKS (HITRAN Atmospheric Workstation): 1996 edition. *J. Quant. Spectrosc. Radiat. Transf.* **1998**, *60* (5), 665 – 710. https://doi.org/10.1016/S0022-4073(98)00078-8.

[120] Neale, L.; Miller, S.; Tennyson, L. J. Spectroscopic Properties of the $H_3^+$ Molecule: A New Calculated Line List. *Astrophys. J.* **1996**, *464* (1 Part I), 516 – 520. https://doi.org/10.1086/177341.

[121] Adams, N. G.; Bohme, D. K.; Ferguson, E. E. Reactions of $He_2^+$, $Ne_2^+$, $Ar_2^+$, and Rare-Gas Hydride Ions with Hydrogen at 200°K. *J. Chem. Phys.* **1970**, *52* (10), 5101 – 5105. https://doi.org/10.1063/1.1672748.

# 5   ATTACHED PUBLICATIONS

1.  Glosík, J.; Dohnal, P.; Kálosi, Á.; Augustovičová, L. D.; **Shapko, D.**; Roučka, Š.; Plašil, R. Electron-Ion Recombination in Low Temperature Hydrogen/Deuterium Plasma. *Eur. Phys. J. Appl. Phys.* **2017**, *80* (3), 30801. https://doi.org/10.1051/epjap/2017170228.

2.  Kálosi, Á.; Dohnal, P.; **Shapko, D.**; Roučka, Š.; Plašil, R.; Johnsen, R.; Glosík, J. Overtone Spectroscopy of $N_2H^+$ Molecular Ions—Application of Cavity Ring-down Spectroscopy. *J. Instrum.* **2017**, *12* (10), C10010. https://doi.org/10.1088/1748-0221/12/10/C10010.

3.  Plašil, R.; Dohnal, P.; Kálosi, Á.; Roučka, Š.; **Shapko, D.**; Rednyk, S.; Johnsen, R.; Glosík, J. Stationary Afterglow Apparatus with CRDS for Study of Processes in Plasmas from 300 K down to 30 K. *Rev. Sci. Instrum.* **2018**, *89* (6), 063116. https://doi.org/10.1063/1.5036834.

4.  Dohnal, P.; **Shapko, D.**; Kálosi, Á.; Kassayová, M.; Roučka, Š.; Rednyk, S.; Plašil, R.; Hejduk, M.; Glosík, J. Towards State Selective Recombination of $H_3^+$ under Astrophysically Relevant Conditions. *Faraday Discuss.* **2019**, *217* (0), 220 – 234. https://doi.org/10.1039/C8FD00214B.

5.  **Shapko, D.**; Dohnal, P.; Kassayová, M.; Kálosi, Á.; Rednyk, S.; Roučka, Š.; Plašil, R.; Augustovičová, L. D.; Johnsen, R.; Špirko, V.; Glosík, J. Dissociative Recombination of $N_2H^+$ Ions with Electrons in the Temperature Range of 80 – 350 K. *J. Chem. Phys.* **2020**, *152* (2), 024301. https://doi.org/10.1063/1.5128330.

6.  **Shapko, D.**; Dohnal, P.; Roučka, Š.; Uvarova, L.; Kassayová, M.; Plašil, R.; Glosík, J. Cavity Ring-down Spectroscopy Study of Neon Assisted Recombination of $H_3^+$ Ions with Electrons. *J. Mol. Spectrosc.* **2021**, *378*, 111450. https://doi.org/10.1016/j.jms.2021.111450.

7.  Plašil, R.; Roučka, Š.; Kovalenko, A.; Tran, T.D.; Rednyk, S.; Dohnal, P.; **Shapko, D.**; Gerlich, D.; Glosík, J. Reaction of $N^+$ Ion with $H_2$, HD, and $D_2$ at Low Temperatures: Experimental Study of the Pathway to Deuterated Nitrogen-containing Molecules in the Interstellar Medium. *Astrophys. J.* **2022**, *941* (2): 144 (1 – 16). https://doi.org/10.3847/1538-4357/aca088.